Cell

Article

Psilocybin triggers an activity-dependent rewiring of large-scale cortical networks

Graphical abstract

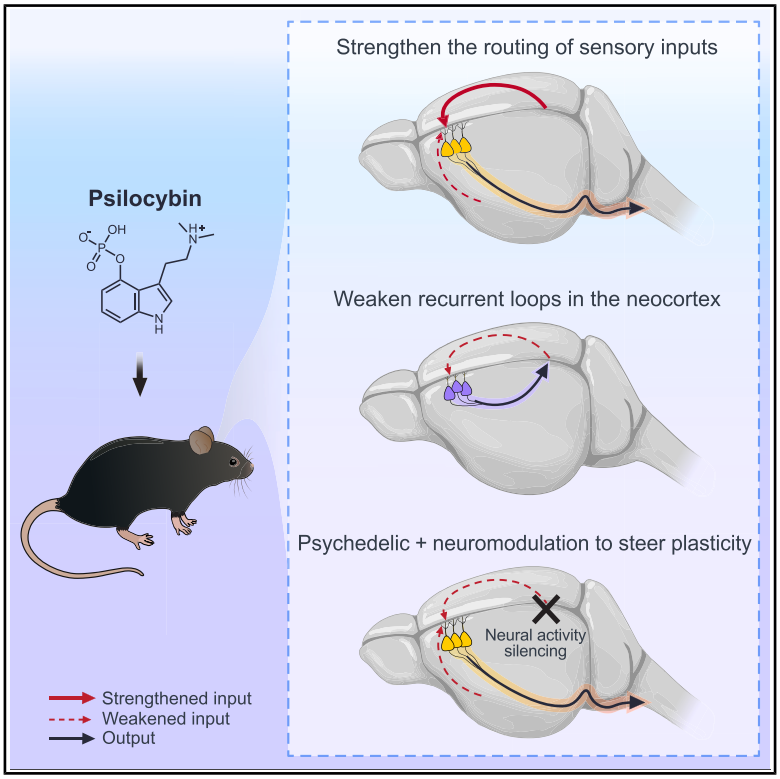

Authors

Quan Jiang, Ling-Xiao Shao, Shenqin Yao, ..., Kevin T. Beier, Hongkui Zeng, Alex C. Kwan

Correspondence

alex.kwan@cornell.edu

In brief

Psilocybin reshapes brain networks through activity-dependent plasticity, including a weakening of recurrent cortical loops that could underlie its therapeutic effects.

Highlights

- Rabies viral tracing shows how psilocybin reshapes brain connectivity
- Psilocybin strengthens pathways that route sensory inputs to subcortical regions
- Psilocybin weakens inputs associated with cortico-cortical feedback loops
- Manipulating neural activity alters the pattern of psilocybin-induced plasticity

Jiang et al., 2026, Cell *189*, 659–675
January 22, 2026
https://doi.org/10.1016/j.cell.2025.11.009

CellPress

Cell

CellPress
OPEN ACCESS

Article

Psilocybin triggers an activity-dependent rewiring of large-scale cortical networks

Quan Jiang,[1] Ling-Xiao Shao,[1] Shenqin Yao,[2] Neil K. Savalia,[1,3,4] Amelia D. Gilbert,[1] Pasha A. Davoudian,[1,3,4] Jack D. Nothnagel,[1] Guilian Tian,[5] Tin Shing Hung,[6] Hei Ming Lai,[6,7,8] Kevin T. Beier,[5] Hongkui Zeng,[2] and Alex C. Kwan[1,9,10,*]

[1]Meinig School of Biomedical Engineering, Cornell University, Ithaca, NY 14853, USA
[2]Allen Institute for Brain Science, Seattle, WA 98109, USA
[3]Interdepartmental Neuroscience Program, Yale University School of Medicine, New Haven, CT 06511, USA
[4]Medical Scientist Training Program, Yale University School of Medicine, New Haven, CT 06511, USA
[5]Department of Physiology and Biophysics, University of California, Irvine, Irvine, CA 92697, USA
[6]Department of Psychiatry, Faculty of Medicine, The Chinese University of Hong Kong, Hong Kong SAR, China
[7]Department of Chemical Pathology, Faculty of Medicine, The Chinese University of Hong Kong, Hong Kong SAR, China
[8]Li Ka Shing Institute of Health Sciences, Faculty of Medicine, The Chinese University of Hong Kong, Shatin, Hong Kong SAR, China
[9]Department of Psychiatry, Weill Cornell Medicine, New York, NY 10065, USA
[10]Lead contact
*Correspondence: alex.kwan@cornell.edu
https://doi.org/10.1016/j.cell.2025.11.009

SUMMARY

Psilocybin holds promise as a treatment for mental illnesses. One dose of psilocybin induces structural remodeling of dendritic spines in the medial frontal cortex in mice. The dendritic spines would be innervated by presynaptic neurons, but the sources of these inputs have not been identified. Here, using monosynaptic rabies tracing, we map the brain-wide distribution of inputs to frontal cortical pyramidal neurons. We discover that psilocybin's effect on connectivity is network specific, strengthening the routing of inputs from perceptual and medial regions (homolog of the default mode network) to subcortical targets while weakening inputs that are part of cortico-cortical recurrent loops. The pattern of synaptic reorganization depends on the drug-evoked spiking activity because silencing a presynaptic region during psilocybin administration disrupts the rewiring. Collectively, the results reveal the impact of psilocybin on the connectivity of large-scale cortical networks and demonstrate neural activity modulation as an approach to sculpt the psychedelic-evoked neural plasticity.

INTRODUCTION

Psychedelics are known to alter perceptual and cognitive states acutely after administration.[1] In the past decade, psychedelic-based treatments have emerged as a potential therapeutic for mental health conditions.[2] Among the various psychedelic compounds, psilocybin has yielded some of the most promising results. Numerous clinical trials have shown that psilocybin treatment with psychological support can relieve symptoms in patients with major depressive disorder or treatment-resistant depression.[3–7] Strikingly, the therapeutic benefit has been reported to last for at least 6 weeks after the administration of a single dose.[5] Psilocybin may be efficacious for other indications, such as alcohol use disorder.[8] Because of the clinical relevance, there is an urgent need to understand the neurobiological mechanisms underlying psychedelic drug action.[9]

Structural neural plasticity is likely involved in psilocybin's enduring effects on behavior. Individuals with major depressive disorder have fewer excitatory spine synapses and lower expression of synaptic proteins in the prefrontal cortex.[10,11] By contrast, the fast-acting antidepressant ketamine promotes the growth of dendritic spines in frontal cortical pyramidal neurons in rodents.[12–14] Like ketamine, a single dose of psilocybin leads to the formation of new dendritic spines in the mouse dorsal medial frontal cortex.[15] Of note, the elevation in spine number density induced by classic psychedelics is long-lasting, persisting for at least a month.[15,16] The durability of the structural remodeling in the brain may explain how psilocybin, which has a short half-life in the body,[17] can cause sustained changes in behavior.

Considering that dendritic spines are the postsynaptic sites for excitatory synapses, a key unanswered question is the identity of the presynaptic neurons that provide axonal inputs for the new connections formed after psilocybin administration. As part of the medial network of the mouse,[18] the dorsal medial frontal cortex receives long-range inputs from other cortical regions, such as the ventromedial prefrontal cortex, retrosplenial cortex (RSP), posterior parietal cortex (VISrl), and anterior insular cortex, as

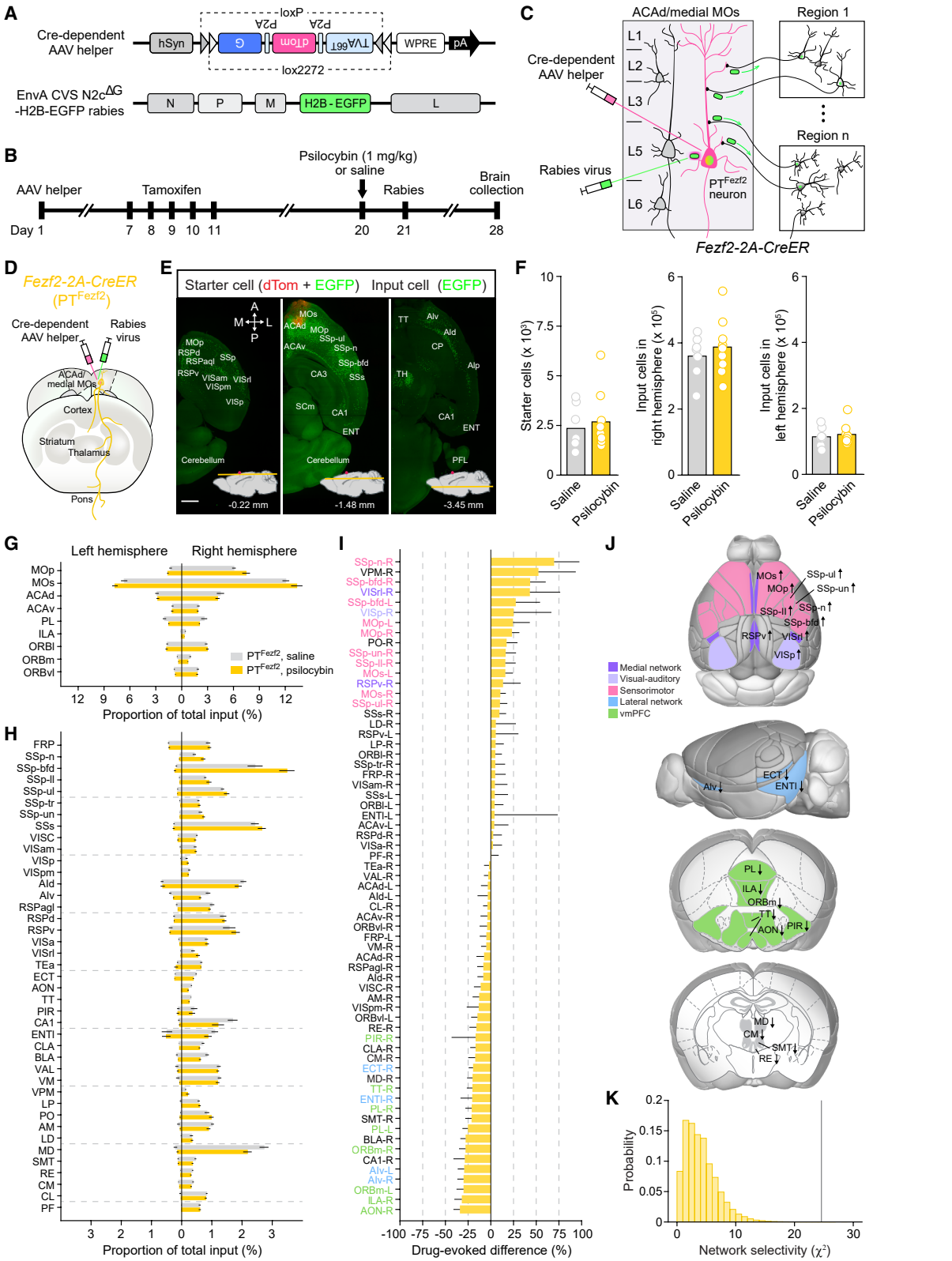

(legend on next page)

well as from subcortical regions, such as the mediodorsal and ventromedial nuclei of the thalamus, basolateral amygdala (BLA), and claustrum.[18–20] Additionally, there are local inputs and inter-hemispheric inputs from the contralateral hemisphere.[19,20] Uncovering the identity of the presynaptic neurons that provide inputs to the newly formed spines after drug administration is crucial because it will reveal the specific neural pathways that are modified by psilocybin.

Here, we perform monosynaptic tracing to map the brain-wide distribution of presynaptic cells that send inputs to the mouse dorsal medial frontal cortex. We find that psilocybin administration alters neuronal connectivity in a manner that is highly specific to brain networks. The subcortical-projecting, pyramidal tract (PT) subtype of frontal cortical pyramidal neurons gains inputs almost exclusively from the medial, sensorimotor, and visual-auditory networks but loses inputs from the ventromedial prefrontal cortex and lateral network. By contrast, the intratelencephalic (IT) subtype of frontal cortical pyramidal neurons exhibits a distinct and opposite pattern of reorganization for their presynaptic inputs. Moreover, we show that the acute effect of psilocybin on spiking activity determines if a particular source of presynaptic input would be strengthened subsequently. Collectively, our study provides crucial insights into how psilocybin modifies the connectivity of cortical networks.

RESULTS

Whole-brain tracing of drug-evoked differences in monosynaptic inputs

Monosynaptic tracing can be achieved using a rabies virus that is engineered to be EnvA-pseudotyped and glycoprotein (G) deficient.[21] Pseudotyping ensures that the rabies virus can enter only a set of experimenter-specified neurons (“starter cells”) that express the EnvA receptor (TVA). The deletion of G means that the rabies virus cannot spread, except from the starter cells in which G is expressed as a transgene. Therefore, a pseudotyped, G-deleted rabies virus (henceforth referred to as simply “rabies virus”) can transduce the starter cells and spread by crossing retrogradely one synapse to the presynaptic neurons (“input cells”), but would halt there from further spread. In this study, we used two viruses for monosynaptic tracing: an hSyn-driven, Cre-dependent adeno-associated virus (AAV) helper virus, AAV-hSyn-DIO-TVA^{66T}-dTomato-CVS N2c G, and the rabies virus, EnvA-CVS N2c$^{\Delta G}$-H2B-EGFP (Figure 1A).

The experimental timeline for monosynaptic tracing is shown in Figure 1B. The Cre-dependent AAV helper virus was injected into the dorsal medial frontal cortex of an animal, for example, the *Fezf2-2A-CreER* mouse, which is an inducible Cre-driver strain targeting the PT subtype of cortical pyramidal cells.[22] Subsequently, tamoxifen was administered to induce Cre expression. 2 weeks later, after sufficient time for TVA and G expression in the starter cells, psilocybin (1 mg/kg intraperitoneally [i.p.]) or saline was administered, followed a day later by the injection of rabies virus into the dorsal medial frontal cortex. The rabies virus was injected after drug administration to ensure that the labeled input cells would reflect differences caused by psilocybin and not pre-existing connectivity prior to drug administration. We chose a dose of 1 mg/kg for psilocybin because it evokes structural neural plasticity in the mouse dorsal medial frontal cortex.[15] Finally, 1 week would elapse for rabies to spread before the brain was collected for analysis. The anticipated result is that we would find starter cells expressing both dTomato and EGFP, whereas the input cells would express EGFP only (Figure 1C).

We targeted the viral injections to the dorsal medial frontal cortex, encompassing the anterior cingulate cortex (ACAd) and the medial portion of the secondary motor cortex (MOs), because brain-wide c-Fos mapping studies showed that this region responds robustly to stress, ketamine, and psilocybin.[23,24] Moreover, psilocybin leads to rapid and persistent structural neural plasticity in this region of the medial frontal cortex.[15] We verified that the monosynaptic tracing method worked as expected by performing multiple control experiments involving a modified AAV helper virus that does not express G protein (Figures S1A–S1C), AAV helper virus only without rabies (Figures S1D and S1E), and rabies virus only without AAV helper virus (Figures S1F and S1G).

Psilocybin modifies inputs to frontal cortical PT^{Fezf2} neurons in a network-specific pattern

Two major subtypes of pyramidal neurons in the neocortex are the PT and IT neurons (Figures S2A–S2F). These subtypes are

Figure 1. Psilocybin modifies inputs to frontal cortical PT^{Fezf2} neurons in a network-specific pattern

(A) The viruses used in this study.

(B) Experimental timeline.

(C) When the viruses are injected in the dorsal medial frontal cortex of a *Fezf2-2A-CreER* mouse, the PT^{Fezf2} starter cells would express dTomato and EGFP, while input cells would express EGFP only.

(D) Monosynaptic tracing from frontal cortical PT^{Fezf2} neurons using the *Fezf2-2A-CreER* mouse.

(E) Images from whole-brain imaging, showing starter cells (red and green) and input cells (green). Depths relative to bregma (red circle) are indicated. Scale bar, 1 mm.

(F) The number of starter cells, input cells in the ipsilateral hemisphere, and input cells in the contralateral hemisphere for *Fezf2-2A-CreER* mice treated with saline or psilocybin. Bar, mean. Circle, individual animal. Wilcoxon rank-sum test.

(G) Proportion of input cells contributed by presynaptic regions in the frontal cortex (mean ± SEM).

(H) Proportion of input cells contributed by other presynaptic regions (mean ± SEM).

(I) Drug-evoked difference (psilocybin subtracted by saline, relative to saline) in the proportion of input cells for all 65 presynaptic regions for PT^{Fezf2} neurons (mean and 90% confidence interval). The list was sorted based on the drug-evoked difference. Presynaptic regions with >10% or <−15% in drug-evoked difference were color coded according to their network membership.

(J) Schematic showing the presynaptic regions with >10% or <−15% in drug-evoked difference.

(K) Network selectivity analysis, testing against the null hypothesis that the increases and decreases in drug-evoked difference were distributed randomly across the 5 cortical networks. Histogram, distribution of χ^2 values for the null hypothesis. Vertical line, observed χ^2 value ($p = 6 \times 10^{-5}$).

$N = 9$ mice for psilocybin and 8 mice for saline.

See also Figures S1, S2, and S3 and Table S1.

non-overlapping populations with distinct morphological characteristics, electrophysiological properties, and long-range projection targets.[19,25,26] Previous work indicated that the PT subtype of pyramidal neurons in the dorsal medial frontal cortex is essential for the long-term behavioral effects of psilocybin.[27] To determine how psilocybin may alter inputs into frontal cortical PT neurons, we performed monosynaptic tracing using *Fezf2-2A-CreER* mice ($N = 4$ male and $N = 5$ female animals for psilocybin; $N = 4$ male and $N = 4$ female animals for saline; Figures 1D, S2G, and S2H). We injected viruses into the right hemisphere; therefore, the right hemisphere is ipsilateral and left hemisphere is contralateral. To determine the brain-wide distribution of input cells, we processed the rabies-traced brains through a pipeline involving tissue clearing, light sheet fluorescence microscopy, and machine learning-based automated detection of nuclei, which enabled us to locate and count all starter and input cells in the mouse brain (Figure S3A). As expected, we observed co-expression of red (dTomato) and green (EGFP) fluorescence from starter cells located in the dorsal medial frontal cortex, whereas green (EGFP) fluorescence from input cells was widespread in the brain (Figure 1E). Video S1 shows images of the dTomato (red) and EGFP (green) expression, highlighting the brain-wide distribution of input cells into the frontal cortical PT^{Fezf2} neurons. Video S2 shows images from the same brain for the dTomato expression (red) and NeuN immunostaining (white), showing the starter PT^{Fezf2} neurons with cell bodies in the dorsal medial frontal cortex and axons projecting ipsilaterally to the striatum as well as out of the cerebrum into the thalamus and pons. The images were aligned to the mouse brain atlas and divided based on the 316 summary structures in the Allen Mouse Brain Common Coordinate Framework version 3.[28]

Starter cells were defined as those neurons with colocalized red and green fluorescence within the ipsilateral frontal cortex (primary motor cortex [MOp], MOs, ACAd, anterior cingulate area, ventral part [ACAv], prelimbic area [PL], infralimbic area [ILA], orbital area, lateral part [ORBl], medial orbital frontal cortex [ORBm], and orbital area, ventrolateral part [ORBvl]). We had similar initial conditions for the psilocybin and saline groups, with 2,680 ± 491 and 2,350 ± 359 starter cells, respectively ($p = 0.7$, Wilcoxon rank-sum test; Figure 1F). As expected, most starter cells were detected in the dorsal medial frontal cortex (94% ± 2% and 95% ± 2% in ACAd, MOs, or PL for the saline and psilocybin groups, respectively; Figure S3F). Input cells were defined as those neurons with green fluorescence anywhere in the brain, except they cannot also have red fluorescence, which would make them starter cells. For mice that received psilocybin, there were $5.1 \pm 0.5 \times 10^5$ input cells, whereas for mice that received saline, there were $4.7 \pm 0.3 \times 10^5$ input cells ($p = 0.7$, Wilcoxon rank-sum test; Figures 1F, S3B, and S3D).

To identify the sources of the presynaptic inputs, we calculated the fraction of input cells residing in each region. Many regions did not provide appreciable input to the dorsal medial frontal cortex, so we analyzed only the 65 regions contributing at least 0.3% of the total inputs in any treatment or cell-type condition (henceforth referred to as "presynaptic regions"). Together these presynaptic regions captured nearly all input cells (saline, 87.6% ± 0.6%; psilocybin, 89.2% ± 0.7%; Figures 1G and 1H). Next, we sorted the presynaptic regions based on the normalized difference of psilocybin's effect on the input fraction relative to saline, revealing numerous regions with increases, including the primary somatosensory cortex and its associated thalamic nuclei (primary somatosensory area [SSp], ventral posteromedial nucleus of the thalamus [VPM], and posterior complex of the thalamus [PO]), VISrl, primary visual cortex (VISp), MOp, RSP, and others (Figure 1I). Other regions had decreased input fraction following psilocybin administration, such as the ILA, ORBm, ventral agranular insular cortex (AIv), hippocampus (CA1), and BLA. Focusing on the regions with the largest psilocybin-evoked increase (>10%) or decrease (<−15%) in input fraction, we discovered that the strengthened presynaptic regions belong to the medial, visual-auditory, and sensorimotor networks (Figure 1J). This demarcation of cortical networks is based on modules identified in a prior large-scale study of long-range connectivity.[18] Regions that contributed fewer inputs after psilocybin administration came from the lateral network, ventromedial prefrontal cortex, and medial nuclei of the thalamus (Figure 1J). To test the statistical likelihood of such a network-specific preference in the input fraction change, we performed a chi-squared test to compare the observed data with shuffled data to find that the network selectivity for psilocybin's effect was highly significant for PT^{Fezf2} neurons ($\chi^2 = 24.6$, degrees of freedom [df] = 4, $p = 6 \times 10^{-5}$, chi-squared test; Figure 1K). The results demonstrate that psilocybin induces a network-specific reorganization of the inputs impinging on the PT subtype of pyramidal neurons in the mouse dorsal medial frontal cortex.

Opposing effects of psilocybin on inputs to the two major pyramidal cell types

Another major subtype of pyramidal neurons is the IT neurons. Unlike the subcortical-projecting PT neurons, the axons of IT neurons stay within the telencephalon to communicate with cortical and striatal locations in both hemispheres. Studies that examined cortical PT and IT neurons showed that the two cell types receive different local and long-range inputs,[19,29–31] which may underpin their distinct roles during behavior.[27,32–34] To determine how psilocybin may modify the inputs to frontal cortical IT neurons, we performed monosynaptic tracing using the *PlexinD1-2A-CreER* mouse, which is an inducible Cre-driver line for IT neurons[22] ($N = 4$ male and $N = 4$ female animals for psilocybin; $N = 4$ male and $N = 4$ female animals for saline; Figures 2A, 2B, S2G, and S2H; Videos S3 and S4).

Beginning from 5,495 ± 1,046 and 4,511 ± 696 starter cells ($p = 0.6$, Wilcoxon rank-sum test; 92% ± 1% and 91% ± 3% located in ACAd, MOs, or PL; Figures 2C and S3G), we counted $5.6 \pm 0.5 \times 10^5$ and $5.7 \pm 0.5 \times 10^5$ input cells for the psilocybin and saline groups, respectively ($p = 0.9$, Wilcoxon rank-sum test; Figures 2C, S3C, and S3E). The same set of 65 presynaptic regions, selected based on the criterion of containing at least 0.3% of the total inputs in any treatment or PT/IT condition, captured nearly all the input cells to the frontal cortical IT^{Plxnd1} neurons (saline, 89.4% ± 0.6%; psilocybin, 89.8% ± 0.6%). We plotted the input fraction for the psilocybin and saline groups in each of the frontal cortical (Figure 2D) and long-range cortical and subcortical presynaptic regions (Figure 2E). We plotted the difference in input fraction due to psilocybin relative to saline

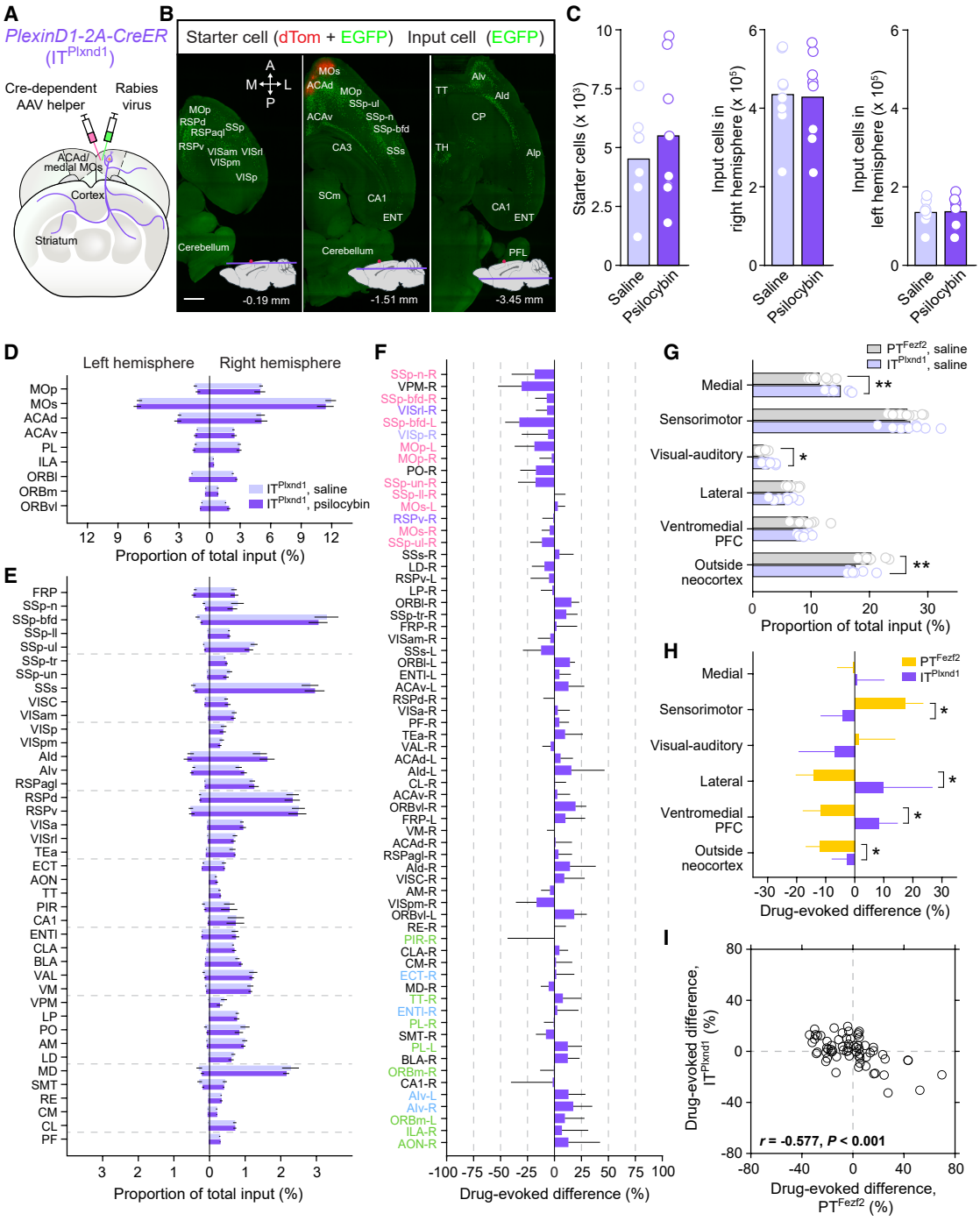

Figure 2. Opposing effects of psilocybin on presynaptic inputs to the two major pyramidal cell types

(A) Monosynaptic tracing from frontal cortical IT^{Plxnd1} neurons using the *PlexinD1-2A-CreER* mouse.

(B) Images from whole-brain imaging, showing starter cells (red and green) and input cells (green). Depths relative to bregma (red circle) are indicated. Scale bar, 1 mm.

(C) The number of starter cells, input cells in the ipsilateral hemisphere, and input cells in the contralateral hemisphere for *PlexinD1-2A-CreER* mice treated with saline or psilocybin. Bar, mean. Circle, individual animal.

(D) Proportion of input cells contributed by presynaptic regions in the frontal cortex (mean ± SEM).

(E) Proportion of input cells contributed by other presynaptic regions (mean ± SEM).

(F) Drug-evoked difference (psilocybin subtracted by saline, relative to saline) in the proportion of input cells for all 65 presynaptic regions for IT^{Plxnd1} neurons (mean and 90% confidence interval). The list was sorted based on the drug-evoked difference. Presynaptic regions with >10% or <−15% in drug-evoked difference were color coded according to their network membership.

(legend continued on next page)

(Figures 2F, S4A, and S4D). Although the specific input cells exhibiting changes were distinct between PT^{Fezf2} and IT^{Plxnd1} neurons, we found that psilocybin's effect on the input fraction of frontal cortical IT^{Plxnd1} neurons is also highly network-specific ($\chi^2 = 15.0$, df = 4, $p = 0.005$, chi-squared test; Figures S4B and S4C). The next analyses would be aimed at delineating the significant differences between PT^{Fezf2} and IT^{Plxnd1} neurons.

First, only considering the saline condition, we observed that PT^{Fezf2} and IT^{Plxnd1} neurons receive long-range inputs from different networks. Frontal cortical IT^{Plxnd1} neurons received a higher fraction of inputs from the medial network (15.0% ± 0.7% for IT, 11.4% ± 0.6% for PT; $p = 0.004$, Wilcoxon rank-sum test) and visual-auditory regions (2.7% ± 0.3% for IT, 1.9% ± 0.2% for PT; $p = 0.05$, Wilcoxon rank-sum test), but had a significantly lower fraction of inputs from outside the neocortex (17.6% ± 0.6% for IT, 20.3% ± 0.7% for PT; $p = 0.007$, Wilcoxon rank-sum test), compared with their PT^{Fezf2} counterparts (Figures 2G, S3H, and S3I). When we determined the effects of psilocybin, there were also cell-type-specific differences. In response to psilocybin, the IT^{Plxnd1} neurons differed significantly from the PT^{Fezf2} neurons in that they had reduced input fraction from the sensorimotor network (−4% for IT, 17% for PT; statistically significant based on 95% confidence interval from bootstrapping), but instead gained input fraction from the lateral network (10% for IT and −14% for PT) and the ventromedial prefrontal cortex (8% for IT and −12% for PT; Figure 2H). Both pyramidal cell types lost input fraction from regions outside the neocortex after psilocybin administration, but the effect was less pronounced for IT neurons (−3% for IT and −12% for PT). Psilocybin's opposing effect on the input fraction to the two cell types was most clearly demonstrated by plotting the drug-induced difference in input fraction for all 65 presynaptic regions, which showed a significant negative correlation ($r = -0.58$, $p = 5 \times 10^{-7}$, Pearson correlation; Figure 2I). These results indicate that, in the mouse dorsal medial frontal cortex, for those inputs that are strengthened in PT neurons by psilocybin, they tend to be weakened in IT neurons after drug administration, and vice versa. Therefore, psilocybin exerts opposing changes to the synaptic input organization for the two main pyramidal cell subtypes in the mouse dorsal medial frontal cortex.

Psilocybin-evoked rewiring is related to the pattern of drug-induced c-Fos expression

We wanted to know why inputs from certain presynaptic regions are selectively strengthened by psilocybin. Presynaptic regions send axon collaterals that terminate in different layers of the mouse dorsal medial frontal cortex, which may influence psilocybin's plasticity potential. To explore this possibility, we leveraged the Allen Mouse Connectivity database, which contains images of fluorescent axons following viral injections at hundreds of locations in the mouse brain.[35] The analyses suggest that the laminar distribution of long-range axons in the dorsal medial frontal cortex is unlikely to explain why certain presynaptic regions are favored for potentiation by psilocybin (Figure S5).

Another possibility is that the baseline expression of certain subtypes of 5-HT receptors may predispose a presynaptic region to be sensitive to psilocybin-induced rewiring. Using the *in situ* hybridization data in the Allen Brain Atlas,[36] we correlated the expression levels of the *Htr1a*, *Htr2a*, and *Htr2c* transcripts, which encode the 5-HT_{1A}, 5-HT_{2A}, and 5-HT_{2C} receptors, respectively, with the psilocybin-induced difference in input cells for presynaptic regions in the cortex (Figures 3A–3C). There was no clear relationship for *Htr1a* and *Htr2a*. For *Htr2c*, the correlation approached significance for PT^{Fezf2} neurons ($p = 0.08$, Pearson correlation), suggesting a potential trend, and reached significance for IT^{Plxnd1} neurons ($p = 0.02$, Pearson correlation). These analyses suggest that while receptor expression does not fully explain the psilocybin-evoked changes, certain subtypes, such as *Htr2c* may partially contribute.

We found a more robust relationship when examining the psilocybin-evoked activation of the immediate early gene c-Fos. In a previous study,[37] our lab injected mice with psilocybin (1 mg/kg i.p.) or saline, collected the brains 2 h later, and then used tissue clearing, c-Fos antibody labeling, and light sheet fluorescence microscopy to visualize c-Fos+ cells in the entire mouse brain (Figure 3D). We compared the drug-evoked difference in c-Fos+ cells with the drug-evoked difference in input cells on a region-by-region basis. For the presynaptic regions in the neocortex, those locations with greater increases in the number of c-Fos+ cells were associated with a higher elevation of input cells for frontal cortical PT^{Fezf2} neurons after psilocybin administration ($r = 0.44$, $p = 0.02$, Pearson correlation; Figure 3E). By contrast, psilocybin's effects on c-Fos activation and input cell gain were negatively correlated for the frontal cortical IT^{Plxnd1} neurons ($r = -0.41$, $p = 0.03$, Pearson correlation; Figure 3E). Altogether, these results indicate that psilocybin-induced c-Fos activation is related to the gain and loss of input cells for frontal cortical PT and IT neurons, respectively. Because c-Fos expression is known to be activity-dependent, this exploratory analysis hints at spiking activity as a potential factor underlying the pattern of synaptic reorganization evoked by psilocybin.

Potentiation of RSP inputs onto PT^{Fezf2} neurons in the medial frontal cortex after psilocybin administration

To delineate the potential mechanisms, we focused on one presynaptic region: the RSP. RSP is known to have dense reciprocal connections with the dorsal medial prefrontal cortex in mice.[18,20,38] The RSP is relevant for the neurobiology of psilocybin because it is a core region in the mouse analog of the default mode network,[39–41] which is thought to be centrally involved in

(G) Source of ipsilateral presynaptic inputs to PT^{Fezf2} and IT^{Plxnd1} neurons in saline-treated mice. Circle, individual animal. *$p < 0.05$, **$p < 0.01$, Wilcoxon rank-sum test.
(H) Drug-evoked difference in the proportion of ipsilateral input cells from the 5 cortical networks and outside neocortex to PT^{Fezf2} and IT^{Plxnd1} neurons. Error bar, 90% confidence interval. *, significant based on 95% confidence intervals.
(I) Drug-evoked difference in the proportion of input cells for all 65 presynaptic regions, for PT^{Fezf2} neurons versus IT^{Plxnd1} neurons. Circle, individual presynaptic region. *r*, Pearson correlation coefficient.
N = 8 mice for psilocybin and 8 mice for saline.
See also Figures S2, S3, and S4 and Table S1.

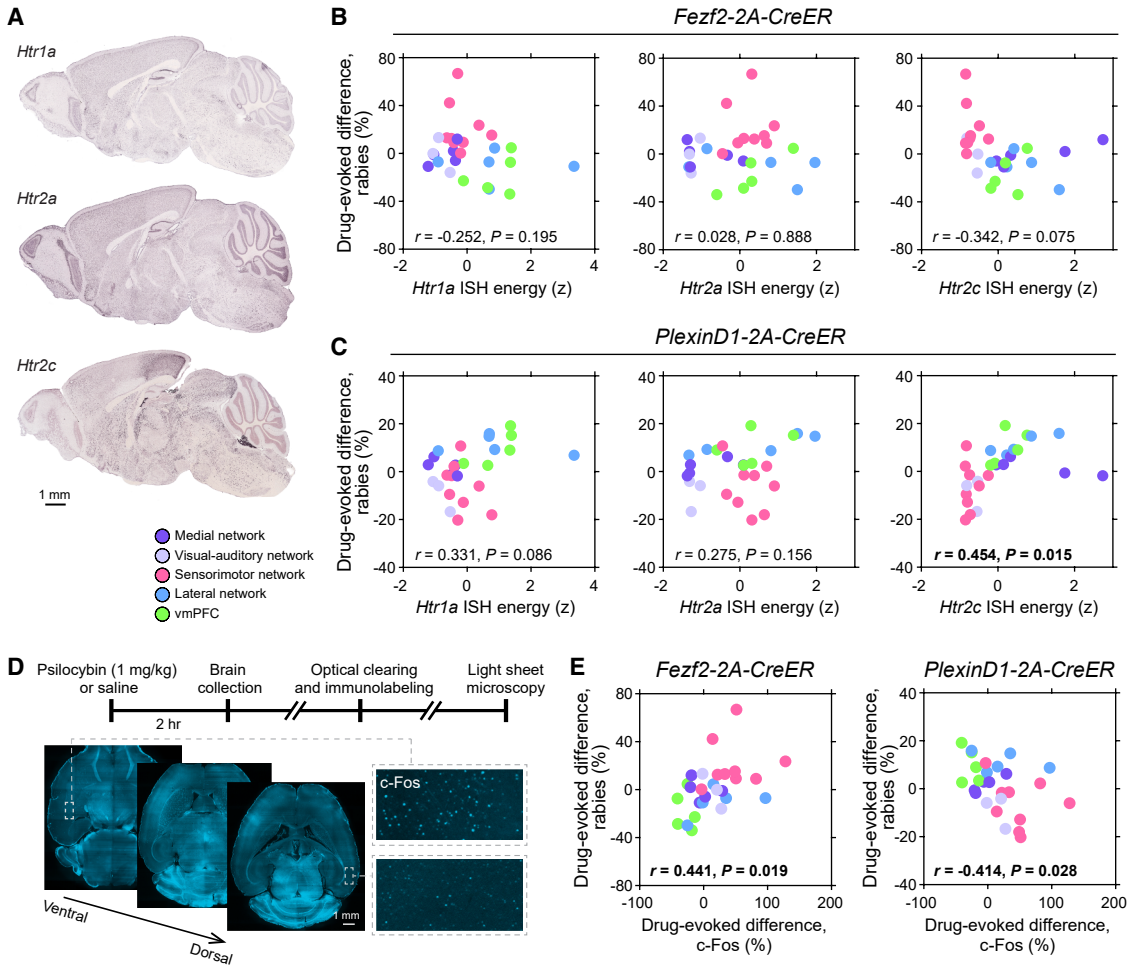

Figure 3. Psilocybin-evoked rewiring correlates with the pattern of drug-evoked c-Fos expression

(A) *In situ* hybridization (ISH) images for *Htr1a*, *Htr2a*, and *Htr2c* transcripts.

(B) The ISH expression of *Htr1a*, *Htr2a*, or *Htr2c* versus psilocybin-evoked differences in input fraction for PT^{Fezf2} neurons. Circle, individual presynaptic region. The color denotes the cortical network membership. *r*, Pearson correlation coefficient.

(C) Similar to (B) for IT^{Plxnd1} neurons.

(D) Experimental timeline for imaging psilocybin's effect on brain-wide c-Fos expression. Insets, representative fluorescence images in a psilocybin-treated mouse. Scale bar, 1 mm.

(E) Psilocybin-evoked differences in c-Fos expression versus psilocybin-evoked differences in input fraction for PT^{Fezf2} and IT^{Plxnd1} neurons. Circle, individual presynaptic region. The color denotes the cortical network membership. *r*, Pearson correlation coefficient.

See also Figure S5 and Table S1.

mediating the effects of psychedelics in humans.[42–44] Our whole-brain rabies tracing results indicated that RSP was a top-ranked region with >10% increase in input fraction to frontal cortical PT^{Fezf2} neurons.

We performed longitudinal two-photon imaging to determine the effect of psilocybin on the density of long-range inputs in the medial frontal cortex (Figures 4A and 4B). To label the boutons along axons originating from neurons in RSP, we injected AAV-hSyn-Synaptophysin-mRuby2 into RSP. Initially, we planned to visualize simultaneously axonal boutons and dendritic spines; therefore, we also injected AAV-CAG-Flex-EGFP into the ACAd/medial MOs of these *Fezf2-2A-CreER* mice to label PT^{Fezf2} neurons; however, the EGFP-expressing dendrites were too dense to resolve most spines, and thus we restricted the analysis to axonal boutons only (Figure 4C). We tracked a total of 60 and 62 fields of view from 7 and 8 animals for the saline and psilocybin conditions, respectively. Using an automated algorithm to count red puncta from the *in vivo* images, we observed that psilocybin increased the number of detectable RSP axonal boutons in superficial layers of the dorsal medial frontal cortex at 1 and 3 days following treatment, relative to saline (day 1, 5.5% ± 3.3% for psilocybin versus −8.6% ± 3.9% for saline; $p = 0.056$, post hoc comparison; day 3, 11.4% ± 4.6% for psilocybin versus −7.6% ± 3.9% for saline; $p = 0.007$, post hoc comparison; treatment and time interaction, $p = 0.0004$, linear mixed-effects model; Figure 4D). We note a decline in bouton

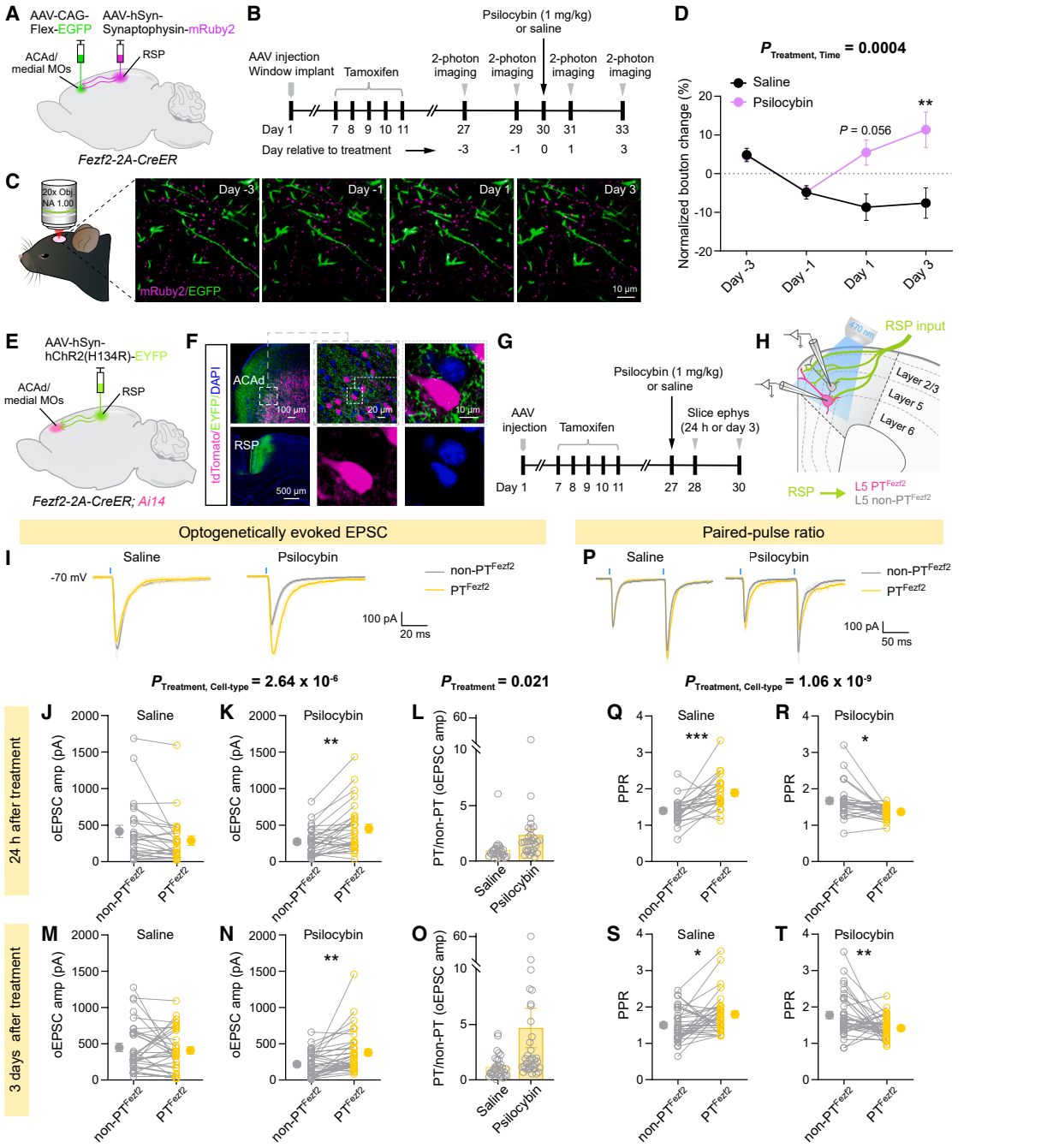

Figure 4. Potentiation of RSP inputs onto PT^{Fezf2} neurons in the medial frontal cortex after psilocybin administration

(A) Strategy to express mRuby2 in axonal boutons of RSP neurons and EGFP in frontal cortical PT^{Fezf2} neurons.

(B) Experimental timeline.

(C) Example *in vivo* two-photon images. Scale bar, 10 µm.

(D) The density of RSP axonal boutons in the medial frontal cortex after psilocybin (magenta; 1 mg/kg i.p.) or saline (black) across days, expressed as the fold change from the baseline (mean ± SEM).

(E) Strategy to express ChR2 in RSP neurons and tdTomato in PT^{Fezf2} neurons.

(F) Post hoc histology. Scale bars, 100 µm (left top), 20 µm (middle top), 10 µm (right top), 500 µm (left bottom).

(G) Experimental timeline.

(H) Successive whole-cell recordings were made from a PT^{Fezf2} neuron and a non-PT^{Fezf2} neuron.

(I) Example optogenetically evoked EPSC in a pair of PT^{Fezf2} and non-PT^{Fezf2} neurons for saline and psilocybin conditions.

(J) Amplitude of the optogenetically evoked EPSC, 24 h after saline administration. Circle, individual cell.

(legend continued on next page)

density prior to treatment, possibly due to photobleaching of the synaptophysin-fused fluorophores, which affected the saline and psilocybin groups similarly (day −1, −4.7% ± 1.3% for psilocybin and −4.8% ± 1.7% for saline; $p = 1$, post hoc comparison). The imaging results thus corroborate the finding from rabies tracing to show a psilocybin-evoked increase in RSP axonal boutons in the dorsal medial frontal cortex.

To evaluate further the effect of psilocybin on RSP inputs and specifically in frontal cortical PT^{Fezf2} neurons, we measured synaptic transmission using slice electrophysiology. We injected AAV-hSyn-hChR2(H134R)-EYFP into RSP to enable photostimulation of axons originating from RSP, which was done in *Fezf2-2A-CreER;Ai14* mice where PT^{Fezf2} neurons expressed tdTomato so we could target them for whole-cell recording (Figures 4E and 4F). Acute brain slices containing ACAd/medial MOs were prepared at 1 or 3 days after the administration of psilocybin (1 mg/kg i.p.) or saline (5–7 mice for each condition; Figure 4G). During each recording session, we would pair the recordings by measuring in succession from a PT^{Fezf2} neuron and a non-PT^{Fezf2} neuron (i.e., an adjacent pyramidal cell without tdTomato; Figure 4H). The motivation was to account for the variable ChR2 expression across experiments and the opposing effects of psilocybin for inputs onto PT^{Fezf2} and IT^{Plxnd1} neurons. A single brief pulse of photostimulation was used to elicit an optogenetically evoked excitatory postsynaptic current (oEPSC; Figure 4I). We found that psilocybin induced cell-type-specific effects on oEPSC amplitude when tested 24 h or 3 days after treatment (treatment and cell-type interaction, $p = 3 \times 10^{-6}$, linear mixed-effects model; Figures 4J, 4K, 4M, and 4N). Specifically, the oEPSC amplitude for PT^{Fezf2} neurons relative to non-PT^{Fezf2} pyramidal cells was higher after psilocybin administration (main effect of treatment, $p = 0.02$, linear mixed-effects model; Figures 4L and 4O). We also assessed psilocybin's effects on optogenetically evoked inhibitory postsynaptic currents (oIPSCs; Figures S6A–S6G), the oEPSC-to-oIPSC ratio (Figures S6H–S6J), and monosynaptic oEPSC in the presence of tetrodotoxin (TTX) and 4-AP (Figures S6K–S6O). Two brief pulses of photostimulation spaced by a short interval were applied to measure paired-pulse ratio (PPR; Figure 4P). With this protocol, we likewise observed that psilocybin induced cell-type-specific effects on PPR at both 1 and 3 days after psilocybin administration (treatment and cell-type interaction, $p = 1 \times 10^{-9}$, linear mixed-effects model; Figures 4Q–4T). The reduced PPR in PT^{Fezf2} neurons suggests psilocybin's effects on the RSP→ACAd excitatory connections may include an increase in presynaptic release probability. Additional electrophysiological data obtained via a different viral labeling strategy provided further evidence for psilocybin's effects on oEPSC and PPR (Figures S6P–S6W). Overall, these data demonstrate psilocybin-induced potentiation of excitatory synaptic drive from RSP to frontal cortical PT^{Fezf2} neurons, which persisted for at least 3 days after drug exposure.

Psilocybin elevates the spiking activity of frontal-cortex-projecting neurons in RSP

After confirming RSP as an input source altered by psilocybin, we tested the importance of spiking activity by measuring firing rates in RSP using *in vivo* electrophysiology. To record specifically from the frontal-cortex-projecting neurons, we injected the retrogradely transported AAVretro-hSyn-Cre into the dorsal medial frontal cortex of an *Ai32* mouse for Cre-dependent expression of channelrhodopsin (ChR2; Figure 5A). For each recording session, we would perform a craniotomy at ipsilateral RSP, insert a high-density Neuropixels electrode, record for 30 min, infuse psilocybin (1 mg/kg i.p.) or saline through an implanted catheter, record for another 60 min, and then use laser photostimulation (473 nm, 20 ms) for opto-tagging (Figure 5B). We isolated single units from the recording via spike sorting and curated based on quality metrics (Figures S7A and S7B). The Neuropixels probe was coated with the fluorescent dye CM-DiI, allowing us to visualize the tract in post hoc histology performed after each recording session (Figure 5C). The reconstructed probe trajectories for all recordings confirmed the targeting of RSP (Figure 5D). During the opto-tag protocol, most neurons exhibited no detectable change in firing rate from the laser photostimulation; however, some cells were driven to fire reliably and with short latency (Figures 5E, 5F, and S7C). These neurons with photostimulation-evoked spiking activity would be the ChR2-expressing RSP→ACAd neurons.

In total, we recorded from 38 and 42 opto-tagged RSP→ACAd neurons, along with 417 and 710 other untagged neurons, in saline and psilocybin conditions, respectively ($N = 2$ male and $N = 4$ female animals for psilocybin; $N = 3$ male and $N = 3$ female animals for saline). We compared the firing rates of opto-tagged RSP→ACAd neurons before and after the administration of psilocybin or saline (Figures 5G–5I, S7D, and S7E). For saline, there was no detectable change in the spiking activity of RSP→ACAd neurons (pre-saline, 11.1 ± 1.6 Hz; post-saline, 12.2 ± 1.6 Hz). By contrast, the administration of psilocybin elicited a 39% increase in the firing rate of the RSP→ACAd neurons (pre-psilocybin, 8.9 ± 1.1 Hz; post-psilocybin, 12.4 ± 1.3 Hz; $p = 0.002$, post hoc comparison; treatment, time, and cell-type interaction, $p = 0.031$,

(K) Similar to (J) for psilocybin administration.
(L) Based on data in (J) and (K), the ratio is calculated by dividing the amplitude of a PT^{Fezf2} neuron by the amplitude of its paired non-PT^{Fezf2} neuron. Circle, individual cell pair. Bar, mean ± SEM.
(M–O) Similar to (J)–(L), 3 days after saline or psilocybin administration.
(P) Example optogenetically evoked EPSCs evoked by two brief pulses in a pair of PT^{Fezf2} and non-PT^{Fezf2} neurons, for saline and psilocybin conditions.
(Q) PPR, 24 h after saline administration. Circle, individual cell.
(R) Similar to (Q) for psilocybin administration.
(S and T) Similar to (Q) and (R), 3 days after saline or psilocybin administration.
For imaging, $n = 60$ fields of view from 7 mice for saline and 62 fields of view from 8 mice for psilocybin. For slice electrophysiology, $n = 23$–25 cell pairs from 6 mice for 24 h after saline, 26–29 cell pairs from 7 mice for 24 h after psilocybin, 33 cell pairs from 5 mice for 3 days after saline, and 34 cell pairs from 7 mice for 3 days after psilocybin. Linear mixed-effects model. See Table S2. $^{*}p < 0.05$, $^{**}p < 0.01$, $^{***}p < 0.001$.
See also Figure S6.

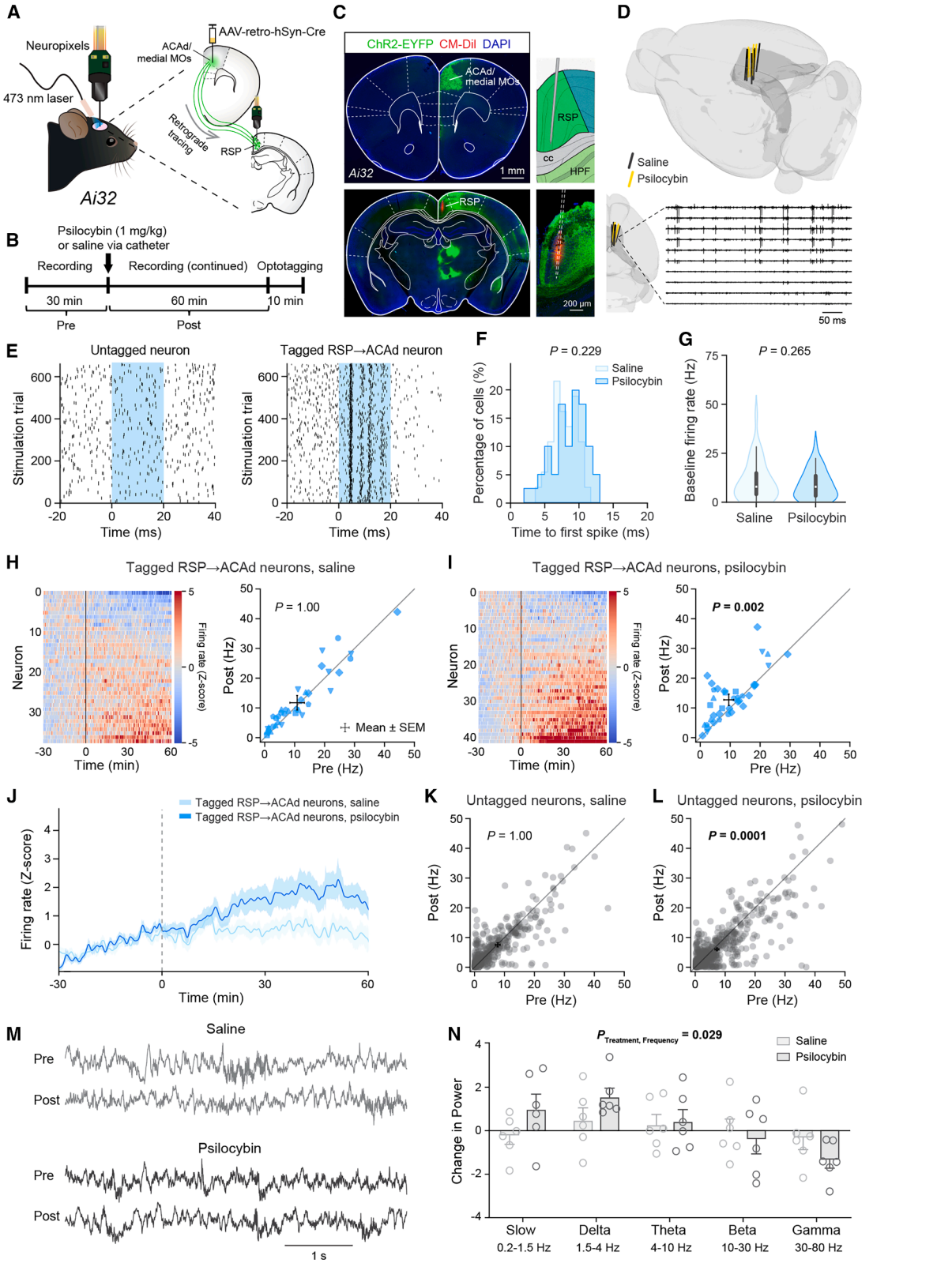

(legend on next page)

linear mixed-effects model). The psilocybin-induced elevation of spiking activity in RSP→ACAd neurons started at ∼15 min after drug administration and persisted until the end of the recording (Figure 5J). Psilocybin reduced the firing of untagged neurons (pre-saline, 7.8 ± 0.5 Hz; post-saline, 7.6 ± 0.5 Hz; $p = 1$, post hoc comparison; pre-psilocybin, 7.1 ± 0.4 Hz; post-psilocybin, 6.1 ± 0.3 Hz; $p = 0.0001$, post hoc comparison; Figures 5K, 5L, S7F, and S7G). One caveat for this experiment is that the recorded RSP→ACAd neurons were not restricted to those that specifically project to PT^{Fezf2} or IT^{Plxnd1} cell types. In addition to single-unit activity, we analyzed the local field potential (LFP) recorded after drug administration (Figure 5M). Averaging the power spectra obtained from LFPs recorded from channels located within 300 μm of the pial surface and comparing pre- versus post-treatment, we observed a shift in the spectral power with increases around the delta band and decreases at the high-frequency gamma band after psilocybin administration (delta, 1.6% ± 0.4% for psilocybin versus 0.5% ± 0.6% for saline; gamma, −1.4% ± 0.4% for psilocybin versus −0.3% ± 0.5% for saline; treatment and frequency interaction, $p = 0.029$, linear mixed-effects model; Figures 5N and S7H–S7L). The increase in delta power was reminiscent of the oscillatory activity previously associated with the dissociative effects of ketamine.[45,46] Altogether, these data indicate that psilocybin increases spiking activity selectively in the frontal cortex-projecting neurons in RSP, which is one of the presynaptic regions that showed strengthened presynaptic inputs to the PT^{Fezf2} neurons after psilocybin.

Chemogenetic silencing of RSP alters psilocybin-evoked rewiring

To test causally if the neural activity in a presynaptic region influences psilocybin-induced rewiring, we manipulated the excitability of neurons in RSP using chemogenetics[47] (Figure 6A). We used the same experimental protocol as our monosynaptic tracing in the *Fezf2-2A-CreER* mouse, with the addition of injecting AAV-hSyn-hM4D(Gi)-mCherry in the RSP to express the inhibitory chemogenetic receptor hM4D(Gi) in RSP neurons (Figure 6B). At 15 min before the administration of psilocybin (1 mg/kg i.p.) or saline, we would inject the chemogenetic ligand deschloroclozapine[48] (DCZ; 0.1 mg/kg i.p.) or DMSO vehicle. Therefore, we were using chemogenetics to silence RSP neurons when psilocybin is psychoactive. The experiment proceeded with rabies tracing and histology, where coronal brain sections were prepared for visualization of EGFP-expressing input cells in RSP and neighboring brain regions.

We performed the experiment using 3–4 animals per condition and obtained 3 brain sections per animal ($N = 2$ male and $N = 2$ female animals for DMSO + saline; $N = 1$ male and $N = 2$ female animals for DMSO + psilocybin; $N = 2$ male and $N = 2$ female animals for DCZ + saline; and $N = 2$ male and $N = 2$ female for DCZ + psilocybin). As anticipated, we observed co-expression of red and green fluorescence in starter cells at the injection site in ACAd and medial MOs (Figure 6C). At RSP, we detected green fluorescence in input cells and additionally red fluorescence from the mCherry fluorophore that is fused to the chemogenetic hM4D(Gi) receptor expressed in RSP neurons (Figure 6C). For the RSP, there was a significant interaction effect (drug and chemogenetics interaction, $p = 0.046$, linear mixed-effects model), indicating that inhibiting neural activity in RSP interfered with the psilocybin-induced potentiation of RSP inputs to the frontal cortical PT^{Fezf2} neurons. In control animals that received the DMSO vehicle, psilocybin increased the fraction of input cells (saline, 4.7% ± 0.2%; psilocybin, 5.9% ± 0.3%; $p = 0.03$, post hoc comparison; Figures 6D and 6E). However, this drug-evoked difference in input fraction was abolished when the neural activity in RSP was suppressed via DCZ (saline, 3.3% ± 0.2%; psilocybin, 3.2% ± 0.1%; $p = 1$; Figures 6D and 6E). We note that there was an effect for DCZ relative to control in saline animals ($p = 0.01$; Figures 6D and 6E), suggesting that lowering the neural activity also affected the efficacy of the monosynaptic tracing independent of the psilocybin administration. Although the coronal sections were intended to target RSP, we could visualize several other presynaptic regions in the same mouse. We determined the input cell fraction in presynaptic regions that previously showed

Figure 5. Psilocybin elevates the spiking activity of frontal-cortex-projecting neurons in the RSP

(A) Experimental setup.

(B) Experimental timeline.

(C) Histology showing the injection site and the probe track in RSP. Scale bars, 1 mm (left), 200 μm (right).

(D) Probe tracks for all recordings reconstructed in the Allen Mouse Brain Common Coordinate Framework. Example segment of recording from 10 consecutive probe channels.

(E) Spike raster plots for a non-tagged RSP neuron and a tagged RSP→ACAd neuron. Blue, period of laser stimulation.

(F) The time of the first spike after laser onset for all tagged RSP→ACAd neurons in saline and psilocybin groups ($p = 0.2$, two-sided two-sample Kolmogorov-Smirnov test).

(G) Pre-treatment firing rates of tagged RSP→ACAd neurons in saline and psilocybin groups. Violin plots show the distribution of firing rates with median and interquartile range. ($p = 0.3$, two-sample *t* test.)

(H) Heatmaps showing *Z* scored firing rate for all tagged RSP→ACAd neurons before and after saline administration. Scatterplot of baseline (pre) and post-saline (post) firing rates for tagged RSP→ACAd neurons. Solid symbols represent individual neurons. Different symbol shapes indicate different animals. Crosshairs, mean ± SEM. Linear mixed-effects model. See Table S2.

(I) Similar to (H) for psilocybin administration.

(J) The *Z* scored firing rate as a function of time for tagged RSP→ACAd neurons in saline and psilocybin groups. Line, mean. Shading, SEM.

(K and L) Similar to (H) and (I) for untagged neurons.

(M) Example LFP signals from the channel at a depth of 300 μm, before and after saline (top rows) or in another animal before and after psilocybin (bottom rows).

(N) Fractional change in spectral power within different frequency bands after saline or psilocybin. Circle, individual animal. Bar, mean ± SEM. Linear mixed-effects model. See Table S2.

$n = 38$ opto-tagged neurons from 6 mice for saline and 42 opto-tagged neurons from 6 mice for psilocybin.

See also Figure S7.

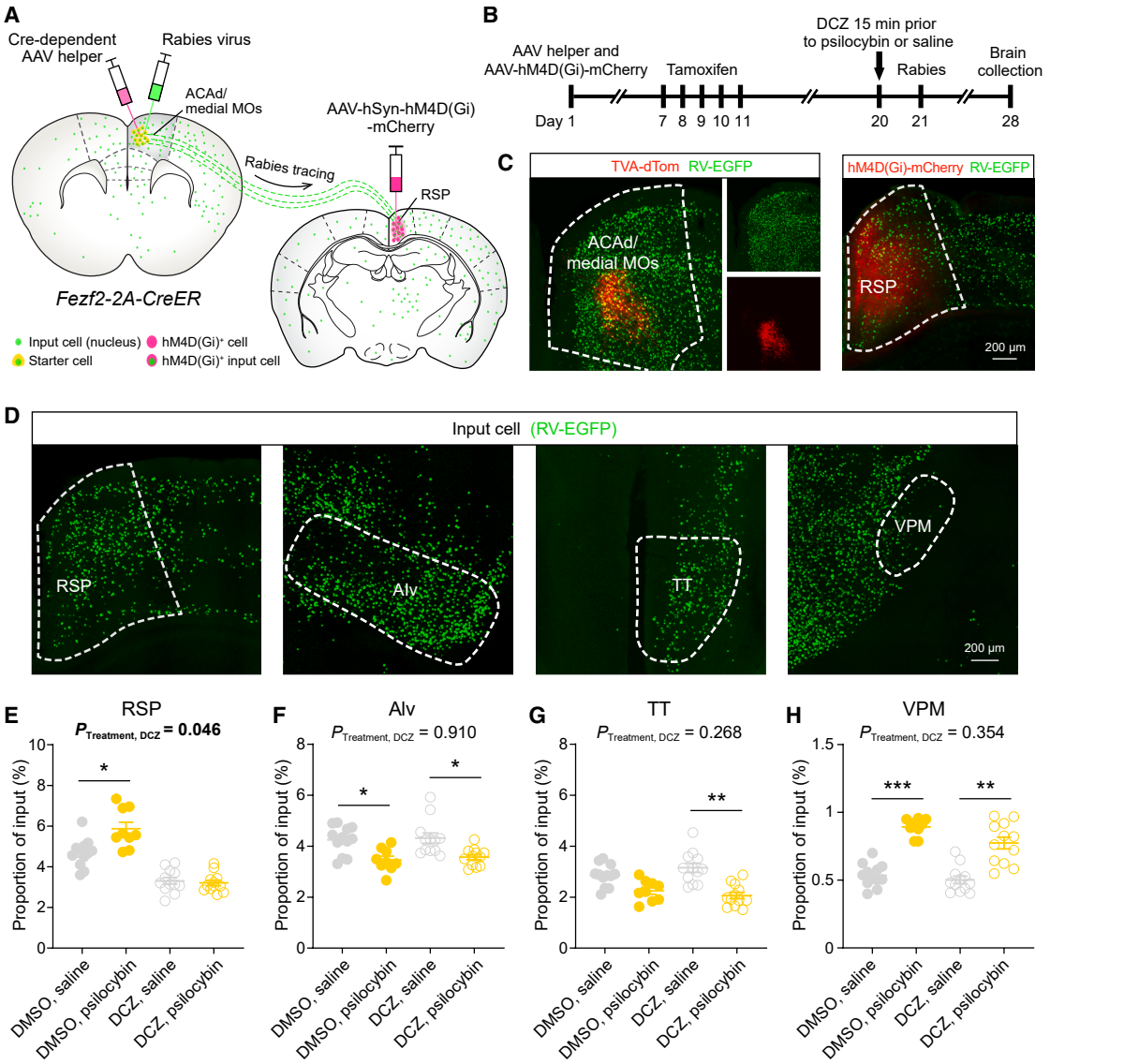

Figure 6. Chemogenetic silencing of RSP alters psilocybin-evoked rewiring of retrosplenial inputs to dorsal medial frontal cortex

(A) Experimental setup.

(B) Experimental timeline.

(C) Fluorescence images from histology after brain collection. TVA-dTom, from Cre-dependent AAV helper virus. RV, rabies virus.

(D) Fluorescence images showing input cells in RSP, AIv, TT, and VPM. Dashed line, boundary of the brain region.

(E–H) Effect of DCZ or DMSO and psilocybin or saline on the input cell fraction in RSP, AIv, TT, and VPM. Circle, individual brain slices. Line, mean ± SEM. $N = 4$ mice for DMSO + saline, 3 mice for DMSO + psilocybin, 4 mice for DCZ + saline, and 4 mice for DCZ + psilocybin. Linear mixed-effects model. See Table S2. $^{*}p < 0.05$, $^{**}p < 0.01$, $^{***}p < 0.001$. Scale bar, 200 µm for all images.

decreases after psilocybin, such as AIv of the lateral network and taenia tecta (TT) of the ventromedial prefrontal cortex, and found that the RSP manipulation had no influence because psilocybin still weakened these connections (drug and chemogenetics interaction, $p = 0.9$ for AIv and $p = 0.3$ for TT; Figures 6F and 6G). Likewise, the RSP manipulation had no detectable effect on the psilocybin-evoked increase of input fraction in the VPM (drug and chemogenetic interaction, $p = 0.4$; Figure 6H). Altogether, the results show that disrupting spiking activity in a presynaptic region influences the psilocybin-evoked rewiring process, specifically for inputs that originate from the manipulated brain region.

DISCUSSION

We found that psilocybin led to the reorganization of presynaptic inputs into the two major subtypes of pyramidal neurons in the dorsal medial frontal cortex. To conceptualize the overall impact of the changes, it is essential to consider not only the

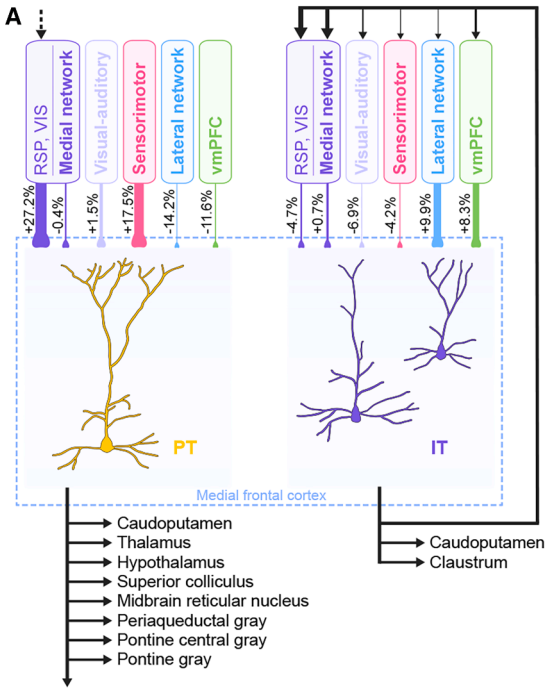

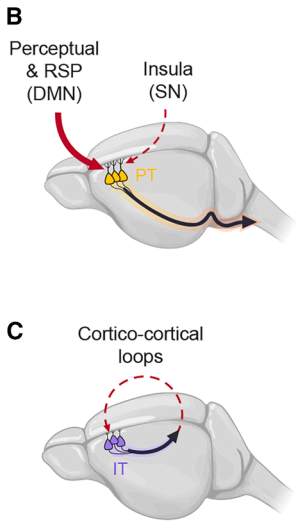

Figure 7. Impact of psilocybin on the connectivity of large-scale cortical networks

(A) Schematic depicting psilocybin's effects on frontal cortical PT^{Fezf2} and IT^{Plxnd1} neurons. Inputs to PT^{Fezf2} and IT^{Plxnd1} neurons are drawn with the line thickness directly related to the drug-evoked difference in input fraction based on Figures 1I, 2F, and 2H. Output from IT^{Plxnd1} neurons to the cortical networks is drawn with the line thickness based on Figure 2A of a prior study.[49] Dashed arrow, one subclass of PT neurons, mostly in ACAv, can project to RSP and VIS.[49]

(B) Cartoon illustration of psilocybin's impact on frontal cortical PT^{Fezf2} neurons: strengthens routing of signals from perceptual and retrosplenial regions at the expense of inputs from the insular cortex.

(C) Cartoon illustration of psilocybin's impact on frontal cortical IT^{Plxnd1} neurons: weakens connections that are part of the cortico-cortical recurrent loops.

inputs but also the output targets of the PT and IT neurons. The long-range axonal collaterals of PT and IT neurons in ACAd and medial MOs have recently been mapped at the single-neuron level.[49] PT neurons send axons to numerous destinations outside the cerebrum. IT neurons project not only to the caudoputamen and claustrum but also to various cortical networks, including most prominently to the medial network, including RSP and the visual cortex. Figure 7A is the synthesis bringing together these output patterns and our data on psilocybin's effects on presynaptic inputs. The results support two important conclusions. One, psilocybin strengthens the routing of inputs from RSP (a core region in the mouse homolog of default mode network[39–41]), visual cortex, and sensorimotor network to subcortical targets via frontal cortical PT neurons (Figure 7B). Interestingly, this shift was done at the expense of reduced influence from the lateral network (including the AIv, hypothesized to be the central seed for the mouse homolog of the salience network[41,50]) and ventromedial prefrontal cortex. Two, psilocybin weakens recurrent loops in the cortex (Figure 7C), because inputs from RSP, VIS, and other regions of the medial network are decreased in frontal cortical IT neurons. These are the cortico-cortical targets that IT neurons in the ACAd and medial MOs most strongly innervate, yet their inputs are now reduced after psilocybin.

The cell-type-specific recording and chemogenetic experiments suggest that spiking activity is a factor that determines if inputs from a presynaptic region would be strengthened by psilocybin. Although the idea may be novel for psychedelic drug action, the results align with a long history of studies demonstrating a crucial role for presynaptic activity in driving the formation of excitatory synapses during neurodevelopment. For example, deprivation of visual stimuli by raising mice in darkness reduces the number of apical dendritic spines in layer 5 neurons in the mouse visual cortex.[51] This deficit is due to the lack of presynaptic activity because the reduction of synapses can also be achieved by blocking action potentials in the optic nerve.[52] By contrast, repeated presentations of visual stimuli can induce long-term potentiation of retinotectal synapses, although presynaptic activity alone was insufficient and the plasticity also requires the firing of postsynaptic neurons.[53] In a similar vein, we surmise that while presynaptic input activity is essential for psilocybin-evoked rewiring, it is likely not sufficient on its own. Instead, we propose that more than one condition may need to be met to strengthen an input: increased presynaptic firing (demonstrated in this study) and elevated dendritic excitability in the postsynaptic neuron,[54] potentially driven by agonism of 5-HT_{2A} receptors.[55,56] For frontal cortical PT neurons, both conditions are present because the cell type exhibits elevated calcium transients in dendritic branches and spines after psilocybin administration, indicating increased dendritic excitability.[27] By contrast, psilocybin does not appear to alter dendritic excitability in frontal cortical IT neurons,[27] leaving the mechanisms underlying input modifications in these cells unclear.

This study demonstrates a potential method to sculpt the psilocybin-evoked synaptic rewiring by manipulating the activity of a presynaptic region. We tested this approach in RSP, which is a central node for the mouse homolog of the default mode network.[39–41] A function of the RSP is to represent perspectives across different spatial reference frames.[57] Psilocybin alters firing dynamics and weakens spatial encoding in RSP neurons in mice[58,59]; therefore, drug action in this retrosplenial cortical region (which is often labeled as the posteromedial cortex and precuneus[60]) may relate to the acute feeling of a temporary loss of oneself after psychedelic use in humans. This framework echoes studies pinpointing the deep posteromedial region in mediating the dissociative effects of ketamine.[45,46] Therefore, the long-range connectivity

between RSP and dorsal medial frontal cortex is of crucial importance, plausibly serving as a bridge that links the acute subjective changes with the enduring therapeutic effects. In humans, neural activity may be modulated using methods such as repetitive transcranial magnetic stimulation. Our study hints at an exciting avenue for future research to combine neuromodulation with psychedelics to precisely target specific circuits for neural plasticity.

Limitations of the study

There are limitations in this study. There is animal-to-animal variability in the input cells labeled via rabies tracing, which should be considered when interpreting the region-specific changes in input cell fraction. Moreover, based on the number of input cells, it is likely that rabies tracing does not label all cells that send monosynaptic inputs to a starter cell.[61] It is unknown if the rabies virus may favor crossing some synapses over others, for example, biases for strong synapses or synapses with certain protein composition, which could be altered by drugs. There may be tropism that prefers specific presynaptic cell types. The rabies virus is thought to spread trans-synaptically, but it is possible that viral transmission could also occur due to proximity. In a prior study, increased labeling of input cells was found in a presynaptic region that has abnormally high neural activity.[62] This should not be a confound in our study, because psilocybin has a short half-life such that the drug-evoked changes in spiking activity would have subsided when the rabies virus was injected on the next day. Due in part to these considerations, it has been argued that rabies tracing should be used as an initial screen to identify putative sources of presynaptic inputs, which then must be confirmed using other methods,[63] which echoes the approach in this study. Furthermore, we used transgenic mice to target PT^{Fezf2} and IT^{Plxnd1} neurons, which capture only a subset of the larger PT and IT cell populations in the medial frontal cortex. In slice electrophysiology, PT^{Fezf2} neurons have fluorophore and Cre recombinase expression, which may affect their physiology. Another limitation is that we only tested psilocybin. Synaptic rewiring seems to be a property shared by compounds with putative fast-acting antidepressant effects, because ketamine, 5-MeO-DMT, and other psychedelic-derived novel chemical entities similarly promote dendritic spine formation in the mouse neocortex.[13,14,16,64–66] It remains to be determined how other pharmacological interventions may exert similar or different effects on brain-wide connectivity.

RESOURCE AVAILABILITY

Lead contact

Further information and requests for resources and reagents should be directed to and will be fulfilled by the lead contact, Alex C. Kwan (alex.kwan@cornell.edu).

Materials availability

This study did not generate new, unique reagents.

Data and code availability

The following public datasets were used in this study: the Allen Mouse Brain Connectivity Atlas,[35] the Allen Mouse Brain Atlas *in situ* hybridization database for serotonin receptors (*Htr1a*, *Htr2a*, and *Htr2c*),[36] a whole-brain c-Fos light sheet imaging dataset,[37] and the Allen Brain Cell Types MERFISH dataset.[67]

The data that support the findings and the code used to analyze the data in this study are made publicly available at https://github.com/Kwan-Lab/jiang2025.

ACKNOWLEDGMENTS

We thank Catherine Chong for help with image analysis and Olesia Bilash for advice on setting up photostimulation for slice electrophysiology. Psilocybin was provided by Usona Institute's Investigational Drug & Material Supply Program, and the Usona Institute IDMSP is supported by Alexander Sherwood, Robert Kargbo, and Kristi Kaylo in Madison, WI. The authors acknowledge the support of NIH grants R01MH121848, R01MH128217, and R01MH137047 (A.C.K.); the One Mind–COMPASS Rising Star Award (A.C.K.); NIH training grant T32GM007205 (P.A.D. and N.K.S.); NIH fellowships F30DA059437 (P.A.D.) and F30MH129085 (N.K.S.); and NIH instrumentation grant S10OD032251 (Cornell Biotechnology Resource Center Imaging Facility).

AUTHOR CONTRIBUTIONS

Q.J. and A.C.K. planned the study. Q.J. performed the rabies viral tracing, Neuropixels, and chemogenetics experiments. L.-X.S. performed the two-photon imaging and slice electrophysiology experiments. P.A.D. assisted with recording for the Neuropixels experiment. J.D.N. assisted with histology for the Neuropixels experiment. S.Y. and H.Z. provided the rabies viruses. G.T., T.S.H., H.M.L., and K.T.B. provided additional reagents. Q.J. analyzed the Neuropixels and chemogenetics data. L.-X.S. analyzed the slice electrophysiology data. N.K.S. performed the transcript and c-Fos analyses. A.D.G. analyzed the two-photon imaging data. A.C.K. analyzed the rabies viral tracing and afferent data. Q.J. and A.C.K. drafted the manuscript. All authors reviewed the manuscript before submission.

DECLARATION OF INTERESTS

A.C.K. has been a scientific advisor or consultant for Boehringer Ingelheim, Eli Lilly, Empyrean Neuroscience, Freedom Biosciences, Otsuka, and Xylo Bio and has received research support from Intra-Cellular Therapies.

STAR★METHODS

Detailed methods are provided in the online version of this paper and include the following:

- KEY RESOURCES TABLE
- EXPERIMENTAL MODEL AND STUDY PARTICIPANT DETAILS
  - Animals
- METHOD DETAILS
  - Animal numbers
  - Viruses
  - Surgery
  - Whole-brain imaging after monosynaptic tracing: Light sheet fluorescence microscopy
  - Whole-brain imaging after monosynaptic tracing: Image processing and cell detection
  - Whole-brain imaging after monosynaptic tracing: Analysis of starter cells
  - Whole-brain imaging after monosynaptic tracing: Analysis of input cells
  - Axonal projection analysis
  - Serotonin receptor distribution and c-Fos analyses
  - In vivo electrophysiology: Recording procedure
  - In vivo electrophysiology: Data analysis
  - In vivo electrophysiology: Histology
  - Chemogenetics: Histology, imaging, and cell detection
  - Estimates for the number of PT, IT, PT^{Fezf2}, and $IT^{PlxinD1}$ neurons
  - Two-photon imaging: Imaging procedures
  - Two-photon imaging: Data analysis
  - Slice electrophysiology: Sample preparation

SUPPLEMENTAL INFORMATION

Supplemental information can be found online at https://doi.org/10.1016/j.cell.2025.11.009.

Received: November 27, 2024
Revised: August 6, 2025
Accepted: November 6, 2025
Published: December 5, 2025

REFERENCES

1. Nichols, D.E. (2016). Psychedelics. Pharmacol. Rev. *68*, 264–355. https://doi.org/10.1124/pr.115.011478.
2. McClure-Begley, T.D., and Roth, B.L. (2022). The promises and perils of psychedelic pharmacology for psychiatry. Nat. Rev. Drug Discov. *21*, 463–473. https://doi.org/10.1038/s41573-022-00421-7.
3. Goodwin, G.M., Aaronson, S.T., Alvarez, O., Arden, P.C., Baker, A., Bennett, J.C., Bird, C., Blom, R.E., Brennan, C., Brusch, D., et al. (2022). Single-Dose Psilocybin for a Treatment-Resistant Episode of Major Depression. N. Engl. J. Med. *387*, 1637–1648. https://doi.org/10.1056/NEJMoa2206443.
4. Carhart-Harris, R., Giribaldi, B., Watts, R., Baker-Jones, M., Murphy-Beiner, A., Murphy, R., Martell, J., Blemings, A., Erritzoe, D., and Nutt, D.J. (2021). Trial of Psilocybin versus Escitalopram for Depression. N. Engl. J. Med. *384*, 1402–1411. https://doi.org/10.1056/NEJMoa2032994.
5. Raison, C.L., Sanacora, G., Woolley, J., Heinzerling, K., Dunlop, B.W., Brown, R.T., Kakar, R., Hassman, M., Trivedi, R.P., Robison, R., et al. (2023). Single-Dose Psilocybin Treatment for Major Depressive Disorder: A Randomized Clinical Trial. JAMA *330*, 843–853. https://doi.org/10.1001/jama.2023.14530.
6. Davis, A.K., Barrett, F.S., May, D.G., Cosimano, M.P., Sepeda, N.D., Johnson, M.W., Finan, P.H., and Griffiths, R.R. (2021). Effects of Psilocybin-Assisted Therapy on Major Depressive Disorder: A Randomized Clinical Trial. JAMA Psychiatry *78*, 481–489. https://doi.org/10.1001/jamapsychiatry.2020.3285.
7. von Rotz, R., Schindowski, E.M., Jungwirth, J., Schuldt, A., Rieser, N.M., Zahoranszky, K., Seifritz, E., Nowak, A., Nowak, P., Jäncke, L., et al. (2023). Single-dose psilocybin-assisted therapy in major depressive disorder: A placebo-controlled, double-blind, randomised clinical trial. EClinicalmedicine *56*, 101809. https://doi.org/10.1016/j.eclinm.2022.101809.
8. Bogenschutz, M.P., Ross, S., Bhatt, S., Baron, T., Forcehimes, A.A., Laska, E., Mennenga, S.E., O'Donnell, K., Owens, L.T., Podrebarac, S., et al. (2022). Percentage of Heavy Drinking Days Following Psilocybin-Assisted Psychotherapy vs Placebo in the Treatment of Adult Patients With Alcohol Use Disorder: A Randomized Clinical Trial. JAMA Psychiatry *79*, 953–962. https://doi.org/10.1001/jamapsychiatry.2022.2096.
9. Kwan, A.C., Olson, D.E., Preller, K.H., and Roth, B.L. (2022). The neural basis of psychedelic action. Nat. Neurosci. *25*, 1407–1419. https://doi.org/10.1038/s41593-022-01177-4.
10. Kang, H.J., Voleti, B., Hajszan, T., Rajkowska, G., Stockmeier, C.A., Licznerski, P., Lepack, A., Majik, M.S., Jeong, L.S., Banasr, M., et al. (2012). Decreased expression of synapse-related genes and loss of synapses in major depressive disorder. Nat. Med. *18*, 1413–1417. https://doi.org/10.1038/nm.2886.
11. Holmes, S.E., Scheinost, D., Finnema, S.J., Naganawa, M., Davis, M.T., DellaGioia, N., Nabulsi, N., Matuskey, D., Angarita, G.A., Pietrzak, R.H., et al. (2019). Lower synaptic density is associated with depression severity and network alterations. Nat. Commun. *10*, 1529. https://doi.org/10.1038/s41467-019-09562-7.
12. Li, N., Lee, B., Liu, R.J., Banasr, M., Dwyer, J.M., Iwata, M., Li, X.Y., Aghajanian, G., and Duman, R.S. (2010). mTOR-dependent synapse formation underlies the rapid antidepressant effects of NMDA antagonists. Science *329*, 959–964. https://doi.org/10.1126/science.1190287.
13. Phoumthipphavong, V., Barthas, F., Hassett, S., and Kwan, A.C. (2016). Longitudinal Effects of Ketamine on Dendritic Architecture In Vivo in the Mouse Medial Frontal Cortex. E.Neuro. *3*. ENEURO.0133-15.2016. https://doi.org/10.1523/ENEURO.0133-15.2016.
14. Moda-Sava, R.N., Murdock, M.H., Parekh, P.K., Fetcho, R.N., Huang, B.S., Huynh, T.N., Witztum, J., Shaver, D.C., Rosenthal, D.L., Alway, E.J., et al. (2019). Sustained rescue of prefrontal circuit dysfunction by antidepressant-induced spine formation. Science *364*, eaat8078. https://doi.org/10.1126/science.aat8078.
15. Shao, L.X., Liao, C., Gregg, I., Davoudian, P.A., Savalia, N.K., Delagarza, K., and Kwan, A.C. (2021). Psilocybin induces rapid and persistent growth of dendritic spines in frontal cortex in vivo. Neuron *109*, 2535–2544.e4. https://doi.org/10.1016/j.neuron.2021.06.008.
16. Jefferson, S.J., Gregg, I., Dibbs, M., Liao, C., Wu, H., Davoudian, P.A., Woodburn, S.C., Wehrle, P.H., Sprouse, J.S., Sherwood, A.M., et al. (2023). 5-MeO-DMT modifies innate behaviors and promotes structural neural plasticity in mice. Neuropsychopharmacology *48*, 1257–1266. https://doi.org/10.1038/s41386-023-01572-w.
17. Holze, F., Becker, A.M., Kolaczynska, K.E., Duthaler, U., and Liechti, M.E. (2023). Pharmacokinetics and Pharmacodynamics of Oral Psilocybin Administration in Healthy Participants. Clin. Pharmacol. Ther. *113*, 822–831. https://doi.org/10.1002/cpt.2821.
18. Zingg, B., Hintiryan, H., Gou, L., Song, M.Y., Bay, M., Bienkowski, M.S., Foster, N.N., Yamashita, S., Bowman, I., Toga, A.W., et al. (2014). Neural networks of the mouse neocortex. Cell *156*, 1096–1111. https://doi.org/10.1016/j.cell.2014.02.023.
19. Anastasiades, P.G., and Carter, A.G. (2021). Circuit organization of the rodent medial prefrontal cortex. Trends Neurosci. *44*, 550–563. https://doi.org/10.1016/j.tins.2021.03.006.
20. Ährlund-Richter, S., Xuan, Y., van Lunteren, J.A., Kim, H., Ortiz, C., Pollak Dorocic, I., Meletis, K., and Carlén, M. (2019). A whole-brain atlas of monosynaptic input targeting four different cell types in the medial prefrontal cortex of the mouse. Nat. Neurosci. *22*, 657–668. https://doi.org/10.1038/s41593-019-0354-y.
21. Callaway, E.M., and Luo, L. (2015). Monosynaptic Circuit Tracing with Glycoprotein-Deleted Rabies Viruses. J. Neurosci. *35*, 8979–8985. https://doi.org/10.1523/jneurosci.0409-15.2015.
22. Matho, K.S., Huilgol, D., Galbavy, W., He, M., Kim, G., An, X., Lu, J., Wu, P., Di Bella, D.J., Shetty, A.S., et al. (2021). Genetic dissection of the glutamatergic neuron system in cerebral cortex. Nature *598*, 182–187. https://doi.org/10.1038/s41586-021-03955-9.
23. Kim, Y., Perova, Z., Mirrione, M.M., Pradhan, K., Henn, F.A., Shea, S., Osten, P., and Li, B. (2016). Whole-Brain Mapping of Neuronal Activity in the Learned Helplessness Model of Depression. Front. Neural Circuits *10*, 3. https://doi.org/10.3389/fncir.2016.00003.
24. Davoudian, P.A., Shao, L.X., and Kwan, A.C. (2023). Shared and Distinct Brain Regions Targeted for Immediate Early Gene Expression by Ketamine and Psilocybin. ACS Chem. Neurosci. *14*, 468–480. https://doi.org/10.1021/acschemneuro.2c00637.
25. Baker, A., Kalmbach, B., Morishima, M., Kim, J., Juavinett, A., Li, N., and Dembrow, N. (2018). Specialized Subpopulations of Deep-Layer Pyramidal Neurons in the Neocortex: Bridging Cellular Properties to Functional Consequences. J. Neurosci. *38*, 5441–5455. https://doi.org/10.1523/JNEUROSCI.0150-18.2018.
26. Shepherd, G.M.G. (2013). Corticostriatal connectivity and its role in disease. Nat. Rev. Neurosci. *14*, 278–291. https://doi.org/10.1038/nrn3469.

27. Shao, L.X., Liao, C., Davoudian, P.A., Savalia, N.K., Jiang, Q., Wojtasiewicz, C., Tan, D., Nothnagel, J.D., Liu, R.J., Woodburn, S.C., et al. (2025). Psilocybin's lasting action requires pyramidal cell types and 5-HT(2A) receptors. Nature *642*, 411–420. https://doi.org/10.1038/s41586-025-08813-6.

28. Wang, Q., Ding, S.L., Li, Y., Royall, J., Feng, D., Lesnar, P., Graddis, N., Naeemi, M., Facer, B., Ho, A., et al. (2020). The Allen Mouse Brain Common Coordinate Framework: A 3D Reference Atlas. Cell *181*, 936–953.e20. https://doi.org/10.1016/j.cell.2020.04.007.

29. Kim, E.J., Juavinett, A.L., Kyubwa, E.M., Jacobs, M.W., and Callaway, E.M. (2015). Three Types of Cortical Layer 5 Neurons That Differ in Brain-wide Connectivity and Function. Neuron *88*, 1253–1267. https://doi.org/10.1016/j.neuron.2015.11.002.

30. Tudi, A., Yao, M., Tang, F., Zhou, J., Li, A., Gong, H., Jiang, T., and Li, X. (2024). Subregion preference in the long-range connectome of pyramidal neurons in the medial prefrontal cortex. BMC Biol. *22*, 95. https://doi.org/10.1186/s12915-024-01880-7.

31. Yao, M., Tudi, A., Jiang, T., An, X., Sun, Q., Li, A., Huang, Z.J., Gong, H., and Li, X. (2023). Long-range connectome of pyramidal neurons in the sensorimotor cortex. iScience *26*, 106316. https://doi.org/10.1016/j.isci.2023.106316.

32. Musall, S., Sun, X.R., Mohan, H., An, X., Gluf, S., Li, S.J., Drewes, R., Cravo, E., Lenzi, I., Yin, C., et al. (2023). Pyramidal cell types drive functionally distinct cortical activity patterns during decision-making. Nat. Neurosci. *26*, 495–505. https://doi.org/10.1038/s41593-022-01245-9.

33. Tang, L., and Higley, M.J. (2020). Layer 5 Circuits in V1 Differentially Control Visuomotor Behavior. Neuron *105*, 346–354.e5. https://doi.org/10.1016/j.neuron.2019.10.014.

34. Li, N., Chen, T.W., Guo, Z.V., Gerfen, C.R., and Svoboda, K. (2015). A motor cortex circuit for motor planning and movement. Nature *519*, 51–56. https://doi.org/10.1038/nature14178.

35. Oh, S.W., Harris, J.A., Ng, L., Winslow, B., Cain, N., Mihalas, S., Wang, Q., Lau, C., Kuan, L., Henry, A.M., et al. (2014). A mesoscale connectome of the mouse brain. Nature *508*, 207–214. https://doi.org/10.1038/nature13186.

36. Lein, E.S., Hawrylycz, M.J., Ao, N., Ayres, M., Bensinger, A., Bernard, A., Boe, A.F., Boguski, M.S., Brockway, K.S., Byrnes, E.J., et al. (2007). Genome-wide atlas of gene expression in the adult mouse brain. Nature *445*, 168–176. https://doi.org/10.1038/nature05453.

37. Aboharb, F., Davoudian, P.A., Shao, L.X., Liao, C., Rzepka, G.N., Wojtasiewicz, C., Indajang, J., Dibbs, M., Rondeau, J., Sherwood, A.M., et al. (2025). Classification of psychedelics and psychoactive drugs based on brain-wide imaging of cellular c-Fos expression. Nat. Commun. *16*, 1590. https://doi.org/10.1038/s41467-025-56850-6.

38. Yamawaki, N., Radulovic, J., and Shepherd, G.M.G. (2016). A Corticocortical Circuit Directly Links Retrosplenial Cortex to M2 in the Mouse. J. Neurosci. *36*, 9365–9374. https://doi.org/10.1523/JNEUROSCI.1099-16.2016.

39. Stafford, J.M., Jarrett, B.R., Miranda-Dominguez, O., Mills, B.D., Cain, N., Mihalas, S., Lahvis, G.P., Lattal, K.M., Mitchell, S.H., David, S.V., et al. (2014). Large-scale topology and the default mode network in the mouse connectome. Proc. Natl. Acad. Sci. USA *111*, 18745–18750. https://doi.org/10.1073/pnas.1404346111.

40. Whitesell, J.D., Liska, A., Coletta, L., Hirokawa, K.E., Bohn, P., Williford, A., Groblewski, P.A., Graddis, N., Kuan, L., Knox, J.E., et al. (2021). Regional, Layer, and Cell-Type-Specific Connectivity of the Mouse Default Mode Network. Neuron *109*, 545–559.e8. https://doi.org/10.1016/j.neuron.2020.11.011.

41. Gozzi, A., and Schwarz, A.J. (2016). Large-scale functional connectivity networks in the rodent brain. NeuroImage *127*, 496–509. https://doi.org/10.1016/j.neuroimage.2015.12.017.

42. Preller, K.H., Duerler, P., Burt, J.B., Ji, J.L., Adkinson, B., Stämpfli, P., Seifritz, E., Repovš, G., Krystal, J.H., Murray, J.D., et al. (2020). Psilocybin Induces Time-Dependent Changes in Global Functional Connectivity. Biol. Psychiatry *88*, 197–207. https://doi.org/10.1016/j.biopsych.2019.12.027.

43. Carhart-Harris, R.L., Erritzoe, D., Williams, T., Stone, J.M., Reed, L.J., Colasanti, A., Tyacke, R.J., Leech, R., Malizia, A.L., Murphy, K., et al. (2012). Neural correlates of the psychedelic state as determined by fMRI studies with psilocybin. Proc. Natl. Acad. Sci. USA *109*, 2138–2143. https://doi.org/10.1073/pnas.1119598109.

44. Siegel, J.S., Subramanian, S., Perry, D., Kay, B.P., Gordon, E.M., Laumann, T.O., Reneau, T.R., Metcalf, N.V., Chacko, R.V., Gratton, C., et al. (2024). Psilocybin desynchronizes the human brain. Nature *632*, 131–138. https://doi.org/10.1038/s41586-024-07624-5.

45. Vesuna, S., Kauvar, I.V., Richman, E., Gore, F., Oskotsky, T., Sava-Segal, C., Luo, L., Malenka, R.C., Henderson, J.M., Nuyujukian, P., et al. (2020). Deep posteromedial cortical rhythm in dissociation. Nature *586*, 87–94. https://doi.org/10.1038/s41586-020-2731-9.

46. Tian, F., Lewis, L.D., Zhou, D.W., Balanza, G.A., Paulk, A.C., Zelmann, R., Peled, N., Soper, D., Santa Cruz Mercado, L.A., Peterfreund, R.A., et al. (2023). Characterizing brain dynamics during ketamine-induced dissociation and subsequent interactions with propofol using human intracranial neurophysiology. Nature Commun *14*. https://doi.org/10.1038/s41467-023-37463-3.

47. Armbruster, B.N., Li, X., Pausch, M.H., Herlitze, S., and Roth, B.L. (2007). Evolving the lock to fit the key to create a family of G protein-coupled receptors potently activated by an inert ligand. Proc. Natl. Acad. Sci. USA *104*, 5163–5168. https://doi.org/10.1073/pnas.0700293104.

48. Nagai, Y., Miyakawa, N., Takuwa, H., Hori, Y., Oyama, K., Ji, B., Takahashi, M., Huang, X.P., Slocum, S.T., DiBerto, J.F., et al. (2020). Deschloroclozapine, a potent and selective chemogenetic actuator enables rapid neuronal and behavioral modulations in mice and monkeys. Nat. Neurosci. *23*, 1157–1167. https://doi.org/10.1038/s41593-020-0661-3.

49. Gao, L., Liu, S., Gou, L., Hu, Y., Liu, Y., Deng, L., Ma, D., Wang, H., Yang, Q., Chen, Z., et al. (2022). Single-neuron projectome of mouse prefrontal cortex. Nat. Neurosci. *25*, 515–529. https://doi.org/10.1038/s41593-022-01041-5.

50. Mandino, F., Vrooman, R.M., Foo, H.E., Yeow, L.Y., Bolton, T.A.W., Salvan, P., Teoh, C.L., Lee, C.Y., Beauchamp, A., Luo, S., et al. (2021). A triple-network organization for the mouse brain. Mol. Psychiatry *27*, 865–872. https://doi.org/10.1038/s41380-021-01298-5.

51. Valverde, F. (1967). Apical dendritic spines of the visual cortex and light deprivation in the mouse. Exp. Brain Res. *3*, 337–352. https://doi.org/10.1007/BF00237559.

52. Riccio, R.V., and Matthews, M.A. (1985). The Postnatal Development of the Rat Primary Visual Cortex during Optic Nerve Impulse Blockade by Intraocular Tetrodotoxin: a Quantitative Electron Microscopic Analysis. Brain Res. *352*, 55–68. https://doi.org/10.1016/0165-3806(85)90087-2.

53. Engert, F., Tao, H.W., Zhang, L.I., and Poo, M.M. (2002). Moving visual stimuli rapidly induce direction sensitivity of developing tectal neurons. Nature *419*, 470–475. https://doi.org/10.1038/nature00988.

54. Savalia, N.K., Shao, L.X., and Kwan, A.C. (2021). A Dendrite-Focused Framework for Understanding the Actions of Ketamine and Psychedelics. Trends Neurosci. *44*, 260–275. https://doi.org/10.1016/j.tins.2020.11.008.

55. de la Fuente Revenga, M., Zhu, B., Guevara, C.A., Naler, L.B., Saunders, J.M., Zhou, Z., Toneatti, R., Sierra, S., Wolstenholme, J.T., Beardsley, P.M., et al. (2021). Prolonged epigenomic and synaptic plasticity alterations following single exposure to a psychedelic in mice. Cell Rep. *37*, 109836. https://doi.org/10.1016/j.celrep.2021.109836.

56. Cameron, L.P., Patel, S.D., Vargas, M.V., Barragan, E.V., Saeger, H.N., Warren, H.T., Chow, W.L., Gray, J.A., and Olson, D.E. (2023). 5-HT2ARs Mediate Therapeutic Behavioral Effects of Psychedelic Tryptamines. ACS Chem. Neurosci. *14*, 351–358. https://doi.org/10.1021/acschemneuro.2c00718.

57. Alexander, A.S., and Nitz, D.A. (2015). Retrosplenial cortex maps the conjunction of internal and external spaces. Nat. Neurosci. *18*, 1143–1151. https://doi.org/10.1038/nn.4058.

58. Ivan, V.E., Tomàs-Cuesta, D.P., Esteves, I.M., Luczak, A., Mohajerani, M., McNaughton, B.L., and Gruber, A.J. (2024). Psilocybin reduces functional correlation and the encoding of spatial information by neurons in mouse retrosplenial cortex. Eur. J. Neurosci. *60*, 6395–6407. https://doi.org/10.1111/ejn.16558.

59. Rogers, S.A., Heller, E.A., and Corder, G. (2025). Psilocybin-enhanced fear extinction linked to bidirectional modulation of cortical ensembles. Nat. Neurosci. *28*, 1311–1326. https://doi.org/10.1038/s41593-025-01964-9.

60. Willbrand, E.H., Parker, B.J., Voorhies, W.I., Miller, J.A., Lyu, I., Hallock, T., Aponik-Gremillion, L., Koslov, S.R., Alzheimer's Disease Neuroimaging Initiative, and Bunge, S.A., et al. (2022). Uncovering a tripartite landmark in posterior cingulate cortex. Sci. Adv. *8*, eabn9516. https://doi.org/10.1126/sciadv.abn9516.

61. Patiño, M., Lagos, W.N., Patne, N.S., Miyazaki, P.A., Bhamidipati, S.K., Collman, F., and Callaway, E.M. (2023). Postsynaptic cell type and synaptic distance do not determine efficiency of monosynaptic rabies virus spread measured at synaptic resolution. eLife *12*, e89297. https://doi.org/10.7554/eLife.89297.

62. Beier, K.T., Kim, C.K., Hoerbelt, P., Hung, L.W., Heifets, B.D., DeLoach, K.E., Mosca, T.J., Neuner, S., Deisseroth, K., Luo, L., et al. (2017). Rabies screen reveals GPe control of cocaine-triggered plasticity. Nature *549*, 345–350. https://doi.org/10.1038/nature23888.

63. Luo, L., Callaway, E.M., and Svoboda, K. (2018). Genetic Dissection of Neural Circuits: A Decade of Progress. Neuron *98*, 256–281. https://doi.org/10.1016/j.neuron.2018.03.040.

64. Liao, C., Dua, A.N., Wojtasiewicz, C., Liston, C., and Kwan, A.C. (2025). Structural neural plasticity evoked by rapid-acting antidepressant interventions. Nat. Rev. Neurosci. *26*, 101–114. https://doi.org/10.1038/s41583-024-00876-0.

65. Cameron, L.P., Tombari, R.J., Lu, J., Pell, A.J., Hurley, Z.Q., Ehinger, Y., Vargas, M.V., McCarroll, M.N., Taylor, J.C., Myers-Turnbull, D., et al. (2021). A non-hallucinogenic psychedelic analogue with therapeutic potential. Nature *589*, 474–479. https://doi.org/10.1038/s41586-020-3008-z.

66. Lu, J., Tjia, M., Mullen, B., Cao, B., Lukasiewicz, K., Shah-Morales, S., Weiser, S., Cameron, L.P., Olson, D.E., Chen, L., et al. (2021). An analog of psychedelics restores functional neural circuits disrupted by unpredictable stress. Mol. Psychiatry *26*, 6237–6252. https://doi.org/10.1038/s41380-021-01159-1.

67. Yao, Z., van Velthoven, C.T.J., Kunst, M., Zhang, M., McMillen, D., Lee, C., Jung, W., Goldy, J., Abdelhak, A., Aitken, M., et al. (2023). A high-resolution transcriptomic and spatial atlas of cell types in the whole mouse brain. Nature *624*, 317–332. https://doi.org/10.1038/s41586-023-06812-z.

68. Yao, S., Wang, Q., Hirokawa, K.E., Ouellette, B., Ahmed, R., Bomben, J., Brouner, K., Casal, L., Caldejon, S., Cho, A., et al. (2023). A whole-brain monosynaptic input connectome to neuron classes in mouse visual cortex. Nat. Neurosci. *26*, 350–364. https://doi.org/10.1038/s41593-022-01219-x.

69. Miyamichi, K., Shlomai-Fuchs, Y., Shu, M., Weissbourd, B.C., Luo, L., and Mizrahi, A. (2013). Dissecting Local Circuits: Parvalbumin Interneurons Underlie Broad Feedback Control of Olfactory Bulb Output. Neuron *80*, 1232–1245. https://doi.org/10.1016/j.neuron.2013.08.027.

70. Reardon, T.R., Murray, A.J., Turi, G.F., Wirblich, C., Croce, K.R., Schnell, M.J., Jessell, T.M., and Losonczy, A. (2016). Rabies Virus CVS-N2c(DeltaG) Strain Enhances Retrograde Synaptic Transfer and Neuronal Viability. Neuron *89*, 711–724. https://doi.org/10.1016/j.neuron.2016.01.004.

71. Shelhamer, E., Long, J., and Darrell, T. (2016). Fully Convolutional Networks for Semantic Segmentation. arXiv, 1605.06211. https://doi.org/10.48550/arXiv.1605.06211.

72. He, K., Zhang, X., Ren, S., and Sun, J. (2016). Deep residual learning for image recognition. Proceedings of the IEEE Conference on Computer Vision and Pattern Recognition (CVPR), 770–778. https://doi.org/10.1109/CVPR.2016.90.

73. Kosaka, K., Sawai, K., Tanaka, C., Imafuji, M., Kamei, A., and Kosaka, T. (2009). Distinct domanial and lamellar distribution of clustered lipofuscin granules in microglia in the main olfactory bulb of young mice. Neurosci. Res. *65*, 286–295. https://doi.org/10.1016/j.neures.2009.08.001.

74. Fulcher, B.D., Murray, J.D., Zerbi, V., and Wang, X.J. (2019). Multimodal gradients across mouse cortex. Proc. Natl. Acad. Sci. USA *116*, 4689–4695. https://doi.org/10.1073/pnas.1814144116.

75. Buccino, A.P., Hurwitz, C.L., Garcia, S., Magland, J., Siegle, J.H., Hurwitz, R., and Hennig, M.H. (2020). SpikeInterface, a unified framework for spike sorting. eLife *9*, e61834. https://doi.org/10.7554/eLife.61834.

76. Steinmetz, N.A., Aydin, C., Lebedeva, A., Okun, M., Pachitariu, M., Bauza, M., Beau, M., Bhagat, J., Böhm, C., Broux, M., et al. (2021). Neuropixels 2.0: A miniaturized high-density probe for stable, long-term brain recordings. Science *372*, eabf4588. https://doi.org/10.1126/science.abf4588.

77. Pachitariu, M., Sridhar, S., and Stringer, C. (2023). Solving the spike sorting problem with Kilosort. Preprint at bioRxiv. https://doi.org/10.1101/2023.01.07.523036.

78. Hill, D.N., Mehta, S.B., and Kleinfeld, D. (2011). Quality metrics to accompany spike sorting of extracellular signals. J. Neurosci. *31*, 8699–8705. https://doi.org/10.1523/JNEUROSCI.0971-11.2011.

79. Penttonen, M., and Buzsáki, G. (2003). Natural logarithmic relationship between brain oscillators. Thalamus Relat. Syst. *2*, 145–152. https://doi.org/10.1017/S1472928803000074.

80. Shamash, P., Carandini, M., Harris, K.D., and Steinmetz, N.A. (2018). A tool for analyzing electrode tracks from slice histology. Preprint at biorxiv. https://doi.org/10.1101/447995.

81. Claudi, F., Tyson, A.L., Petrucco, L., Margrie, T.W., Portugues, R., and Branco, T. (2021). Visualizing anatomically registered data with brainrender. eLife *10*, e65751. https://doi.org/10.7554/eLife.65751.

82. Yates, S.C., Groeneboom, N.E., Coello, C., Lichtenthaler, S.F., Kuhn, P.H., Demuth, H.U., Hartlage-Rübsamen, M., Roßner, S., Leergaard, T., Kreshuk, A., et al. (2019). QUINT: Workflow for Quantification and Spatial Analysis of Features in Histological Images From Rodent Brain. Front. Neuroinform. *13*, 75. https://doi.org/10.3389/fninf.2019.00075.

83. Groeneboom, N.E., Yates, S.C., Puchades, M.A., and Bjaalie, J.G. (2020). Nutil: A Pre- and Post-processing Toolbox for Histological Rodent Brain Section Images. Front. Neuroinform. *14*, 37. https://doi.org/10.3389/fninf.2020.00037.

84. Puchades, M.A., Csucs, G., Ledergerber, D., Leergaard, T.B., and Bjaalie, J.G. (2019). Spatial registration of serial microscopic brain images to three-dimensional reference atlases with the QuickNII tool. PLoS One *14*, e0216796. https://doi.org/10.1371/journal.pone.0216796.

85. Berg, S., Kutra, D., Kroeger, T., Straehle, C.N., Kausler, B.X., Haubold, C., Schiegg, M., Ales, J., Beier, T., Rudy, M., et al. (2019). ilastik: interactive machine learning for (bio)image analysis. Nat. Methods *16*, 1226–1232. https://doi.org/10.1038/s41592-019-0582-9.

STAR★METHODS

KEY RESOURCES TABLE

REAGENT or RESOURCE	SOURCE	IDENTIFIER
Antibodies		
Mouse Monoclonal Antibody to FOX3/NeuN	Encor Biotechnology	Cat# MCA-1B7; RRID:AB_2572267
Mouse anti-NeuN	Millipore	Cat# MAB377; RRID:AB_2298772
Bacterial and virus strains		
AAV1-hSyn-DIO-TVA66T-dTom-CVS N2c G	Allen Institute	N/A
AAV1-hSyn-DIO-TVA66T-dTom	Allen Institute	N/A
EnvA-CVS N2cΔG-H2B-EGFP	Allen Institute	N/A
AAVretro-hSyn-Cre-WPRE-hGH	Addgene	Cat# 105553-AAVrg
AAV1-pCAG-FLEX-EGFP-WPRE	Addgene	Cat# 51502-AAV1
AAV9-hSyn-hM4D(Gi)-mCherry	Addgene	Cat# 50475-AAV9
AAV9-mDlx-GFP-Fishell-1	Addgene	Cat# 83900-AAV9
AAV1-FLEX-tdTomato	Addgene	Cat# 28306-AAV1
AAV9-hSyn-hChR2(H134R)-EYFP	Addgene	Cat# 26973-AAV9
AAV9-hSyn-Synaptophysin-mRuby2-WPRE-polyA	This paper	Custom-made from BrainVTA
Chemicals, peptides, and recombinant proteins		
Dexamethasone	Bimeda	Cat# 1DEX022
Carprofen	Covetrus	Cat# 059149
Psilocybin	Usona Institute	N/A
HEPES solution	Sigma-Aldrich	Cat# H3537
Sodium chloride solution	Sigma-Aldrich	Cat# S5150
Potassium chloride solution	Sigma-Aldrich	Cat# 60142
Calcium chloride solution	Sigma-Aldrich	Cat# 21115
Magnesium chloride solution	Sigma-Aldrich	Cat# 63069
Formaldehyde solution	Sigma-Aldrich	Cat# F8775
Phosphate buffered saline	Sigma-Aldrich	Cat# P4474
Tamoxifen	Sigma-Aldrich	Cat# T5648
Corn oil	Sigma-Aldrich	Cat# C8267
Heparin sodium salt	Sigma-Aldrich	Cat# H3149
Choline chloride	Sigma-Aldrich	Cat# C1879
Sodium bicarbonate	Sigma-Aldrich	Cat# S6014
Sodium phosphate monobasic dihydrate	Sigma-Aldrich	Cat# 71505
Sodium ascorbate	Sigma-Aldrich	Cat# 11140
Sodium pyruvate	Sigma-Aldrich	Cat# P2256
Glucose	Sigma-Aldrich	Cat# G8270
Cesium methanesulfonate	Sigma-Aldrich	Cat# C1426
Sodium chloride	Sigma-Aldrich	Cat# 71376
EGTA (Ethylene glycol-bis (2-aminoethylether)-*N*,*N*,*N*′, *N*′-tetraacetic acid)	Sigma-Aldrich	Cat# E4378
Mg-ATP (Adenosine 5′-triphosphate magnesium salt)	Sigma-Aldrich	Cat# A9187
Na-GTP (Guanosine 5′-triphosphate sodium salt hydrate)	Sigma-Aldrich	Cat# G8877

(*Continued on next page*)

Continued

REAGENT or RESOURCE	SOURCE	IDENTIFIER
Na-phosphocreatine (Phosphocreatine disodium salt hydrate)	Sigma-Aldrich	Cat# P7936
CsOH (Cesium hydroxide)	Thermo Fisher Scientific	Cat# 213601000
Deschloroclozapine	MedChemExpress	Cat# HY-42110
Mounting Medium with DAPI	Vector Laboratories	Cat# H-1200-10
Mounting Medium without DAPI	Vector Laboratories	Cat# H-1400-10
CM-DiI Dye	ThermoFisher	Cat# C7000
Tergazyme	Alconox Inc	Cat# 1304-1
Sodium azide 5%	VWR	Cat# BDH7465-2
Tetrodotoxin	Tocris Bioscience	Cat# 1078/1
4-Aminopyridine	Tocris Bioscience	Cat# 0940/100
Isopropyl alcohol	AmericanBio	Cat# AB07015
Normal donkey serum	Abcam	Cat# ab7475
Deposited data		
Allen Mouse Brain Connectivity Atlas	Oh et al.[35]	https://doi.org/10.1038/nature13186
Allen Mouse Brain Atlas gene expression database (Htr1a, Htr2a, Htr2c expression)	Lein et al.[36]	https://doi.org/10.1038/nature05453
Whole-brain c-Fos light sheet imaging dataset	Aboharb et al.[37]	https://doi.org/10.1038/s41467-025-56850-6
Allen Brain Cell Types MERFISH dataset	Yao et al.[67]	https://doi.org/10.1038/s41586-023-06812-z
Whole-brain rabies viral tracing dataset acquired with light-sheet imaging, along with the associated analysis code	This paper	https://github.com/Kwan-Lab/jiang2025
Experimental models: Organisms/strains		
C57BL/6J	Jackson Labs	Cat# 000664
B6;129S4-*Fezf2*$^{tm1.1(cre/ERT2)Zjh}$/J	Jackson Labs	Cat# 036296
B6;129S4-*Plxnd1*$^{tm1.1(cre/ERT2)Zjh}$/J	Jackson Labs	Cat# 036294
B6.Cg-*Gt(ROSA)26Sor*$^{tm32(CAG-COP4*H134R/EYFP)Hze}$/J	Jackson Labs	Cat# 024109
B6.Cg-*Gt(ROSA)26Sor*$^{tm14(CAG-tdTomato)Hze}$/J	Jackson Labs	Cat# 007914
B6.Cg-*Gt(ROSA)26Sor*$^{tm75.1(CAG-tdTomato*)Hze}$/J	Jackson Labs	Cat# 025106
Software and algorithms		
MATLAB	MathWorks	https://www.mathworks.com/
ImageJ	NIH	
Prism 10	GraphPad Software	http://www.graphpad.com/scientific-software/pris
Visual Studio Code	Microsoft	https://code.visualstudio.com/
R	R Core Team	https://www.r-project.org/
Clampfit 10.4	Molecular Devices	N/A
Other		
Small Animal Stereotaxic Instrument	David Kopf Instruments	Cat# Model 900
Optixcare Eye Lube	Covetrus North America	Cat# 062143
Far Infrared Warming Pad	Kent Scientific	Cat# RT-0515
Brush Type Control Unit	Foredom	Cat# HP4-917
Self-Tapping Bone Screws	Fine Science Tools	Cat# 19010-10
C&B Metabond® Quick Adhesive Cement System	Parkell	Cat# S380
Stereotaxic Headplate	eMachineShop	https://github.com/Kwan-Lab/behavioral-rigs
Round coverslips	Warner Instruments	Cat# 64-0720
Intravenous catheter system (Saf-T-Intima Closed IV Catheter System)	Becton, Dickinson and Company (BD)	Cat# 383323

(*Continued on next page*)

Continued

REAGENT or RESOURCE	SOURCE	IDENTIFIER
Neuropixels 1.0 probe	IMEC	Cat# PRB_1_4_0480_1_C
Handheld dental drill	Foredom	Cat# HP4-917
Surgical sutures	Surgical Specialties Corporation	Cat# 1265B
Silicone elastomer (Body Double Fast Set)	Smooth-On	Cat# 10006546
Ultraviolet-curable optical adhesive (NOA 61)	Norland Products	N/A
Ultraviolet illuminator	Henkel	Cat# 2182210
Tungsten Needles	Fine Science Tools	Cat# 10130-10
Surgifoam	Ethicon	Cat# 1972
Vetbond tissue adhesive	3M Company	Cat# 1469SB

EXPERIMENTAL MODEL AND STUDY PARTICIPANT DETAILS

Animals

Fezf2-2A-CreER (B6;129S4-*Fezf2*$^{tm1.1(cre/ERT2)Zjh}$/J, Stock No. 036296),[22] *PlexinD1-2A-CreER* (B6;129S4-*Plxnd1*$^{tm1.1(cre/ERT2)Zjh}$/J, Stock No. 036294),[22] *Ai32* (B6.Cg-*Gt(ROSA)26Sor*$^{tm32(CAG-COP4*H134R/EYFP)Hze}$/J, Stock No. 024109), *Ai14* (B6.Cg-*Gt(ROSA)26-Sor*$^{tm14(CAG-tdTomato)Hze}$/J, Stock No. 007914), *Ai75* (B6.Cg-*Gt(ROSA)26Sor*$^{tm75.1(CAG-tdTomato*)Hze}$/J, Stock No. 025106) and wild-type C57BL/6J (Stock No. 000664) mice were acquired from Jackson Laboratory and bred in our animal facility. For tracing experiments involving G-deleted rabies virus and adeno-associated virus (AAV), homozygous 2- to 3-month-old *Fezf2-2A-CreER* and *PlexinD1-2A-CreER* mice of both sexes were used. For Neuropixels studies, 2- to 3-month-old *Ai32* mice of both sexes were used. For two-photon imaging studies, 5- to 7-week-old mice of both sexes were used. Animals were housed in groups of 2 to 5 per cage in a temperature-controlled room, maintained on a standard 12-hour light/dark cycle (lights on from 8:00 AM to 8:00 PM). Food and water were provided *ad libitum*. Animals were randomly assigned to experimental groups. All animal care and experimental procedures were approved by the Institutional Animal Care and Use Committee (IACUC) at Cornell University.

METHOD DETAILS

Animal numbers

For monosynaptic tracing, we had 9 *Fezf2-2A-CreER* animals for psilocybin condition (4 male and 5 female), 8 *Fezf2-2A-CreER* animals for saline condition (4 male, 4 female), 8 *PlexinD1-2A-CreER* animals for psilocybin condition (4 male, 4 female), 8 *PlexinD1-2A-CreER* animals for saline condition (4 male, 4 female). For in vivo electrophysiology, we used 6 *Ai32* animals for the psilocybin condition (2 male, 4 female) and 6 *Ai32* animals for the saline condition (3 male, 3 female). For chemogenetics, we used 4 animals in the DMSO + saline group (2 male, 2 female), 3 animals in the DMSO + psilocybin group (1 male, 2 female), 4 animals in the DCZ + saline group (2 male, 2 female), and 4 animals in the DCZ + psilocybin group (2 male, 2 female). For two-photon imaging, we used 7 *Fezf2-2A-CreER* animals for the saline condition (2 male, 5 female) and 8 *Fezf2-2A-CreER* animals for the psilocybin condition (4 male, 4 female), with a total of 60 and 62 fields of view imaged for saline and psilocybin conditions, respectively. For immunohistochemistry, we used 4 *Fezf2-2A-CreER;Ai75* animals (4 females) and 5 *PlexinD1-2A-CreER;Ai75* animals (5 females). For slice electrophysiology, we used two strategies to label the PT^{Fezf2} neurons. For transgenic Ai14-based labeling, we used 6 *Fezf2-2A-CreER;Ai14* animals (2 male, 4 female) for the saline condition at 24 hr time point, 7 *Fezf2-2A-CreER;Ai14* animals (4 male, 3 female) for the psilocybin condition at 24 hr time point, 6 *Fezf2-2A-CreER;Ai14* animals (3 male, 3 female) for the saline condition at 3 day time point, and 7 *Fezf2-2A-CreER;Ai14* animals (5 male, 2 female) for the psilocybin condition at 3 day time point. For viral mediated tdTomato expression, we used 4 *Fezf2-2A-CreER* animals (1 male, 3 female) for the saline condition and 5 *Fezf2-2A-CreER* animals (2 male, 3 female) for the psilocybin condition.

Viruses

For rabies viral tracing, the Cre-dependent AAV helper (AAV1-hSyn-DIO-TVA^{66T}-dTomato-CVS N2c G), Cre-dependent AAV control (AAV1-hSyn-DIO-TVA^{66T}-dTomato), and EnvA-pseudotyped G-deleted rabies virus (EnvA-CVS N2c$^{\Delta G}$-H2B-EGFP) were generated at the Allen Institute as previously described.[68] The DIO design utilizes the Cre-dependent FLEX strategy to ensure that expression is restricted to Cre-positive starter neurons. The viruses were engineered to have several favorable characteristics.[68] One, the TVA has a point mutation Glu^{66} to Thr to reduce EnvA-enveloped viral transduction, which mitigates the issue of non-specific, Cre-independent transduction of rabies virus due to leaky TVA expression.[69] Two, EGFP is fused to the histone H2B to restrict expression within the nucleus, enabling automated cell counting using machine learning methods. Three, the CVS N2c strain of rabies virus allows for efficient retrograde spread from cortical neurons, labeling more input cells per starter cell.[70] For in vivo electrophysiology,

AAVretro-hSyn-Cre-WPRE-hGH (Catalog #105553) was purchased from Addgene. For chemogenetics, AAV9-hSyn-hM4D(Gi)-mCherry (Catalog #50475) was purchased from Addgene. For two-photon imaging, AAV1-pCAG-FLEX-EGFP-WPRE (Catalog #51502) was purchased from Addgene, and AAV9-hSyn-Synaptophysin-mRuby2-WPRE-polyA vector was custom-designed and packaged by a commercial vendor (BrainVTA). For immunohistochemistry, AAV9-mDlx-GFP-Fishell-1 (Catalog #83900) was purchased from Addgene. For slice electrophysiology, AAV1-FLEX-tdTomato (Catalog #28306) and AAV9-hSyn-hChR2(H134R)-EYFP (Catalog #26973) were purchased from Addgene. The viruses were aliquoted and stored at -80°C. Prior to stereotaxic injection, the viruses were removed from the -80°C freezer and thawed on ice.

Surgery

Surgery commenced with anesthesia induction using 2-3% isoflurane. Once the animal reached a surgical level of anesthesia, it was placed in a stereotaxic frame (Model 900, David Kopf Instruments). Dexamethasone (2 mg/kg, i.m.; #1DEX022, Bimeda) and carprofen (5 mg/kg, s.c.; #059149, Covetrus) were administered for anti-inflammatory and analgesic effects. Eye lubricant (Optixcare Eye Lube, #062143, Covetrus North America) was applied to protect the eyes from drying and potential damage. Anesthesia was maintained at 1-1.5% isoflurane during the entire procedure. Core body temperature was maintained at 38°C using a far-infrared warming pad (#RT-0515, Kent Scientific). The area above the skull was shaved. The scalp was sterilized with ethanol pads and povidone-iodine. A small incision (~1 cm) was made along the midline. The skin and fascia were carefully removed to expose the skull. Burr holes were drilled at specific target sites using a handheld dental drill (#HP4-917, Foredom). The viruses were injected intracranially via a borosilicate glass micropipette connected to an injection control unit (Nanoject II Auto-Nanoliter Injector, Drummond Scientific). Injections were performed for various experiments using different viral vectors and volumes, as detailed below, using 4.6 nL pulses with a 20-second interval between pulses. To minimize backflow, the micropipette was left in place for 5-10 minutes following the end of the injection before being withdrawn slowly. The brain surface was kept moist with artificial cerebrospinal fluid (aCSF; in mM: 135 NaCl (#S5150, Sigma-Aldrich), 5 HEPES (#H3537, Sigma-Aldrich), 5 KCl (#60142, Sigma-Aldrich), 1.8 $CaCl_2$ (# 21115, Sigma-Aldrich), 1 $MgCl_2$ (#63069, Sigma-Aldrich); pH 7.3). After completing the injections, the burr holes were covered with a silicone elastomer (#10006546, Smooth-On, Inc.). The incision was sealed using surgical sutures (#1265B, Surgical Specialties Corporation). Post-surgical analgesia was provided with carprofen (5 mg/kg, subcutaneously) immediately following the procedure and once daily for three days thereafter.

All mice received injections in one hemisphere only, and we targeted the right hemisphere. The anteroposterior (AP) and mediolateral (ML) coordinates are measured from bregma, with ML distances taken from the midline. The depth was measured from the brain's pial surface. For monosynaptic tracing of inputs, on day 1, the Cre-dependent AAV helper (276 nL) was injected into the medial frontal cortex (coordinates are AP: 1.6 mm, ML: 0.4 mm, depth: -0.6 and -0.8 mm) in a *Fezf2-2A-CreER* or *PlexinD1-2A-CreER* mouse. More specifically, half of the volume was injected at a depth of -0.6 mm and the remainder was injected at -0.8 mm. The anatomical coordinates correspond to the ACAd (anterior cingulate area, dorsal part) and the medial portion of MOs (secondary motor area) of the mouse. For control experiments, the Cre-dependent AAV control (276 nL) was injected instead. On days 7 through 11, tamoxifen was administered daily to induce the expression of Cre recombinase. On day 20, psilocybin (1 mg/kg, i.p.; prepared fresh monthly from powder; Usona Institute) or saline was administered. On day 21, G-deleted rabies virus (276 nL) was injected in the medial frontal cortex at the same stereotaxic coordinates. On day 28, the mouse was deeply anesthetized for transcardial perfusion.

For in vivo electrophysiology, the AAVretro-hSyn-Cre-WPRE-hGH (276 nL) was injected into the medial frontal cortex (AP: 1.6 mm, ML: 0.4 mm, depth: -0.6 and -0.8 mm) of an *Ai32* mouse. Three weeks later, the mice underwent a second surgical procedure. A midline incision was made, the skin above the skull was removed, and the periosteum of the skull was cleared. A 0.9-mm-diameter craniotomy was drilled using a handheld dental drill, and a self-tapping bone screw (0.86 mm; #19010-10, Fine Science Tools) was placed into the cerebellum to serve as a ground screw. A stainless steel headplate (eMachineShop; design available at https://github.com/Kwan-Lab/behavioral-rigs) was affixed to the skull using a rapid adhesive cement system (C&B Metabond, #S380, Parkell). The mouse would recover for at least one week before commencing the electrophysiological recording.

For chemogenetics, on day 1, the Cre-dependent AAV helper virus (diluted 1:3 in phosphate-buffered saline (PBS; #P4474, Sigma-Aldrich); 276 nL) was injected into the medial frontal cortex (AP: 1.6 mm, ML: 0.4 mm, depth: -0.6 and -0.8 mm) and AAV9-hSyn-hM4D(Gi)-mCherry (276 nL) was injected into the retrosplenial cortex (RSPd, retrosplenial area, dorsal part, and RSPv, retrosplenial area, ventral part; AP: -1.7 mm, ML: 0.15 mm, depth: -0.6 and -0.8 mm) in a *Fezf2-2A-CreER* mouse. On days 7 to 11, tamoxifen was administered daily to induce Cre-dependent gene expression. On day 20, deschloroclozapine (DCZ; 0.1 mg/kg, i.p.; #HY-42110, MedChemExpress) was administered from a stock solution (5 mg/mL) prepared in 100% DMSO and diluted with saline to achieve a final injection concentration (0.025 mg/mL) containing 0.5% v/v DMSO. For control, an equivalent amount of DMSO (0.5% v/v in saline) was administered. Then 15 minutes later, psilocybin (1 mg/kg, i.p.) or saline (i.p.) was injected. On day 21, the G-deleted rabies virus (276 nL) was injected in the medial frontal cortex at the same stereotaxic coordinates. On day 28, the mouse was deeply anesthetized and perfused transcardially with PBS followed by 4% paraformaldehyde (4% (v/v) in PBS). The brain was extracted and post-fixed in 4% paraformaldehyde overnight at 4°C.

For two-photon imaging of axonal boutons and dendritic structures, viral injections and window implantation were performed on the same day. Following induction of anesthesia, a midline scalp incision was made, and the skin above the skull was removed. The skull surface was gently cleared of connective tissue. AAV9-hSyn-Synaptophysin-mRuby2-WPREpolyA (276 nL) was injected into the retrosplenial cortex (AP: -1.7 mm, ML: 0.15 mm, depth: -0.6 and -0.8 mm) of a *Fezf2-2A-CreER* mouse. Next, a 3 mm circular

craniotomy was created over the medial frontal cortex (centered at AP: 1.6 mm, ML: 0.4 mm) using a dental drill. The exposed dura was kept moist with aCSF throughout the procedure. AAV1-pCAG-FLEX-EGFP-WPRE (1:100 dilution in PBS; 92 nL) was then injected into the medial frontal cortex (AP: 1.6 mm, ML: 0.4 mm, depth: -0.6 and -0.8 mm). Following viral injection, a double-layer glass window was placed over the craniotomy. The window was constructed by bonding two round coverslips (3 mm diameter, 0.15 mm thickness; #64-0720, Warner Instruments) using ultraviolet-curable optical adhesive (NOA 61, Norland Products), which was cured with an ultraviolet illuminator (#2182210, Loctite). Super glue adhesive (Henkel Loctite 454) was applied with caution to secure the window to the surrounding skull while maintaining slight pressure. A stainless steel headplate was then fixed onto the skull and centered on the glass window using a rapid adhesive cement system (C&B Metabond, Parkell). The mouse would recover and ensure sufficient AAV expression for at least 3 weeks after the window implantation and AAV injection before beginning imaging experiments.

To achieve CreER-induced gene expression, tamoxifen (#T5648, Sigma-Aldrich) was prepared as a 20 mg/mL solution in corn oil (#C8267, Sigma-Aldrich). The solution was fully dissolved using an ultrasonic bath at 37°C for 1-2 hours, then aliquoted into 1 mL portions, protected from light with aluminum foil, and stored at -20°C. Before administration, the tamoxifen aliquots were thawed and kept at 4°C. Each mouse was weighed, and tamoxifen was injected intraperitoneally at a dose of 75 mg/kg (equivalent to 0.094 mL of the 20 mg/mL solution for a 25 g mouse) once daily for five consecutive days (https://www.jax.org/research-and-faculty/resources/cre-repository/tamoxifen). The injection site was sanitized with 70% ethanol before each injection.

Whole-brain imaging after monosynaptic tracing: Light sheet fluorescence microscopy

Each mouse was perfused transcardially with ice-cold PBS containing 10 U/mL heparin (H3149, Sigma-Aldrich) and ice-cold 4% paraformaldehyde (PFA). After perfusion, the brain was extracted and incubated in 4% PFA at 4°C for 24 hours, then washed twice with PBS. The samples were stored in PBS with 0.02% sodium azide (#BDH7465-2, VWR) and then shipped to LifeCanvas Technologies (Cambridge, MA) for tissue clearing and imaging. The brains were preserved with SHIELD and then cleared with SmartClear technology, then immunolabeled for NeuN (#MCA-1B7, Encor Biotechnology) with eFLASH technology, which combined stochastic electrotransport and SWITCH techniques within a SmartBatch device. Following labeling, samples were incubated overnight at 37°C in 50% EasyIndex (RI = 1.52, LifeCanvas Technologies), then further incubated for 24 hours in 100% EasyIndex to achieve complete refractive index matching. For consistent index matching, the samples were embedded in 2% ultra-low melt agarose prepared with EasyIndex and left in EasyIndex overnight. Imaging was performed on a SmartSPIM axially-swept light sheet microscope with a 3.6x objective (0.2 NA), using a z-step size of 4 μm and an XY pixel size of 1.8 μm. The samples are imaged using three channels: 488 nm (GFP), 561nm (dTomato), and 647 nm (NeuN).

Whole-brain imaging after monosynaptic tracing: Image processing and cell detection

Each sample was aligned to the Allen Brain Atlas (Allen Institute: https://portal.brain-map.org/) through an automated alignment process conducted by LifeCanvas Technologies. NeuN channels for individual brains were registered to an average NeuN atlas generated by LifeCanvas Technologies using previously aligned samples. The registration was performed in stages using rigid, affine, and b-spline transformations (SimpleElastix: https://simpleelastix.github.io/). Cell detection was carried out through a two-step neural network approach. Initially, a U-Net-based fully convolutional network[71] was employed to detect potential cell locations with high sensitivity. Following this, a second network based on a ResNet architecture[72] was used to classify each detected location as either positive or negative, refining the accuracy of cell detection. This model leveraged both U-Net and Fully Convolutional Network architectures to optimize semantic segmentation. For colocalization analysis, single-channel cell centers were identified, and the spatial relationships between cells across channels were calculated. Cells in different channels were marked as colocalized if the Euclidean distance between a cell in channel 1 and a cell in channel 2 was less than three voxels, indicating coexpression within a single cell. Data after imaging processing and cell detection were tabulated in CSV files, which included region IDs and cell counts in each region for *Fezf2-2A-CreER* and *PlexinD1-2A-CreER* mice. We divided the brain into the 316 non-overlapping regions based on the "summary structures" defined by a prior study of the Allen Common Coordinate Framework (CCF).[28]

Whole-brain imaging after monosynaptic tracing: Analysis of starter cells

Starter cells were defined as those nuclei detected with coexpression in the 488 and 561 nm channels and located in one of the frontal cortical regions in the right hemisphere (MOp-R, ACAv-R, MOs-R, ACAd-R, PL-R, ILA-R, ORBm-R, and ORBvl-R).

As a quality check, we analyzed cells with colocalized red and green fluorescence in the entire brain (henceforth refer to as "red+green cells"), including in the right frontal cortex as well as also all other brain regions. For each region in each brain, we calculated the fraction of red+green cells, by dividing the number of red+green cells in a region by the total number of red+green cells in the brain. Unexpectedly, we observed a sizable number of puncta with red and green fluorescence in the left and right main olfactory bulb (MOB). We investigated this further by looking at the raw fluorescence images, which showed that the red-green puncta were in the glomerular layer of the olfactory bulb. These red-green puncta did not colocalize with NeuN, indicating that the signals did not originate from neurons, and instead likely come from lipofuscin granules.[73] When we excluded these red+green puncta in the MOB from our analysis, we found that nearly all (91.1%) of the red+green cells were indeed found in the right frontal cortex (MOp-R, MOs-R, ACAd-R, ACAv-R, PL-R, ILA-R, ORBl-R, ORBm-R, and ORBvl-R). Outside the right frontal cortex, the top three highest contributors were neighboring regions in the right anterior cortex with 1.01% of the red+green cells coming from FRP-R, 0.49% coming from

DP-R, and 0.43% coming from ENTI-R. There was negligible signal in the contralateral hemisphere, because only 0.54% of the red-green cells were detected in left frontal cortex (MOp-L, MOs-L, ACAd-L, ACAv-L, PL-L, ILA-L, ORBl-L, ORBm-L, and ORBvl-L). Overall, the starter cells were localized to the injection site as expected.

Whole-brain imaging after monosynaptic tracing: Analysis of input cells

Inputs cells were defined as those nuclei detected in the 488 nm. For the frontal cortical regions in the right hemisphere, some nuclei detected in 488 nm were also the nuclei with coexpression in the 488 and 561 nm channels, so the count was subtracted by the number of starter cells to yield the number of input cells.

The number of input cells in a brain varied depending on the number of starter cells, and the relationship was not linear. To aggregate the results across brain, we normalized by calculating, for each region of each brain, the "proportion of total input (%)" by dividing the number of input cells in the region by the total number of input cells in the brain. Next, instead of keeping track of all the summary structures, we focused on the regions that provided substantial inputs to the medial frontal cortex. We set a threshold to identify regions that contributed at least 0.3% of the total input cells for any experimental group (PT or IT, psilocybin or saline). This yielded regions that provided substantial inputs, which we called "presynaptic regions".

To evaluate the effect of psilocybin, for each presynaptic region, we computed "drug-evoked difference (%)" by subtracting the mean input fraction for psilocybin by the mean input fraction for saline, and normalized by divided by the mean input fraction for saline. To estimate the variance in drug-evoked difference, for each presynaptic region, we performed bootstrapping by drawing with replacement 75% of the psilocybin samples and 75% of saline samples, then calculated the drug-evoked difference for this scenario for 10,000 repeats. Using the distribution of drug-evoked differences from the bootstrapping, we estimate the 90% confidence interval for the drug-evoked difference for a presynaptic region.

To assess network-specific effects, we grouped presynaptic regions based on their network memberships. Networks were defined based on a prior large-scale connectivity study of the mouse neocortex,[18] including 5 networks: medial (ACAd, ACAv, RSPagl, RSPd, RSPv, VISa, VISrl), visual-auditory (AUDd, AUDp, AUDpo, AUDv, VISal, VISam, VISl, VISp, VISpl, VISpm, VISli, VISpor), sensorimotor (MOp, MOs, SSp-n, SSp-bfd, SSp-ll, SSp-m, SSp-ul, SSp-tr, SSp-un, SSs), lateral (GU, VISC, AId, AIp, AIv, TEa, PERI, ETC, PIR, ENTl), and ventromedial prefrontal cortex (PL, ILA, ORBl, ORBm, ORBvl, AON, TT, DP). Some presynaptic regions showed increased number of input cells after psilocybin relative to saline, whereas other presynaptic regions showed decreased number of input cells. To determine if the distribution of regions with increase or decrease (2 categories) are biased or evenly distributed for the networks (5 categories), we used the chi-squared test.

To determine cell-type differences in the network-specific effects, presynaptic regions that do not belong to these networks are considered 'Outside neocortex'. When assessing only saline data to determine baseline differences for inputs into PT and IT neurons, we would sum the number of input cells in the presynaptic regions that belong to a network. We used the two-sided Wilcoxon rank sum test to determine statistical significance between the two cell types for each network. To evaluate the effect of psilocybin on each network, we would first sum the number of input cells in the presynaptic regions that belong to a network, then compute "drug-evoked difference (%)" by subtracting the mean input fraction for psilocybin by the mean input fraction for saline, and normalized by divided by the mean input fraction for saline. To estimate the variance in drug-evoked difference, for each network, we performed bootstrapping by drawing with replacement 75% of the psilocybin samples and 75% of saline samples, then calculated the drug-evoked difference for this scenario for 10,000 repeats. Using the distribution of drug-evoked differences from the bootstrapping, we estimate the 90% confidence interval for the drug-evoked difference for a network. To determine cell-type specific differences, for each of the 10,000 repeats, we also calculated the difference in the drug-evoked difference between PT and IT neurons. Using this distribution of PT minus IT drug-evoked difference, we deemed the cell-type difference to be significant if 0 lies outside the 95% confidence interval.

For the network selectivity analysis, take PT^{Fezf2} neurons as an example, we started with the 65 presynaptic regions, each of which was associated with a drug-evoked difference. We analyzed the subset of 47 presynaptic regions that are part of the neocortex, with each belonging to 1 of 5 possible networks (medial, visual-auditory, sensorimotor, lateral, vmPFC). Based on the drug-evoked difference, we classified each of the 47 presynaptic regions as an increase or a decrease. A chi-squared test was used to determine if the observing proportions deviate from the expected proportions (e.g., observing a few people accumulating all the wealth while expecting wealth distributed equally). To calculate the chi-square statistic, we needed to know the observed proportions and expected proportions. The observed 5 proportions were the number of regions with increase divided by the number of regions in the 5 networks. The expected 5 proportions were an equal distribution with regions with increase divided evenly among the 5 networks. We determined the chi-square statistic for our experimental data. Based on the chi-square statistic and the degree of freedom ((2-1)*(5-1) = 4), we calculated the associated p-value. To evaluate the null distribution of chi-square statistics, we used bootstrapping. We created surrogate data by randomly shuffling the increase and decrease labels for the 47 presynaptic regions. Then we calculated the chi-square statistic using the shuffled data. We repeated this procedure for 1,000,000 times to generate the histogram corresponding to the null distribution.

Axonal projection analysis

The Allen Mouse Brain Connectivity Atlas has a curated database of fluorescence images of coronal sections of a mouse brain after injecting viral tracer in various brain regions.[35] For each of the 65 presynaptic regions, we identified an experiment in the database in

which the injection was done centering at that region. Then we downloaded the fluorescence image corresponding to the medial frontal cortex. Using the ImageJ software, we would draw one rectangle region of interest for ACAd, roughly corresponding to a segment spanning all the cortical layers in ACAd, and extract the pixel intensity along that laminar profile. We would draw another rectangle region of interest for medial MOs and repeat to extract the pixel intensity along that laminar profile.

For analysis, we first interpolate so the length of the ACAd profile matches the length of the MOs profile, because ACAd is thinner than medial MOs. We then average the ACAd and MOs profiles to get a single pixel intensity profile across cortical depth. Based on the pixel values as a function of depth, we fitted a cubic smoothing spline to estimate the axonal density as a function of depth. We defined the laminar positions as follows: layer 1 (0 – 5% of full depth), layer 2/3 (5 – 25%), layer 5 (25 – 50%), layer 6a (50 – 90%), and layer 6b (90 – 100%). Pearson correlation coefficients were used to assess the association between aspects of the axonal density and the drug-evoked difference in PT neurons as measured via monosynaptic tracing.

Serotonin receptor distribution and c-Fos analyses

Drug-related differences in the rabies tracing data were compared to publicly available region-level data on 5-HT receptor expression patterns and immediate-early gene (c-Fos) activation following psilocybin. For 5-HT receptor expression, *in situ* hybridization (ISH) data for *Htr1a*, *Htr2a*, and *Htr2c* mRNA were extracted across the cortical regions in prior studies,[24,54,74] with the original data coming from the Allen Mouse Brain Atlas gene expression database.[36] Per transcript, expression levels were computed as the mean ISH intensity across voxels of a given cortical region (“ISH energy”), then z-scored across regions for normalization.[74] For c-Fos expression, we used prior data from whole-brain light sheet imaging of c-Fos immunohistochemistry after treatment with psilocybin (1 mg/kg) or saline.[37] For each cortical brain region, we computed “drug-evoked difference (%)” by subtracting the mean c-Fos expression for psilocybin by the mean c-Fos expression for saline, and normalized by dividing the mean c-Fos expression for saline. Regional drug-evoked differences in the rabies tracing data were then compared to these independent estimates of 5-HT receptor expression and drug-evoked differences in c-Fos.

In vivo electrophysiology: Recording procedure

Mice were acclimated to head fixation over a four-day period, with exposure times progressively increased from 15 minutes on the first day to 30, 60, and finally 120 minutes on the subsequent days. On the day of the experiment, 3 hours before the recording, the mouse was anesthetized with isoflurane and a 2-mm-diameter craniotomy was performed over the retrosplenial cortex (RSP; AP: -1.7 mm, ML: 0.15 mm). To minimize tissue damage and prevent overheating during drilling, cold (4°C) artificial cerebrospinal fluid (aCSF) was applied to clear debris, and care was taken to prevent bleeding and remove bone particles. Following the craniotomy, an area of the dura mater was removed using a fine metal pin (#10130-10, Fine Science Tools). A section of Surgifoam (#1972, Ethicon), soaked in aCSF, was positioned over the exposed cortex to maintain moisture, and a layer of silicone elastomer was applied to ensure cleanliness and humidity in the craniotomy area until recording commenced. An intravenous catheter system (22-gauge; #383323, BD Saf-T-Intima Closed IV Catheter Systems), preloaded with psilocybin or saline, was kept at neutral pressure and implanted into the intraperitoneal cavity an hour prior to recording. The catheter was secured with Vetbond tissue adhesive (#1469SB, 3M Vetbond), with the tubing affixed to the head-fixation support frame to ensure stability during the session. Immediately before recording, the silicon polymer and Surgifoam were removed, and the craniotomy was gently rinsed with aCSF to ensure a clear field. A ground wire was wrapped around the self-tapping bone screw placed above the cerebellum. A Neuropixels 1.0 high-density silicon probe (#Neuropixels 1.0, IMEC), configured to record from the bottom-most 384 sites out of 960 available electrodes. Prior the insertion, the probe was coated with a 10 μL droplet of CM-DiI dye (1 mM in ethanol; #C7000, Invitrogen). The probe was inserted at a controlled rate of 100 μm/min via a micromanipulator (MPM; M3-LS-3.4-15-XYZ-MPM-Inverted, New Scale Technologies) until reaching a target depth of approximately 2000 μm. During probe implantation, aCSF was periodically applied to the craniotomy site. Once reaching the final position, the probe was held steady to stabilize for at least 30 minutes before recording commenced. Data were collected using the OpenEphys software in external reference mode, with action potentials recorded between 0.3-10 kHz at 30 kHz and LFP between 0.5-500 Hz at 2.5 kHz. The recording protocol involved a baseline period of 30 minutes, after which mice received an injection of either psilocybin or saline via the catheter, followed by an additional 60 minutes of recording. At the conclusion of each session, optotagging was conducted to identify ChR2-expressing neurons. A 473 nm laser (Obis FP 473LX, Coherent) connected to a 200 μm optical fiber was directed toward the craniotomy site using the micromanipulator, with laser pulses controlled by OpenEphys and triggered via a PulsePal (#1102, Sanworks), delivering 20 ms pulses at 1 Hz with an intensity of ~25 mW/mm^2. Each trial lasted 1 second, with a 980 ms inter-trial interval, across a minimum of 500 trials. Following the completion of recording, the probe was carefully retracted and cleaned using a sequence of 1% Tergazyme solution (#1304-1, Alconox Inc.), deionized water, and isopropyl alcohol (#AB07015, AmericanBio).

In vivo electrophysiology: Data analysis

Raw extracellular traces from the action potential band were processed with SpikeInterface,[75] which provided an end-to-end workflow for filtering, channel clean-up, spike detection, and quality-metric extraction. The preprocessing steps were: (1) passing the traces through a high-pass filter at 400 Hz to remove slow fluctuations while retaining action potentials; (2) excluding channels whose root-mean-square noise exceeded a session-specific threshold, which eliminated mostly the sites that were positioned outside the brain; (3) correcting for phase alignment to compensate for temporal offsets between channels; (4) removing shared noise sources,

including specifically the laser-induced artifacts, by common-median referencing. Spike sorting was then performed with Kilosort 2.5,[76,77] which iteratively matched template waveforms and tracked electrode drift, yielding an initial set of putative single units. These putative units were imported into Phy (https://github.com/kwikteam/phy) for manual curation: each cluster was inspected for waveform consistency, refractory-period violations, and stability over time, and subsequently labelled as good (well-isolated single unit), MUA (multi-unit activity), or noise. Only putative units marked good were retained for subsequent analyses. Quality metrics were then generated via SpikeInterface. Units were retained if they satisfied the following criteria[78]: (1) presence ratio $\geq$ 0.90. Presence ratio refers to the fraction of 60-s time bins in which the unit fired at least one spike, indicating stable activity throughout the session; (2) ISI violation rate < 0.5. ISI violation rate refers to the proportion of spikes occurring within 1.5 ms of a previous spike, indicating refractory-period compliance; (3) amplitude cutoff < 0.1. Amplitude cutoff estimated the fraction of spikes missed because their amplitudes fell below the detection threshold in the sorting algorithm and thus indicated waveform consistency; (4) isolation distance > 20. Isolation distance quantified the separation between the unit's waveforms and those of other units, ensuring adequate cluster isolation. To identify opto-tagged neurons, peri-stimulus time histograms (PSTHs) were created by aligning the spiking activity of each unit to the onset of laser stimulation. Opto-tagged neurons were then classified based on latency to spike and the reliability of spiking following laser onset.

Raw extracellular traces from the LFP band were analyzed in Python using custom scripts built upon numpy, scipy, and pynapple. Signal from each channel was low-pass filtered (<300 Hz), zero-centered by subtracting the time-averaged mean, and notch filtered to remove potential power-line noise at 60 Hz. LFP signals were segmented into non-overlapping 2-second epochs. Animal's movements could induce artifacts; therefore, we had a pre-processing step to exclude epochs with outliers. We had two thresholds. One threshold was fixed at ±1800 μV. The other threshold was channel-specific, set to be ±6× the standard deviation as calculated using the channel's signal. Any epoch that had spurious large-amplitude deflections that lied beyond either of the threshold would be excluded from further analysis. For the remaining epochs, power spectral density was computed using a custom implementation of the multi-taper method (time-bandwidth product = 3.0; number of tapers = 5), based on discrete prolate spheroidal sequences and fast Fourier transforms. Spectral power was calculated for the 1–100 Hz range and averaged across tapers. We made rough estimates of the cortical depth associated with each channel by using Phy to mark the location at which we began to switch from no detected units to detection of well-isolated single units and then calculating depth based on the known spacing between channels. For each range of depths (i.e., 0-300, 300-600, and 600-900 μm), we averaged the spectral power from all channels within that range. We collated the results for pre-drug (-30 – 0 min) and post-drug (0 – 60 min) windows. Subsequently, mean spectral power was extracted from five frequency bands: slow (0.2–1.5 Hz), delta (1.5–4 Hz), theta (4–10 Hz), beta (10–30 Hz), and gamma (30–80 Hz).[79]

In vivo electrophysiology: Histology

To evaluate fluorescence at specific brain regions, the fixed brain was sectioned at a thickness of 45 μm using a vibratome (VT1000S, Leica). The coronal sections were mounted on slides with mounting medium containing DAPI (#H-1200-10, Vector Laboratories) and covered with glass coverslips. Sections were imaged with a wide-field fluorescence microscope (BZ-X810, Keyence). For electrophysiology, the fluorescence came from the DiI that was coated on the Neuropixels probe. The DiI-labeled tracks in coronal sections were aligned to the Allen Common Coordinate Framework[28] using the SHARP-TRACK software.[80] Reconstructed probe tracks were visualized within the Allen CCF using Brainrender,[81] providing anatomical positioning of the recording sites.

Chemogenetics: Histology, imaging, and cell detection

For the chemogenetic experiments, the brain was sectioned at a thickness of 40 μm, and all consecutive slices were collected to ensure that capturing the target regions for analysis. During imaging, brain slices containing the target regions (RSP, AIv, TT, and VPM) were selected based on atlas alignment to maintain consistency across samples. For each brain region, 3 consecutive slices were imaged, using a 20x objective lens with a wide-field fluorescence microscope (BZ-X810, Keyence). The images were analyzed using the QUINT workflow,[82] with brain atlas registration based on the Allen Mouse Brain Atlas Common Coordinate Framework version 3 (CCFv3, 2017). The QUINT workflow was structured as follows: first, the images were pre-processed using Nutil[83] to adjust file names according to the QUINT convention and to downscale as needed for compatibility. Following this, registration to the atlas was performed in two stages. QuickNII[84] facilitated initial linear alignment, and VisuAlign was subsequently employed to refine the registration through non-linear adjustments. Once registered, specific image features were extracted using ilastik.[85] Quantification of these features was then conducted in Nutil. Since whole-brain imaging was not performed, the "Proportion of input (%)" refers to the proportion of input cells within the imaged brain sections rather than the entire brain.

Estimates for the number of PT, IT, PT^{Fezf2}, and $IT^{PlxinD1}$ neurons

To estimate the number of PT and IT neurons in the medial frontal cortex, we extracted cell counts from the "MERFISH-C57BL6J-638850 with Imputed Genes + Reconstructed Coordinates" data set,[67] which was publicly available in the Allen Brain Cell Types Knowledge Portal (https://knowledge.brain-map.org/abcatlas; "Allen Mouse Common Coordinate Framework, 2020 release"). We restricted the analyses to the ACAd and MOs regions of the isocortex, including their laminar subdivisions (e.g., ACAd1, ACAd2/3, ACAd5, ACAd6a, and ACAd6b). For each region, we classified cells as neuronal (Glut, GABA, and Glut–GABA) or

non-neuronal (NA). We further classified the glutamatergic neurons into subpopulations of interest: ET (022 L5 ET CTX Glut), CT (030 L6 CT CTX Glut), or IT (004 L6 IT CTX Glut, 005 L5 IT CTX Glut, 006 L4/5 IT CTX Glut, and 007 L2/3 IT CTX Glut). Cell counts for the different classifications were tabulated for presentation.

Although a prior study showed that the *Fezf2-2A-CreER* and *PlexinD1-2A-CreER* animals capture selectively cells belonging to the PT and IT subtypes of excitatory neurons,[22] it is unclear if the mice can be used to effectively express transgenes in all cells belonging to those subpopulations. To estimate the number of PT^{Fezf2} and $IT^{PlexinD1}$ neurons in the medial frontal cortex, we generated *Fezf2-2A-CreER;Ai75* or *PlexinD1-2A-CreER;Ai75* mice by crossing the respective inducible Cre-driver mice with the *Ai75* reporter mouse for Cre-dependent expression of tdTomato in the nucleus. At 3–4 weeks of age, each animal received a unilateral stereotaxic injection of AAV9-mDlx-GFP-Fishell-1 into the ACAd/medial MOs for GFP expression in GABAergic neurons. One week later, tamoxifen was administered daily for five consecutive days to induce tdTomato labeling of PT^{Fezf2} or IT^{Plxnd1} neurons. Three weeks after the final tamoxifen injection, mice were deeply anaesthetized, perfused with ice-cold PBS followed by 4% paraformaldehyde in PBS, and brains were post-fixed overnight at 4 °C. Coronal sections were cut at 40 μm thickness using a vibratome. Free-floating sections were washed twice in PBS, permeabilized for 10 min in 0.3 % Triton X-100/PBS (room temperature, protected from light), rinsed twice in PBS, and blocked for 1 h in blocking solution (5 % normal serum; Abcam AB7475, 0.1 % Triton X-100 in PBS). Sections were incubated overnight at 4 °C with mouse anti-NeuN (#MAB377, Millipore) primary antibody (diluted in blocking solution), washed three times in PBS (10 min each), and incubated for 1 h at room temperature with Alexa Fluor 405-conjugated secondary antibody (diluted in the same blocking solution). After three final PBS washes, sections were mounted with VECTASHIELD HardSet Antifade Mounting Medium without DAPI (#H-1400-10, Vector Laboratories). Images were acquired on a Zeiss LSM 880 confocal microscope. The images were analyzed in Fiji/ImageJ to obtain cell counts. Specifically, we quantified the proportion of excitatory neurons (i.e., those that are NeuN-positive but GFP-negative) that expressed tdTomato, indicating that they were either PT^{Fezf2} or IT^{Plxnd1} neurons.

Two-photon imaging: Imaging procedures

Two-photon imaging was performed using a Movable Objective Microscope (MOM, Sutter Instrument) equipped with a resonant-galvo scanner (Rapid Multi Region Scanner, Vidrio Technologies) and a water-immersion 20X objective (XLUMPLFLN, 20x/1.00 N.A., Olympus). Image acquisition was controlled by ScanImage 2020 (Vidrio Technologies). To visualize dendrites of PT^{Fezf2} neurons labeled with EGFP and axonal boutons labeled by Synaptophysin-mRuby2, two femtosecond-pulsed lasers were aligned to converge into the excitation path: a fixed-wavelength laser for excitation at 920 nm (Axon 920-2, Coherent) and a fixed-wavelength laser for excitation at 1064 nm (ALCOR 1064-2 W, SPARK Lasers). Emitted fluorescence signals were separated using dichroic mirrors and collected through a 475–550 nm bandpass filter for EGFP and a 580–680 nm bandpass filter for mRuby2. Power after the objective was typically below 20 mW for each laser. For longitudinal imaging of the same field of view, power levels for the lasers were held constant across sessions to ensure consistency.

During each imaging session, the mouse was head-fixed under 0.8-1% isoflurane anesthesia delivered via a nose cone. Body temperature was maintained at 37.4°C using a feedback-controlled heating pad system (FHC #40-90-8D). Imaging was targeted to the ACAd/medial MOs region within 400 μm of the midline. Apical tuft dendrites were identified within 0–200 μm of the pial surface, and segments located at 20–100 μm depth were selected for imaging. For each field of view, a z-stack was acquired for a depth of between 10–30 μm and at 0.5-μm intervals using bidirectional scanning at 15 Hz, with 1024 × 1024 pixel resolution and a spatial resolution of 0.094 μm per pixel. The same mouse would be imaged repeatedly at the same fields of view on days −3, −1, 1, and 3 relative to drug administration. No imaging was performed on day 0. On that day, the animal received an intraperitoneal injection of either psilocybin (1 mg/kg) or saline (10 mL/kg) while awake. Following the injection, the mouse would be transferred to a clean cage for observation of head twitch responses for 10 minutes before being returned to their home cage.

Two-photon imaging: Data analysis

Motion correction of the two-photon imaging data was performed using the MultiStackReg plugin in Fiji, with the transformation matrix derived from the green channel applied identically to the red channel. To quantify the change across sessions, the z-stack images for a field of view for the four time points (days −3, −1, 1, and 3) were imported. Based on the brighter EGFP signals in the green channel, we selected a narrower z-range that was consistently captured across days and converted to single images via maximal projection. Next, using custom MATLAB scripts, for each channel of each image, we subtracted the background, which was estimated by selecting a small region of interest in each image devoid of any neural structure to determine the mean background intensity value. Any pixel with a negative value after subtraction was set to zero. To equalize brightness across sessions, we then clipped pixel values to a range (10–160), and then linearly stretched them back to the full range (0–255). To further correct for potential misalignments, images were rigidly registered, using the green channel of the image from the first time point as reference via MATLAB's "imregtform" function (rigid, multimodal metric). We cropped the images to isolate a portion of the field of view that can be consistently observed across all time points.

Initially, by visualizing the EGFP-expressing dendrites of PT^{Fezf2} neurons and mRuby2-expressing axonal boutons in the same field of view, our goal was to identify specifically those axonal boutons from RSP that apposed dendritic spines in the medial frontal cortex. The mRuby2 was fused to synaptophysin, which worked well to localize the fluorophore selectively to axonal boutons. However, the

approach resulted in dense labeling of PT^{Fezf2} neurons, which made the dual-color analysis unreliable due to the many overlapping dendrites and therefore difficulty in characterizing all the spines along the dendrites. For this reason, we focused the analysis solely on the mRuby2-expressing axonal boutons.

We developed custom MATLAB scripts for automated detection of red fluorescent puncta. From the red channel of the image, we generated a binary mask by detecting pixel values that lied above an intensity threshold and requiring the pixel value to exceed the value at the same location in the green channel. The same threshold was used for analyzing all images and was chosen based on inspecting the histograms of pixel values from many images. Puncta (i.e., connected pixels in the binary mask) were detected, and puncta that were too small (<5 pixels) or too large (>1000 pixels) were excluded from further analysis. The number of puncta was determined for each image. Change in the number of puncta across sessions were normalized as percent change relative to the baseline, which was defined as the average number of puncta observed in day -3 and -1.

Slice electrophysiology: Sample preparation

The aim was to label PT^{Fezf2} neurons with a red fluorophore for targeted whole-cell recording, while expressing ChR2 in the axons of RSP→ACAd neurons for photostimulation. We used two different strategies to label PT^{Fezf2} neurons for slice electrophysiology. For the first strategy, we generated *Fezf2-2A-CreER;Ai14* mice to label PT^{Fezf2} neurons, and injected AAV9-hSyn-hChR2(H134R)-EYFP (#26973, Addgene) into RSP to express ChR2. This was our preferred strategy because PT^{Fezf2} neurons had bright and uniform tdTomato expression. Due to limited availability of the double transgenic mice in our colony, we also used a second strategy: using *Fezf2-2A-CreER* mice, AAV1-FLEX-tdTomato (#28306, Addgene) was injected into ACAd/medial MOs to label PT^{Fezf2} neurons, and AAV9-hSyn-hChR2(H134R)-EYFP (#26973, Addgene) was injected into RSP to express ChR2. For both strategies, 3- to 4-week-old animals underwent stereotaxic surgeries for viral injection. Tamoxifen was administered daily for five consecutive days to induce tdTomato labeling of PT^{Fezf2} neurons. Then at 7-8 weeks of age, brain slices were prepared from these mice for electrophysiological recordings.

Mice were randomly assigned to receive either psilocybin (1 mg/kg, i.p.) or saline (10 mL/kg, i.p.). Slice electrophysiology experiments commenced either 24 hours or 3 days after drug administration. On the day of the experiment, mice were anesthetized with isoflurane and perfused intracardially with an ice-cold cutting solution containing (in mM): 110 choline chloride (#C1879, Sigma-Aldrich), 25 $NaHCO_3$ (#S6014, Sigma-Aldrich), 2.5 KCl, 7 $MgCl_2$, 1.25 NaH_2PO_4 (#71505, Sigma-Aldrich), 0.5 $CaCl_2$, 11.6 sodium ascorbate (#11140, Sigma-Aldrich), 3.1 sodium pyruvate (#P2256, Sigma-Aldrich), and 20 glucose (#G8270, Sigma-Aldrich). Acute coronal brain slices (300 μm) containing the ACAd/ medial MOs were prepared using a vibratome (VT1000S, Leica Biosystems). The chamber in the vibratome was filled with the cutting solution and surrounded by ice. Following cutting, slices were transferred to artificial cerebrospinal fluid (aCSF) containing (in mM): 127 NaCl, 25 $NaHCO_3$, 2.5 KCl, 2 $CaCl_2$, 1.25 NaH_2PO_4, 1 $MgCl_2$, 1 sodium pyruvate, and 20 glucose. Slices were incubated at 34°C for 30 minutes, then maintained at room temperature for at least another 30 minutes before recording. Cutting solution and aCSF were prepared using deionized filtered water (18.2 MΩ·cm) and passed through 0.22 μm filters. The cutting solution and aCSF were continuously bubbled with 95% O_2 and 5% CO_2 for at least 15 minutes before use and throughout the slicing and recording procedures.

Slice electrophysiology: Recording procedure

Slices were transferred to a submerged recording chamber and continuously perfused with oxygenated aCSF (2–3 mL/min) at 30–32°C. Whole-cell voltage-clamp recordings were performed, as previously described,[15] on pyramidal neurons located in layer 5 of ACAd and medial MOs, identified by infrared-differential interference contrast and fluorescence. PT^{Fezf2} neurons were identified by their red fluorescence, while non-PT^{Fezf2} neurons were identified by the absence of fluorescence and their morphology (i.e., a triangular somata and a prominent apical dendrite). We recorded sequentially from adjacent PT^{Fezf2} and non-PT^{Fezf2} neurons that lie at the same depth, typically 30–50 μm below the slice surface, and within 50 μm apart laterally. Although the PT^{Fezf2} neuron was typically recorded first, we have also recorded the non-PT^{Fezf2} neuron first in some cases. Recording pipettes were pulled from borosilicate glass capillaries (BF-150-86-10, Sutter Instruments) using a horizontal puller (P-97, Sutter Instruments) to a tip resistance of 2–4 MΩ. Pipettes were filled with a cesium-based internal solution containing (in mM): 125 Cs-methanesulfonate (#C1426, Sigma-Aldrich), 8 NaCl (#71376, Sigma-Aldrich), 10 HEPES, 0.5 EGTA (#E4378, Sigma-Aldrich), 2 $MgCl_2$, 4 Mg-ATP (#A9187, Sigma-Aldrich), 0.4 Na-GTP (#G8877, Sigma-Aldrich), 10 Na-phosphocreatine (#P7936, Sigma-Aldrich), and 1 sodium ascorbate (pH 7.25–7.3 adjusted with CsOH (#213601000, Thermo Fisher Scientific)). All internal solutions were double filtered through a 0.22 μm syringe filter prior to use. Signals were acquired with a MultiClamp 700B amplifier (Molecular Devices), digitized at 10 kHz using a Digidata 1550A interface and pClamp software (Molecular Devices), and filtered at 2 kHz for voltage-clamp recording. Initial series resistance was <20 MΩ, and cells were excluded if access resistance exceeded 25 MΩ at the end of the recording.

Photostimulation of the ChR2-expressing RSP axons was achieved via blue LED illumination (470 nm, Thorlabs). Light pulse (2 ms duration) was delivered through a 40× water-immersion objective (0.8 NA, Olympus). To isolate optically evoked excitatory postsynaptic currents (oEPSCs), cells were held at –70 mV. To isolate optically evoked inhibitory postsynaptic currents (oIPSCs), cells were held at 0 mV. In some experiments, 1 μM tetrodotoxin (TTX, #1078/1, Tocris Bioscience) and 100 μM 4-aminopyridine (4-AP, #0940/100, Tocris Bioscience) were applied to block action potentials and restore synaptic release by enhancing terminal depolarization, respectively. LED intensity was typically kept within ~0.2–2.0 mW/mm^2 to avoid triggering network bursts or abnormal oEPSCs. A higher-intensity pulse was occasionally applied to determine the maximal synaptic response in each neuron when needed. For all paired recordings, the light stimulation intensity was kept constant to ensure comparability of synaptic input strength across the

two cells. In the recordings performed in the presence of TTX and 4-AP to isolate monosynaptic responses, higher light intensities (compared to recordings without TTX and 4-AP) were used. This adjustment was necessary because synaptic transmission under TTX requires stronger depolarization of presynaptic terminals, and network activity is suppressed by TTX, allowing for the use of stronger stimulation without inducing polysynaptic activity. To examine presynaptic function, paired-pulse ratio (PPR) was assessed using two consecutive light pulses (2 ms duration) with a 100 ms inter-pulse interval. Due to the use of Cs-based internal solution to isolate synaptic currents in voltage clamp, it was not possible to characterize hyperpolarization-activated sag that would have provided additional information to identify PT and IT cell types.

Slice electrophysiology: Data analysis

Electrophysiological data were analyzed using Clampfit 10.4 (Molecular Devices). For each type of recording, 5–15 consecutive trials with 15 s inter-trial interval were collected. Traces were aligned to stimulus onset and trial-averaged to obtain the response per cell for each measurement. Peak amplitudes of oEPSCs and oIPSCs were determined from the trial-averaged trace for each cell relative to its baseline (10 ms prior to stimulus). PPR was calculated as the ratio of the second oEPSC peak amplitude to the first oEPSC peak amplitude ($oEPSC_2$ / $oEPSC_1$) evoked by the two consecutive light pulses. Individual data points represent single recorded neurons or sequentially recorded cell pairs.

QUANTIFICATION AND STATISTICAL ANALYSIS

Statistical analysis

Analyses were performed in GraphPad Prism 10.0, MATLAB, Python, and R.

For the network selectivity analysis of the rabies tracing data, we used the chi-squared test as described in an earlier section.

We fit linear mixed effects models to analyze datasets with hierarchical structure (e.g. multiple cells recorded from the same mouse, multiple brain sections originating from the same animal), implemented using the "lmer" function in the lme4 package in R. For two-photon imaging data, we used a linear mixed effects model with fixed effects terms of drug (saline or psilocybin), time (day -3, -1, 1, or 3) and their interaction, with fields of view per mouse modeled as nested random intercepts to account for repeated measures. For slice electrophysiology, dependent measures oEPSC amplitudes and PPR were each fit with linear mixed effects models using fixed effects terms of drug (saline or psilocybin), time (24 hr or 3 day), cell type (PT^{Fezf2} or non-PT^{Fezf2}) and all interactions, with cell pairs per brain slice per mouse modeled as nested random intercepts. For slice electrophysiology PT^{Fezf2}/non-PT^{Fezf2} ratios, we used linear mixed effects models with fixed effects terms of drug (saline or psilocybin), time (24 hr or 3 day) and their interaction, with random intercepts for brain slices per mouse. For Neuropixels single-unit data, we used a linear mixed effects model with fixed effects terms of drug (saline or psilocybin), time (pre- or post-drug), cell type (opto-tagged or untagged), and all interactions, with cells per mouse modeled as nested random intercepts. For Neuropixels LFP data, we used a linear mixed effects model with fixed effects terms of drug (saline or psilocybin), frequency (slow, delta, theta, beta, or gamma) and their interaction, with a random intercept for each mouse. For chemogenetics data, we evaluated region-specific effects by fitting separate linear mixed effects models for each brain region. Each model included fixed effects of drug (saline or psilocybin), chemogenetic manipulation (DMSO or DCZ), and their interaction, with a random intercept for each mouse. When the linear mixed effects model indicated significant main or interaction effects, we performed post hoc pairwise comparison with Bonferroni correction via estimated marginal means using the emmeans package in R.

For comparisons between two sample groups, when per-group sample size was <10, we used the two-sided Wilcoxon rank-sum test, such as for testing the total number of starter or input cells in the whole brain. For comparisons between two sample groups, when per-group sample size was $\geq$ 10, we used the two-sided t-test, such as for comparing the baseline firing rates for opto-tagged cells between saline and psilocybin condition, or the paired t-test for paired data. For comparisons of cumulative distributions, we used two-sample two-sided Kolmogorov-Smirnov test, such as for comparing the time to first spike after laser onset for opto-tagged cells between saline and psilocybin condition.

Mean values are presented as mean ± SEM. Statistical significance was defined as $P < 0.05$.

CellPress
OPEN ACCESS

Supplemental figures

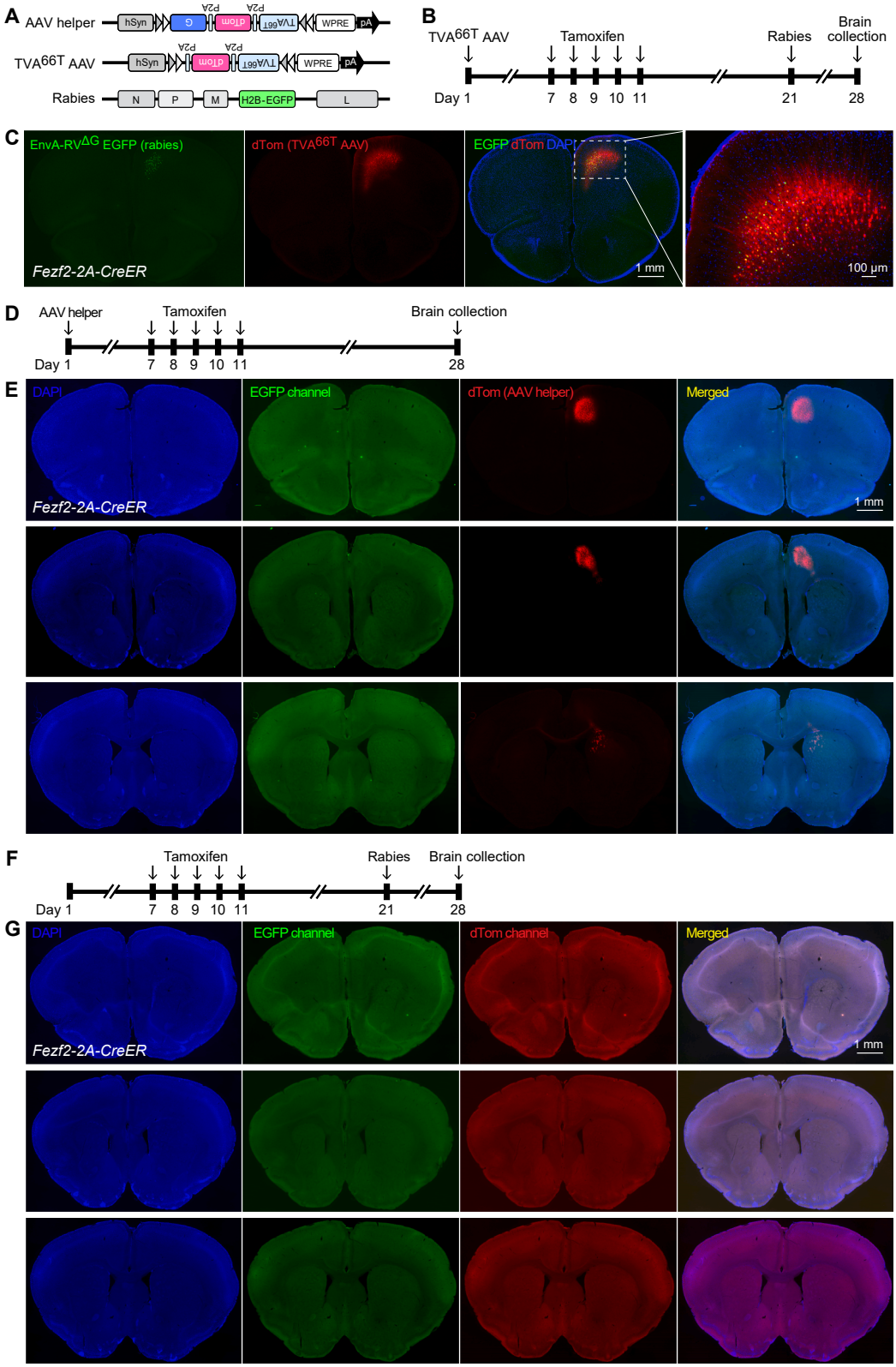

(legend on next page)

Figure S1. Control experiments validating monosynaptic tracing in *Fezf2-2A-CreER* mice, related to Figure 1

(A) Schematic of viral vectors used: Cre-dependent AAV helper (AAV1-hSyn-DIO-TVA^{66T}-dTomato-CVS N2c G), Cre-dependent AAV control without G protein (AAV1-hSyn-DIO-TVA^{66T}-dTomato), and EnvA-pseudotyped G-deleted rabies (EnvA-CVS N2c$^{\Delta G}$-H2B-EGFP).

(B and C) Experiment involving the Cre-dependent AAV control and G-deleted rabies virus. Experimental timeline. Representative images showing EGFP (green) and dTomato (red) expression restricted to the injection site around the medial frontal cortex of a *Fezf2-2A-CreER* mouse, with nuclear staining by DAPI (blue). As expected, the G-deleted rabies virus could not spread due to the lack of G protein.

(D and E) Experiment involving the Cre-dependent AAV virus only. Experimental timeline. Representative images showing dTomato expression (red) at the injection site in the medial frontal cortex of a *Fezf2-2A-CreER* mouse brain. As expected, there was no green fluorescence because the G-deleted rabies virus was not injected.

(F and G) Experiment involving the G-deleted rabies virus only. Experimental timeline. Representative images showing sections corresponding to the medial frontal cortex of a *Fezf2-2A-CreER* mouse. As expected, the G-deleted rabies virus could not enter any cell because the neurons lack the TVA receptor. Scale bars, 1 mm (C, left, E, and G), 100 μm (C, right).

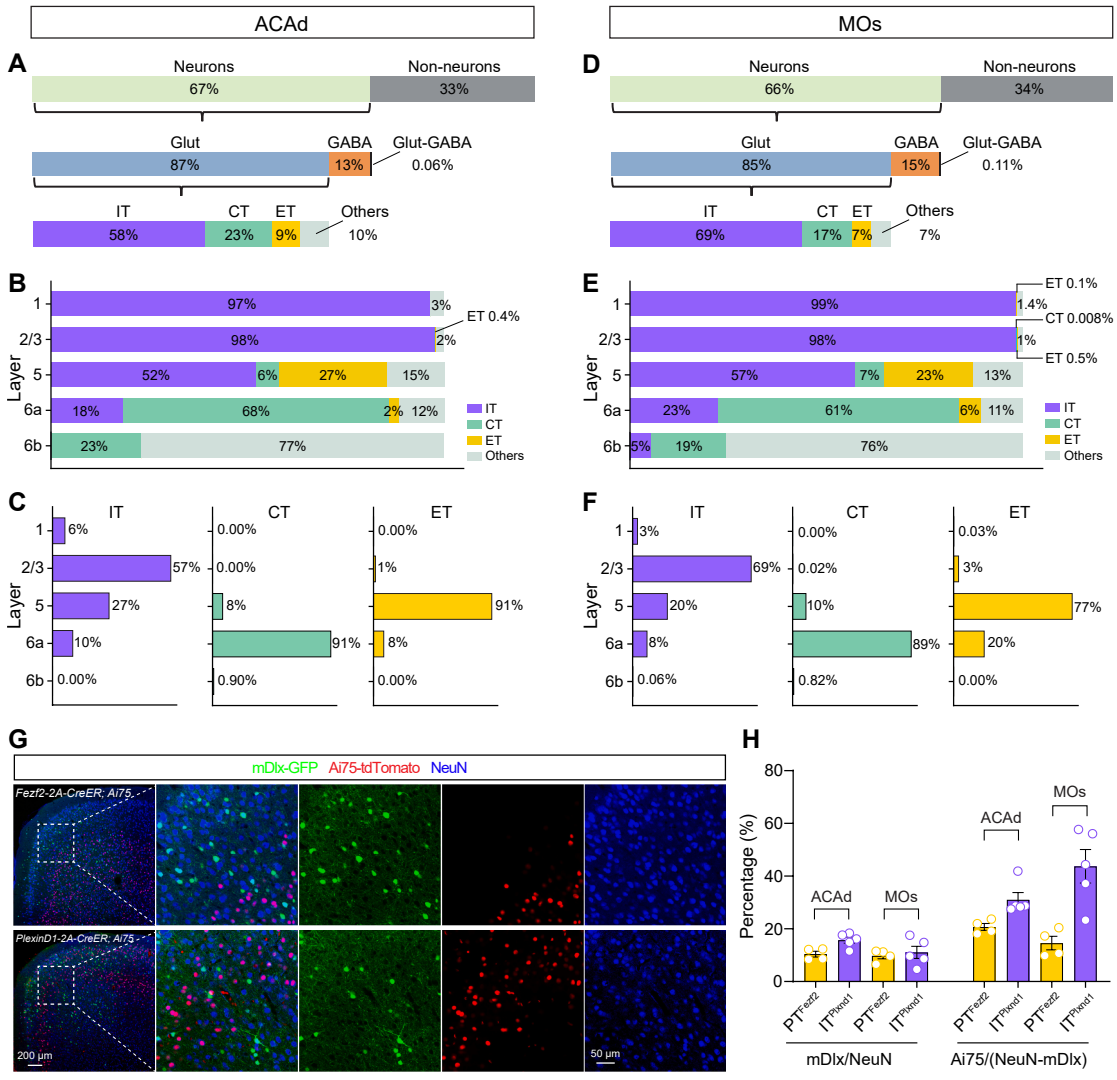

Figure S2. Estimates for the proportion of excitatory cells as PT, IT, PT^{Fezf2}, and IT^{Plxnd1} neurons in the mouse dorsal medial frontal cortex, related to Figures 1 and 2

(A) Proportion of cell types extracted from the publicly available spatial transcriptomics data hosted by the Allen Institute (Yao Z et al.[67]), focusing on the ~14,900 glutamatergic (Glut) neurons in ACAd. IT, intratelencephalic; CT, corticothalamic; and ET, extratelencephalic.

(B) Proportion of layers 1, 2/3, 5, 6a, and 6b neurons that are IT, CT, ET, or other glutamatergic neurons in ACAd.

(C) Proportion of IT, CT, and ET neurons that reside in layers 1, 2/3, 5, 6a, or 6b of ACAd.

(D–F) Similar to (A)–(C) for MOs.

(G) AAV-mDlx-GFP was injected into the ACAd/medial MOs region of a *Fezf2-2A-CreER;Ai75* mouse; therefore, GFP was expressed in GABAergic cells, tdTomato was expressed in PT^{Fezf2} neurons, and NeuN in blue was used to stain all neurons (top row). A similar strategy was applied to a *PlexinD1-2A-CreER;Ai75* mouse; therefore, GFP was expressed in GABAergic cells, tdTomato was expressed in IT^{Plxnd1} neurons, and NeuN in blue was used to stain all neurons (bottom row). Images from fixed coronal sections showing the dorsal medial frontal cortex. Scale bars, 200 μm (left), 50 μm (right).

(H) Quantification of the fraction of all neurons that were GABAergic in ACAd and medial MOs (left) and estimated fractions of excitatory (non-GABAergic) neurons that were PT^{Fezf2} or IT^{Plxnd1} neurons (right) (mean ± SEM).

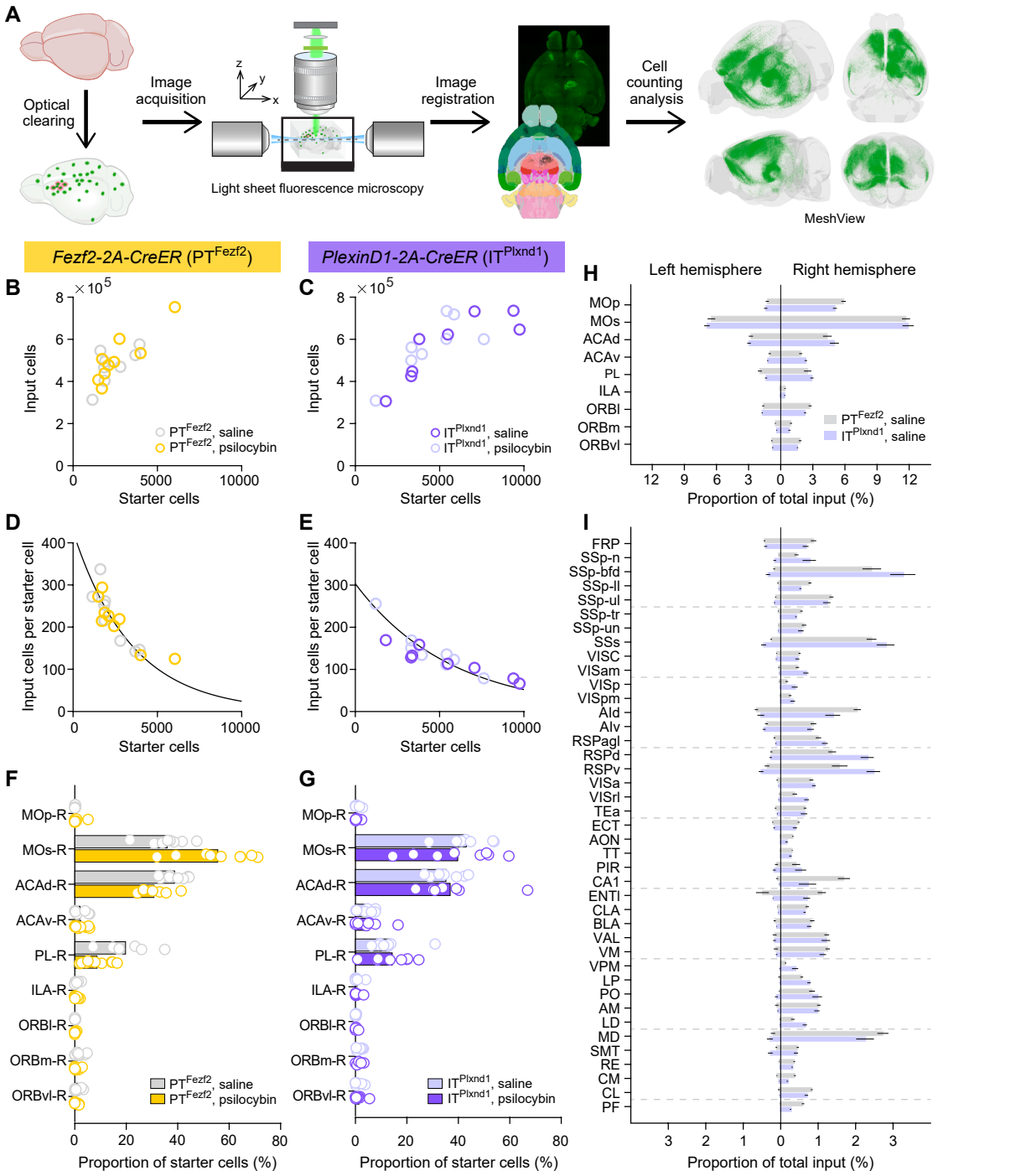

Figure S3. The distribution of input and starter cells in PT^{Fezf2} and IT^{Plxnd1} mice after saline or psilocybin treatment, related to Figures 1 and 2

(A) Workflow for whole-brain imaging and analysis. Following tissue clearing, brains were imaged using a light sheet fluorescence microscope. The images were registered to the Allen Brain Atlas for cell counting analysis. The EGFP-expressing input cells were visualized in MeshView.

(B) Relationship between the total number of input and starter cells in the brain in PT^{Fezf2} mice. Open circle, individual animal.

(C) Similar to (A) for IT^{Plxnd1} mice.

(D) The number of input cells per starter cell as a function of the number of starter cells in the brain of PT^{Fezf2} mice. Line, exponential decay fit to data from the saline condition. Open circle, individual animal.

(E) Similar to (C) for IT^{Plxnd1} mice.

(legend continued on next page)

(F) The distribution of starter cells in various frontal cortical regions in PT^{Fezf2} mice for the saline and psilocybin groups. Bar, mean. Open circle, individual animal.
(G) Similar to (E) for IT^{Plxnd1} mice.
(H) Proportion of total input cells in the left and right hemispheres for frontal cortical regions of PT^{Fezf2} and IT^{Plxnd1} mice in the saline condition (mean ± SEM).
(I) Similar to (G) for all other regions in the brain.

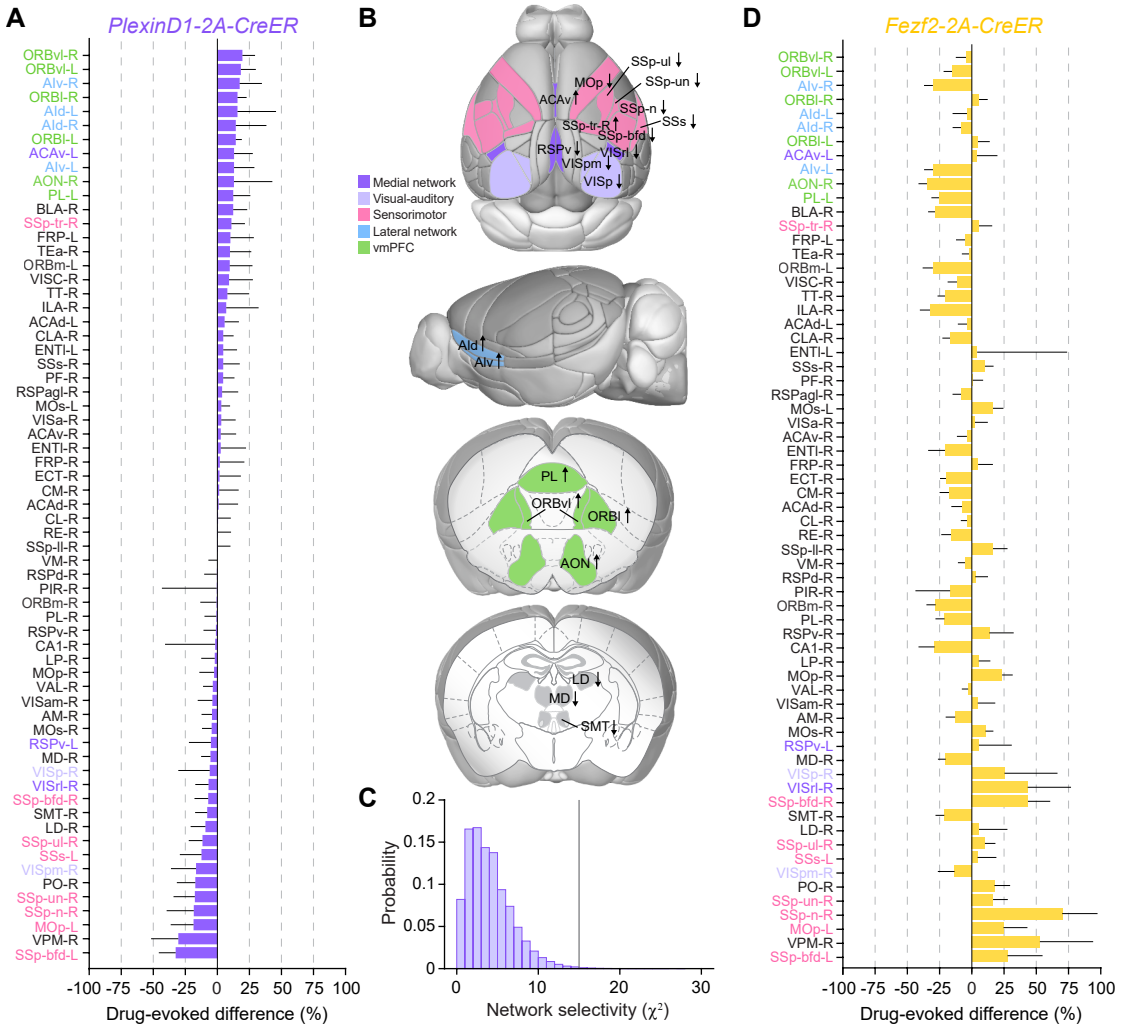

Figure S4. Drug-evoked difference and network selectivity for IT neurons in *PlexinD1-2A-CreER* mice, related to Figure 2

(A) Drug-evoked difference (psilocybin subtracted by saline, relative to saline) in the proportion of input cells for all 65 presynaptic regions for IT^{Plxnd1} neurons (mean and 90% confidence interval). The list of presynaptic regions was sorted based on the drug-evoked difference value for IT^{Plxnd1} neurons. Presynaptic regions with >10% or <−5% in drug-evoked difference were color coded according to their network membership.

(B) Schematic showing the location of the presynaptic regions with >10% or <−5% in drug-evoked difference for IT^{Plxnd1} neurons. The presynaptic regions are color coded according to their network membership.

(C) Network selectivity analysis, testing against the null hypothesis that the increases and decreases in drug-evoked difference for IT^{Plxnd1} neurons would be distributed randomly across the 5 cortical networks. Histogram, the distribution of χ^2 values for the null hypothesis. Vertical line, the observed χ^2 value (p = 0.0047).

(D) Drug-evoked difference (psilocybin subtracted by saline, relative to saline) in the proportion of input cells for all 65 presynaptic regions for PT^{Fezf2} neurons (mean and 90% confidence interval). The list of presynaptic regions was sorted based on the drug-evoked difference value for IT^{Plxnd1} neurons (i.e., same order as in A).

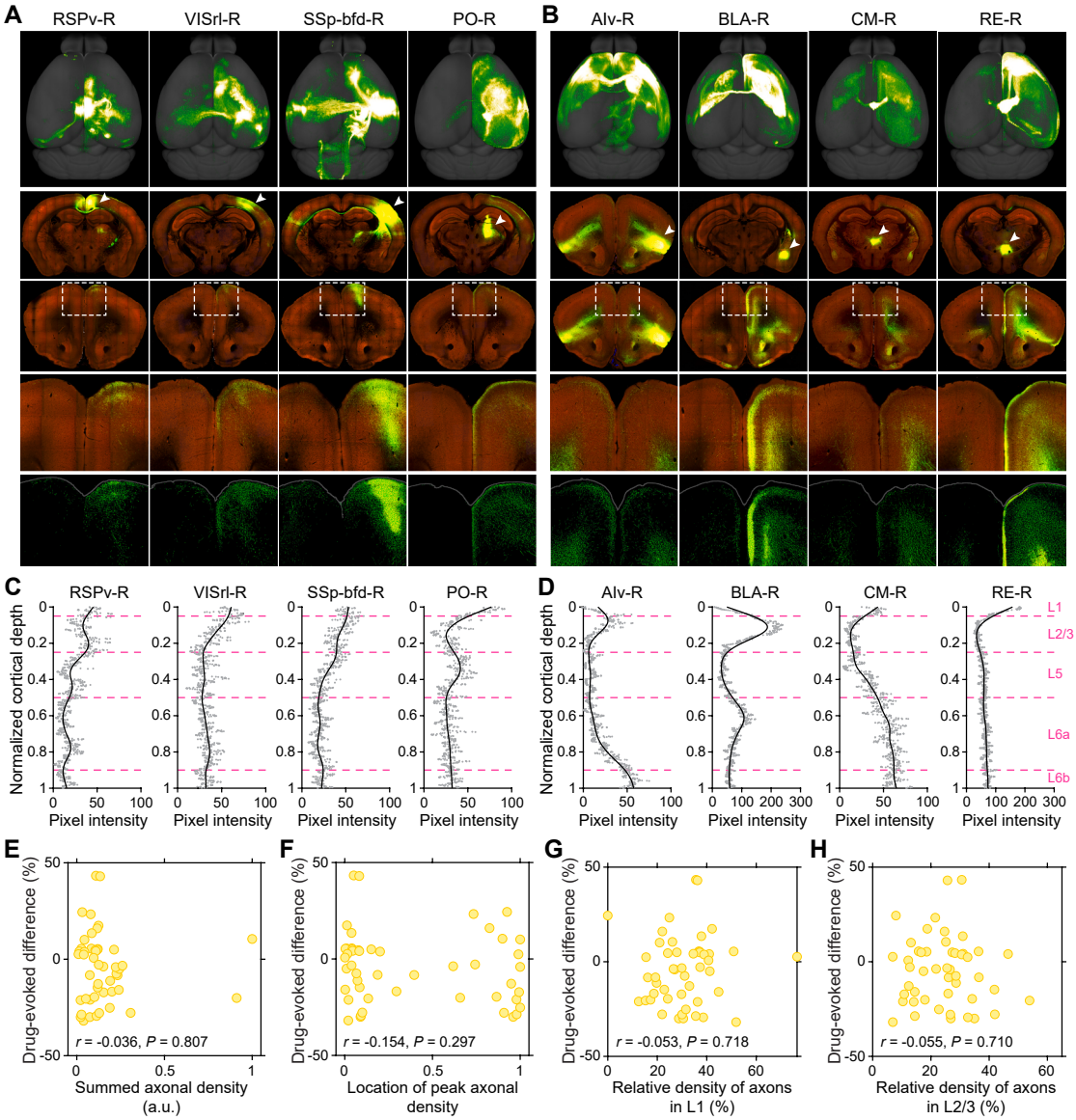

Figure S5. Analysis of the laminar profile of axonal density from presynaptic regions, related to Figure 3

(A) Representative images of 4 presynaptic regions with increased numbers of input cells following psilocybin treatment, as identified by monosynaptic rabies tracing. Top row, 3D visualization of brain-wide axonal projection emanating from neurons in the presynaptic region. Second row, serial two-photon image showing the section at the injection site (arrowhead). Third row, serial two-photon image showing the section at the dorsal medial frontal cortex. Fourth and fifth rows, magnified view of the framed area in the third row. Red, autofluorescence. Green, fluorophore.

(B) Similar to (A) for 4 presynaptic regions with decreased number of input cells.

(C) The laminar profile of pixel intensity (as an estimate of axonal density) in presynaptic regions corresponding to the examples shown in (A). Red dashed lines, positions that divide layers 1, 2/3, 5, 6a, and 6b.

(D) Similar to (C), corresponding to the presynaptic regions depicted in (B).

(E) Scatterplot showing how drug-evoked difference in the number of input cells to PT^{Fezf2} neurons may relate to the summed axonal density, which was calculated by adding up the pixel intensity across the entire profile. Filled circle, individual presynaptic region.

(F) Similar to (E) for location of peak axonal density, which was determined by finding the laminar position with the highest pixel intensity.

(G) Similar to (E) for relative density of axons in layer 1, which was calculated by dividing the summed axonal density in the portion of the profile demarcated as layer 1 by the summed axonal density across the entire profile.

(H) Similar to (G) for layer 2/3.

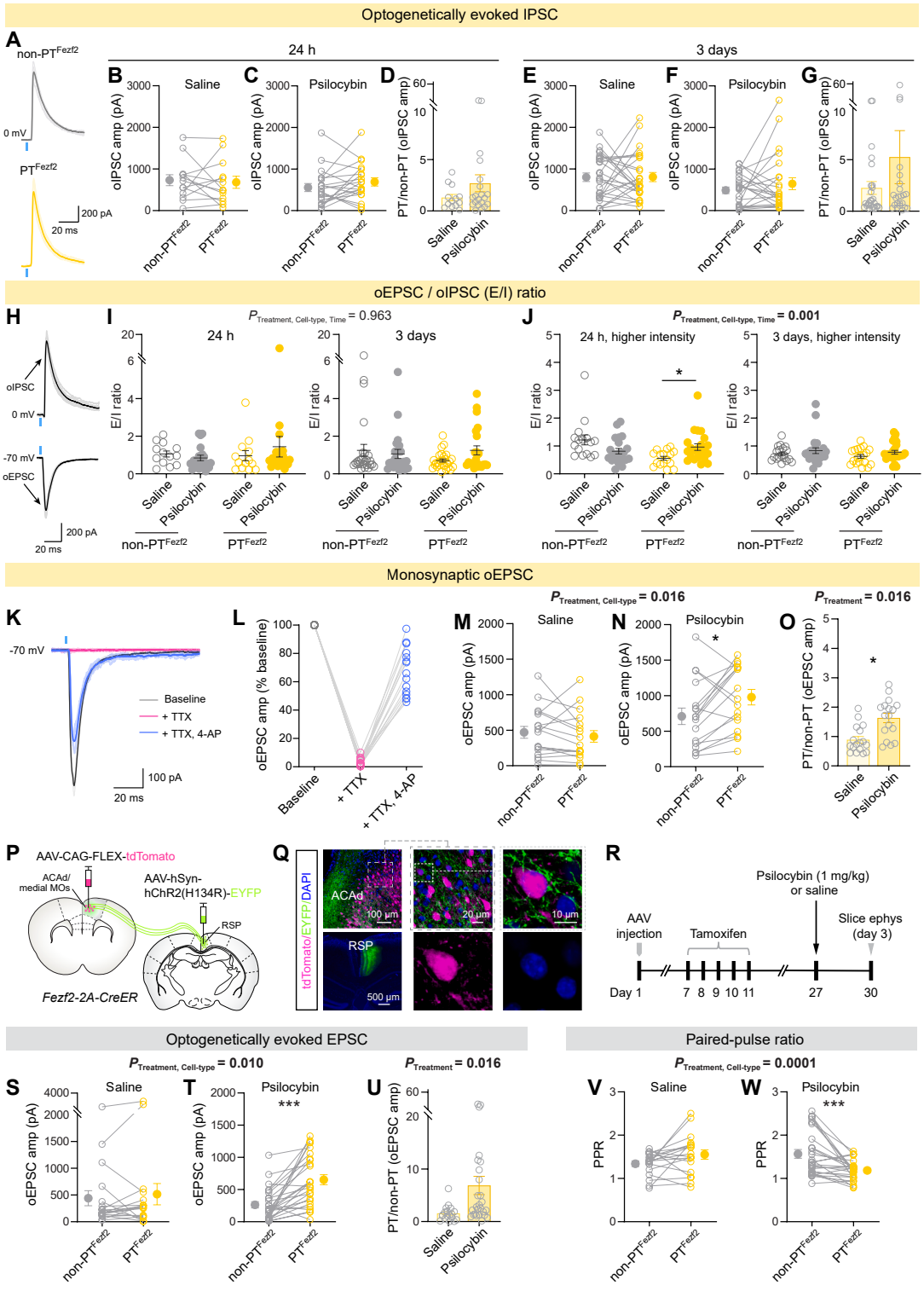

Figure S6. Additional analyses and data for the slice electrophysiology experiments, related to Figure 4

(A) Example optogenetically evoked inhibitory postsynaptic current (IPSC) in a pair of PT^{Fezf2} and non-PT^{Fezf2} neurons for saline and psilocybin condition.

(B) Amplitude of the optogenetically evoked IPSC, 24 h after saline administration. Circle, individual cell.

(C) Similar to (B) for psilocybin administration.

(legend continued on next page)

(D) Based on data in (B) and (C), the ratio is calculated by dividing the amplitude of a PT^{Fezf2} neuron by the amplitude of its paired non-PT^{Fezf2} neuron. Circle, individual cell pair. Bar, mean ± SEM.
(E–G) Similar to (B)–(D), 3 days after saline or psilocybin administration.
(H) Example oEPSC and oIPSC recorded from the same non-PT^{Fezf2} neuron.
(I) Ratio of the oEPSC amplitude divided by the oIPSC amplitude, 24 h or 3 days after saline or psilocybin administration, for PT^{Fezf2} and non-PT^{Fezf2} neurons. Circle, individual cell. Line, mean ± SEM.
(J) Similar to (I) except using a light pulse with higher intensity. This was because when using standard light intensity, EPSCs were reliably evoked, but IPSCs were sometimes absent. This was why after testing with the standard light intensity, we typically repeated the measurements with a higher light intensity, which could evoke stronger IPSCs. However, sometimes EPSCs have abnormal shapes at the higher light intensity, and those cells were excluded from this plot. Considering these caveats, we show both sets of data at the two different light intensities.
(K) Example optogenetically evoked EPSC at baseline and after the application of 1 μM TTX or 1 μM TTX and 100 μM 4-AP. TTX and 4-AP were added to isolate monosynaptic transmission.
(L) Amplitude of the optogenetically evoked EPSC in the different conditions, normalized by baseline. Circle, individual cell.
(M) Amplitude of the optogenetically evoked EPSC in the presence of TTX and 4-AP, 24 h after saline administration. Circle, individual cell.
(N) Similar to (M) for psilocybin administration.
(O) Based on data in (M) and (N), the ratio is calculated by dividing the amplitude of a PT^{Fezf2} neuron by the amplitude of its paired non-PT^{Fezf2} neuron. Circle, individual cell pair. Bar, mean ± SEM.
(P) Viral strategy to express ChR2 in RSP neurons. PT^{Fezf2} neurons express tdTomato because AAV-CAG-Flex-tdTomato was injected into the ACAd/medial MOs region of a *Fezf2-2A-CreER* mouse.
(Q) Post hoc histology showing the fluorophore expression in medial frontal cortex and RSP. Scale bars, 100 μm (left top), 20 μm (middle top), 10 μm (right top), 500 μm (left bottom).
(R) Experimental timeline. Successive whole-cell recordings were made from a PT^{Fezf2} neuron and a non-PT^{Fezf2} neuron. A 470 nm LED was used to photostimulate the RSP axons in the acute brain slice.
(S) Amplitude of the optogenetically evoked EPSC, 3 days after saline administration. Circle, individual cell.
(T) Similar to (S) for psilocybin administration.
(U) Based on data in (S) and (T), the ratio is calculated by dividing the amplitude of a PT^{Fezf2} neuron by the amplitude of its paired non-PT^{Fezf2} neuron. Circle, individual cell pair. Bar, mean ± SEM.
(V) PPR, 3 days after saline administration. Circle, individual cell.
(W) Similar to (V) for psilocybin administration.
Data in (A)–(O) came from the same experiments to obtain results shown in Figures 4E–4T (i.e., Ai14-based labeling of PT^{Fezf2} neurons). For (A)–(J), n = 13–16 cell pairs from 6 mice for 24 h after saline, 19–22 cell pairs from 7 mice for 24 h after psilocybin, 19–26 cell pairs from 5 mice for 3 days after saline, 23–24 cell pairs from 7 mice for 3 days after psilocybin. For (L), n = 15 cells from 14 animals. For (M)–(O), n = 17 cell pairs from 6 mice for 24 h after saline, 17 cell pairs from 5 mice for 24 h after psilocybin. Data in (P)–(W) came from the different experiments involving viral-mediated tdTomato expression in frontal cortical PT^{Fezf2} neurons. n = 18 cell pairs from 4 mice for 3 days after saline, 26 cell pairs from 5 mice for 3 days after psilocybin.
For (B), (C), (E), and (F), a linear mixed-effects model with fixed effects terms of drug (saline or psilocybin), time (24 h or 3 days), cell type (PT^{Fezf2} or non-PT^{Fezf2}), and all interactions, with cell pairs per brain slice per mouse modeled as nested random intercepts. For (D) and (G), linear mixed-effects model with fixed effects terms of drug (saline or psilocybin), time (24 h or 3 days), and interaction, with a random intercept for brain slice and animal. Post hoc pairwise comparisons with Bonferroni correction. For (I) and (J), data were analyzed separately using linear mixed-effects models with fixed effects of drug, time, cell type, and all interactions, and random intercepts for cell pair nested within brain slice and animal (Mouse/Slice/CellPair). Post hoc pairwise comparisons between treatment groups were performed for each cell type and time point using estimated marginal means with Bonferroni correction. For (M), (N), (S), (T), (V), and (W), data were analyzed separately using linear mixed-effects models with fixed effects of drug, cell type, and their interaction, with random intercepts for cell pair nested within brain slice and animal (Mouse/Slice/CellPair). Post hoc pairwise comparisons between cell types were performed within each treatment group using estimated marginal means, with Bonferroni correction. For (O) and (U), the ratio of oEPSC amplitudes (PTFezf2/non-PTFezf2) was analyzed separately using a model with drug as a fixed effect and brain slice nested within animal as a random intercept (Mouse/Slice). Post hoc comparisons were based on estimated marginal means. See Table S2. $^{*}p < 0.05$, $^{**}p < 0.01$, $^{***}p < 0.001$.

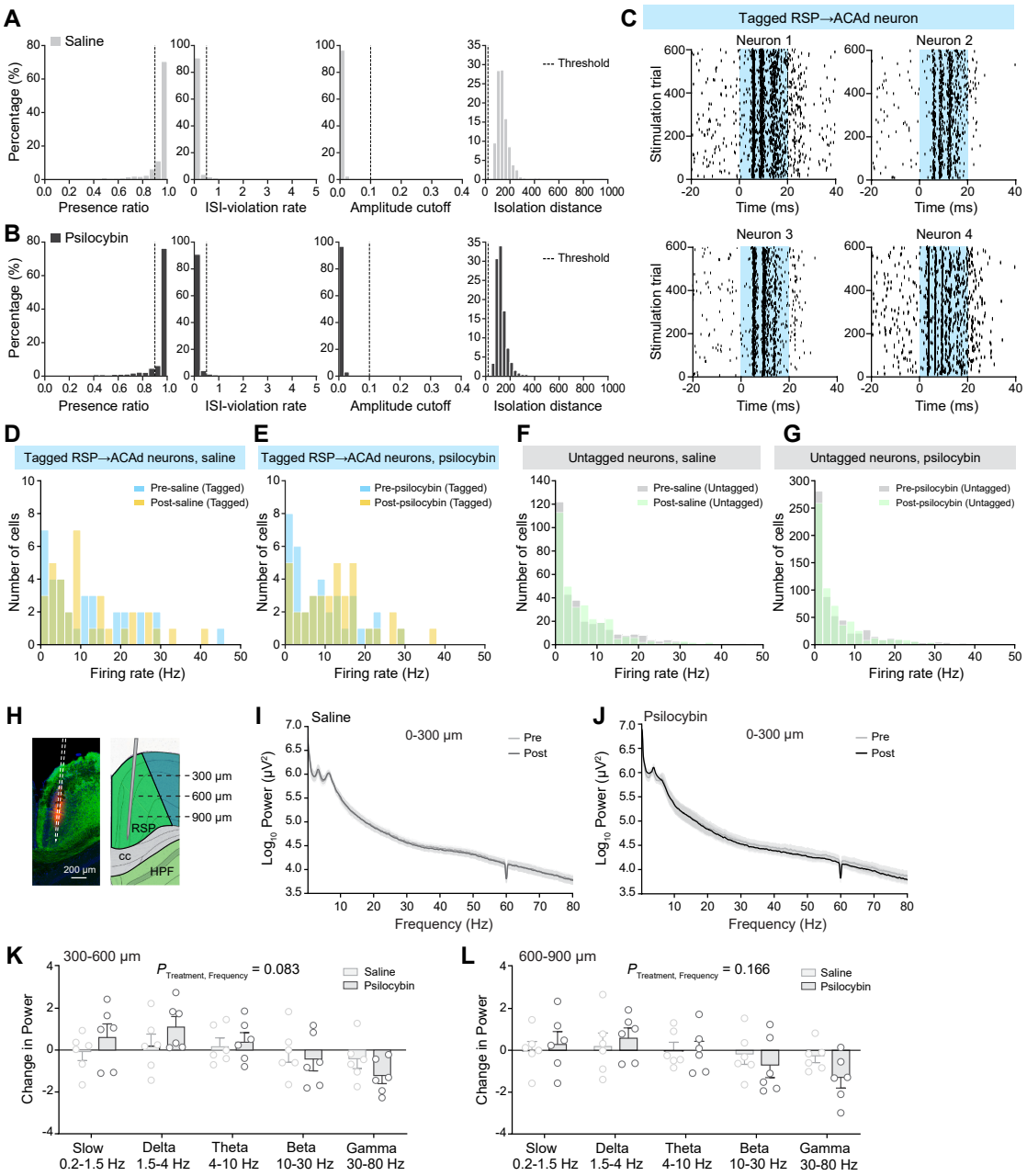

Figure S7. Additional analyses for the Neuropixels experiments, related to Figure 5

(A) The distribution of quality metrics for all untagged units in the saline group marked as "good" after Kilosort and Phy. Dashed line, the criterion for the units to be included for further analyses (see STAR Methods).

(B) Similar to (A) for the psilocybin group.

(C) Additional examples of spike raster plots for tagged RSP→ACAd neurons. Blue, period of laser stimulation.

(D) The distribution of firing rates for opto-tagged RSP→ACAd neurons in the pre and post periods around saline administration.

(E) Similar to (D) for opto-tagged RSP→ACAd neurons around psilocybin administration.

(F) Similar to (D) for untagged RSP neurons.

(G) Similar to (D) for untagged RSP neurons around psilocybin administration.

(H) This is the same histology figure shown in Figure 5C, delineating rough estimates for depths of 300, 600, and 900 µm. Scale bar, 200 µm.

(I) Mean power spectrum calculated from LFP signals from channels within a depth of 0–300 µm, before and after saline.

(J) Similar to (I), before and after psilocybin.

(K) Fractional change in spectral power within different frequencies after saline or psilocybin, calculated from LFP signals from channels within a depth of 300–600 µm. Circle, individual animal. Bar, mean ± SEM.

(L) Similar to (K), for channels within a depth of 600–900 µm.

(legend continued on next page)

Data came from the same experiments to obtain results shown in Figure 5. *N* = 6 mice for psilocybin and 6 mice for saline.
For (K) and (L), a linear mixed-effects model with fixed effects terms of drug (saline or psilocybin), frequency (slow, delta, alpha, beta, or gamma), and interaction, with a random intercept for animal.
See Table S2.